การร่วมผลิตไฮโดรคาร์บอน C2 และกำลังไฟฟ้าจากมีเทนโดยใช้เครื่องปฏิกรณ์เซลล์เชื้อเพลิงแบบออกไซด์แข็ง

นางสาววีรินทร์ดา อัปมานะ

วิทยานิพนธ์นี้เป็นส่วนหนึ่งของการศึกษาตามหลักสูตรปริญญาวิศวกรรมศาสตรดุษฎีบัณฑิต
สาขาวิชาวิศวกรรมเคมี ภาควิชาวิศวกรรมเคมี
คณะวิศวกรรมศาสตร์ จุฬาลงกรณ์มหาวิทยาลัย
ปีการศึกษา 2556
ลิขสิทธิ์ของจุฬาลงกรณ์มหาวิทยาลัย

COGENERATION OF C2 HYDROCARBONS AND ELECTRICAL POWER FROM METHANE USING SOLID OXIDE FUEL CELL TYPE REACTOR

Miss Weerinda Appamana

A Dissertation Submitted in Partial Fulfillment of the Requirements
for the Degree of Doctor of Engineering Program in Chemical Engineering
Department of Chemical Engineering
Faculty of Engineering
Chulalongkorn University
Academic Year 2013

Thesis Title	COGENERATION OF C2 HYDROCARBONS AND ELECTRICAL POWER FROM METHANE USING SOLID OXIDE FUEL CELL TYPE REACTOR
By	Miss Weerinda Appamana
Field of Study	Chemical Engineering
Thesis Advisor	Professor Suttichai Assabumrungrat, Ph.D.
Thesis Co-Advisor	Wisitsree Wiyaratn, Ph.D.

Accepted by the Faculty of Engineering, Chulalongkorn University in Partial Fulfillment of the Requirements for the Doctoral Degree

.....Dean of the Faculty of Engineering

(Professor Bundhit Eua-arporn, Ph.D.)

THESIS COMMITTEE

.....Chairman

(Associate Professor Muenduen Phisalaphong, Ph.D.)

.....Thesis Advisor

(Professor Suttichai Assabumrungrat, Ph.D.)

.....Thesis Co-Advisor

(Wisitsree Wiyaratn, Ph.D.)

.....Examiner

(Assistant Professor Apinan Soottitantawat, D.Eng.)

.....Examiner

(Assistant Professor Amornchai Arpornwichanop, D.Eng.)

.....External Examiner

(Assistant Professor Ratanawan Kiattikomol, Ph.D.)

วีรินทร์ดา อัปมานะ : การร่วมผลิตไฮโดรคาร์บอน C2 และกำลังไฟฟ้าจากมีเทนโดยใช้เครื่องปฏิกรณ์เซลล์เชื้อเพลิงแบบออกไซด์แข็ง. (COGENERATION OF C2 HYDROCARBONS AND ELECTRICAL POWER FROM METHANE USING SOLID OXIDE FUEL CELL TYPE REACTOR) อ.ที่ปรึกษาวิทยานิพนธ์หลัก: ศ. ดร. สุทธิชัย อัสสะบำรุงรัตน์, อ.ที่ปรึกษาวิทยานิพนธ์ร่วม: วิศิษฏ์ศรี วิยะรัตน์,121 หน้า.

งานวิจัยนี้ศึกษาการพัฒนาตัวเร่งปฏิกิริยาสำหรับปฏิกิริยาคู่ควบของมีเทน เพื่อผลิตสารประกอบ ไฮโดรคาร์บอน C2 และกระแสไฟฟ้า โดยแบ่งการศึกษาออกเป็น 2 ส่วน ในเครื่องปฏิกรณ์ 2 ชนิด คือ เครื่องปฏิกรณ์แบบเบดนิ่งและเซลล์ปฏิกรณ์เชื้อเพลิงแบบออกไซด์แข็ง การศึกษาในเครื่องปฏิกรณ์แบบเบดนิ่งจะดำเนินการที่อัตราส่วนโดย โมลของลักษณะการไหลผสมของก๊าซมีเทน, ก๊าซออกซิเจนและก๊าซไนโตรเจนคือ 4:1:5 ในช่วงอุณหภูมิ 700-900 องศาเซลเซียส โดยตัวเร่งปฏิกิริยาที่สนใจศึกษา คือ $Au/La_{0.6}Sr_{0.4}MnO_3$ (Au/LSM), $La_{0.25}Sr_{0.75}Cr_{0.5}Mn_{0.5}O_3$ (LSCM) และ $LiFeO_2$ (LFO) ได้มีการพัฒนาโดยการเติมซีเรียมเพื่อดูประสิทธิภาพของตัวเร่งปฏิกิริยา พบว่าการเติมซีเรียมจะช่วยให้ค่าการเลือกเกิดสารประกอบไฮโดรคาร์บอน C2 มากขึ้น สำหรับการศึกษาในเซลล์ปฏิกรณ์เชื้อเพลิงแบบออกไซด์แข็ง เซลล์ที่ใช้ประกอบด้วยขั้วแคโทดคือ $La_{0.8}Sr_{0.2}MnO_3$ (LSM) และ $La_{0.8}Sr_{0.2}FeO_3$ (LSF) อิเล็กโตรไลท์คือ 8% โมล yttria-stabilized zirconia (YSZ) และมีการเปรียบเทียบตัวเร่งปฏิกิริยาแอโนดที่แตกต่างกัน ใช้เทคนิคในการเตรียมเซลล์ด้วยวิธี tape casting และการแทรกซึมขั้วตัวเร่งปฏิกิริยาอิเล็กโทรดลงในรูพรุนของวัสดุอิเล็กโทรด สำหรับตัวเร่งปฏิกิริยาแอโนด การเติมซีเรียม (Ce) ในขั้วแอโนด $La_{0.25}Sr_{0.75}Cr_{0.5}Mn_{0.5}O_3$ (LSCM) ให้ค่าประสิทธิภาพของเซลล์ที่ดีที่สุด ตัวเร่งปฏิกิริยา Ce/LSCM ให้ค่าการเลือกเกิดผลิตภัณฑ์ไฮโดรคาร์บอน C2 เท่ากับ 78.4% ค่าการเปลี่ยนแปลงของมีเทนเท่ากับ 3.4% และกำลังไฟฟ้าสูงสุดที่ได้รับคือ 221 $mW.cm^{-2}$ ที่อุณหภูมิ 850 องศาเซลเซียส ภายใต้สภาวะโหลด 0.3 V สำหรับตัวเร่งปฏิกิริยา LFO เหมาะสำหรับการใช้งานในช่วงอุณหภูมิดำเนินการที่ต่ำกว่า 800 องศาเซลเซียส โดยทำการทดลองใช้อิเล็กโตรไลท์สำหรับช่วงอุณหภูมิที่ต่ำลงคือ $La_{0.9}Sr_{0.1}Ga_{0.8}Mg_{0.2}O_3$ (LSGM) พบว่าได้ค่าการเปลี่ยนแปลงของมีเทนเท่ากับ 3.1% ค่าการเลือกเกิดผลิตภัณฑ์ไฮโดรคาร์บอน C2 เท่ากับ 85.2% และกำลังไฟฟ้าสูงสุดที่ได้รับคือ 38 $mW.cm^{-2}$ ที่อุณหภูมิ 750 องศาเซลเซียสภายใต้สภาวะโหลด 0.3 V

ภาควิชา วิศวกรรมเคมี ลายมือชื่อนิสิต .....

สาขาวิชา วิศวกรรมเคมี ลายมือชื่อ อ.ที่ปรึกษาวิทยานิพนธ์หลัก .....

ปีการศึกษา 2556 ลายมือชื่อ อ.ที่ปรึกษาวิทยานิพนธ์ร่วม .....

5170611421 : MAJOR CHEMICAL ENGINEERING
KEYWORDS: SOLID OXIDE FUEL CELL/ C2 HYDROCARBON/ OXIDATIVE COUPLING OF METHANE/ / ANODE / INFILTRATION/ TAPE CASING/ YSZ WEERINDA APPAMANA: COGENERATION OF C2 HYDROCARBONS AND ELECTRICAL POWER FROM METHANE USING SOLID OXIDE FUEL CELL TYPE REACTOR

WEERINDA APPAMANA: COGENERATION OF C2 HYDROCARBONS AND ELECTRICAL POWER FROM METHANE USING SOLID OXIDE FUEL CELL TYPE REACTOR. ADVISOR: PROF. SUTTICHAI ASSABUMRUNGRAT, Ph.D., CO-ADVISOR: WISITSREE WIYARATN, Ph.D., 121 pp.

This work developed the new anode catalysts for co-generation of C2 hydrocarbons and electric power from methane. The study is divided into 2 parts in two different types of reactor: 1) Fixed bed reactor (FBR) and (2) Solid oxide fuel cell reactor (SOFC). In part 1, the experiments were performed using co-feeds of methane, oxygen and nitrogen inert gas molar ratio of 4:1:5 at various temperatures (700-900 $^{\circ}$C). Three types of catalysts; Au/$La_{0.6}Sr_{0.4}MnO_3$ (Au/LSM), $La_{0.25}Sr_{0.75}Cr_{0.5}Mn_{0.5}O_3$ (LSCM) and $LiFeO_2$ (LFO), have been investigated. The catalyst was doped with ceria in order to improve its catalytic activity. The results indicated that the addition of Ce promoter could promote the C2 selectivity. In part 2, $La_{0.8}Sr_{0.2}MnO_3$ (LSM) and $La_{0.8}Sr_{0.2}FeO_3$ (LSF) were uses as the cathode while 8 mol% yttria-stabilized zirconia (8YSZ) was used as the electrolyte. The various types of electrode catalyst for anode have been investigated. Membrane cell has been fabricated by the tape casting and solution impregnation method. For the anode catalyst, the CeO_2-LSCM infiltrated provided the excellent electrode performance. Ce/LSCM catalyst provided the C2 selectivity of 85%, CH_4 conversion of 3.4%, and the maximum power densities of 221 mW.cm^{-2} at 800°C under a load of 0.3 V. In case of LFO catalyst, it was suitable to operate under the temperature lower than 800 $^{\circ}$C. The $La_{0.9}Sr_{0.1}Ga_{0.8}Mg_{0.2}O_3$ (LSGM) has been used as the electrolyte at low temperature operation. It provided the CH_4 conversion of 3.1%, C2 selectivity of 85.2% and the maximum power densities of 38 mW.cm^{-2} at 750°C under a load of 0.3 V.

Department:	Chemical Engineering	Student's Signature .....
Field of Study:	Chemical Engineering	Advisor's Signature .....
Academic Year:	2013	Co-Advisor's Signature .....

ACKNOWLEDGEMENTS

The author would like to show her high appreciation to my advisor, Professor Suttichai Assabumrungrat and my co-advisor, Dr.Wisitsree Wirayan. It is an honour for me to have a great chance working with them. Thanks for their invaluable suggestion and encouragement in both research study and life attitude. I would also be grateful to Prof. John T. S. Irvine for his kind assistance, valuable advice, and encouragement as he allowed me to use his equipment to complete my experiments at St.Andrew University, England for one year. Moreover, the author would like to thank to Associate Professor Muenduen Phisalaphong as the chairman, Assistant Professor Apinan Soottitantawat, Assistant Professor Amornchai Arpornwichanop and Assistant Professor Ratanawan Kiattikomol as the members of the thesis committee for their kind cooperation.

Special thanks extended to Dr. Sumittra Charojrochkul for her great help in paper publication, kind assistance and valuable advice. The author would like to acknowledge for the financial support and the opportunity to study abroad from the Royal Golden Jubilee PhD Program, Thailand Research Fund (TRF). Moreover, the author would like to thank Center of Excellence in Catalysis and Catalytic Reaction Engineering (CECC), Chulalongkorn University for the facility and equipment during my research study.

I am indebted to many of my former and present colleagues in JTSI group for their assistance, advice and fruitful discussion. Special thanks go to Julie Nairn and Mr. George Antony for all of lab facilities, Dr. Cristian Savaniu for his advice on electrochemical testing, Thuy Muhl for her help on the testing jig, Dr. Paul Connor for his assistance on testing instruments.

Many thanks for kind helpful, suggestion and encouragement to many friends both in the Center of Excellence in Catalysis and Catalytic Reaction Engineering, Chulalongkorn University and school of chemistry, St andrews university, England.

Finally, the author would like to express the great gratitude to her beloved parents. Without their encouragement and support, the author cannot achieve the successful in her degree.

CONTENTS

Page

Page

Page

LIST OF TABLE

LIST OF FIGURES

LIST OF ABBREVIATIONS

List of acronyms

G/P	Galvanostat/Potentiostat
SEP	Solid Electrolyte Potentiometry
SOFC	Solid Oxide Fuel Cell
STP	Standard Temperature and Pressure
STM	Scanning Tunneling Microscopy
XPS	X-ray Photoelectron Spectroscopy
YSZ	Yttria-stabilized zirconia
ac, AC	alternating current
dc, DC	direct current
OCV	open circuit voltage, I=0
tpb	three phase boundaries
OCM	Oxidative coupling of methane

List of symbols

Symbol	Meaning
j0	exchange current density

jL	limiting current density
Keq	equilibrium constant
n	stoichiometric number of electrons involved in
a	n electrode reaction
P	pressure
Q	charge passed in electrolysis
R	(a) gas constant
	(b) resistance
R_{ohmic}	ohmic resistance
Rp	polarisation resistance
Rs	series resistance
Welec	electric work

Greek symbols	Symbol Meaning
$\propto$	transfer coefficient
η	overpotential
η_{ohm}	ohm ohmic overpotential

CHAPTER I
INTRODUCTION

1.1 Introduction and Motivation

Solid oxide fuel cell (SOFC) is one of the most popular type of fuel cells nowadays due to its widest range of application (from a small unit to the large scale power plants) ,high system efficiency, fuel flexibility and low emissions [1-3]. In addition, SOFC may be considered as a chemical reactor depending on the operating modes, i.e.,1 (i) only electricity generation which totally converses fuel into carbon dioxide and water, (ii) cogeneration of useful chemicals and electrical power by proper selection of the anode electrode and the fuel [4]. The second mode is extremely interesting for fuel conversion into useful chemical by electro co-generation process e.g.. ,styrene production from ethylbenzene [5], oxidation of methanol to formaldehyde [6], production of nitric oxide from oxidation of ammonia [7], oxidation of hydrogen sulfide to sulfur dioxide which is a basic step of the manufacture of sulfuric acid [8], production of hydrogen cyanide from oxidation of methane and ammonia [9] and oxidative coupling of methane (OCM) to C2 hydrocarbons [1, 10]. Therefore, this research will focus mainly on chemical and electrical power co-generation by high temperature SOFCs.

Methane is the main component in natural gas and a byproduct from oil refining and chemical processing. Furthermore, it appears to be the cheapest and most available carbon source for the direct conversion of natural gas, as well as it is the convenient transportable products. As the result, OCM to C2 hydrocarbon (i.e., ethane and ethylene) is a promising attractive process for utilizing methane. Since

the pioneering work of Keller and Bhasin, they have been widely interested to production of C2 hydrocarbons from OCM reaction [11]. A wide variety of catalysts have been studied such as Na_2O_2, Na/La_2O_3, La_2O_3, Ba/MgO and Na_2WO_4 [12-14]. However, the yield of C2 hydrocarbons achieved in a fixed-bed reactor (FBR) was limited to about 25% due to the presence of undesired complete oxidation in the gas phase and partially on the catalyst surface [12, 13]. To overcome this limiting problem, selective catalysts for the methane coupling reaction and SOFC reactor had been designed to inhibit the side reactions. However there are a few researches reveled SOFC reactor to produce C2 hydrocarbons. The use of SOFC reactor for co-generation of C2 hydrocarbons and electric power was first reported by Pujare and Sammells, they studied the OCM by using the cell $Pt/Sm_2O_3/La_{0.89}Sr_{0.10}MnO_3/YSZ/La_{0.89}Sr_{0.10}MnO_3/Pt$. High selectivity to C_2 hydrocarbon (>90 %) was achieved although the methane conversion was relatively low [13]. Carrillo *et al.* was studied oxidation of methane on Ni/ZrO_2 anodes in a SOFC reactor, Ni/ZrO_2 cermet prepared by the mist method was selective for the OCM reaction with high C2 hydrocarbon selectivity (70-80%) was produced but the methane conversion was low (3-8%) [10]. Hence, a development of anode catalysts for an oxidative coupling of methane in SOFC becomes an important goal to improve the conversion, selectivity, yield and stability of the reactor. Addition, the anode material must require good electronic conductivity, high electrochemical activity and structural stability properties [15].

A large number of anode catalysts have been evaluated for their performance in the OCM in SOFC reactor such as Bi_2O_3–Ag [16], Bi_2O_3-Pr_6O_{11} [17], $BaCO_3$–Au [18], $LaAlO_3$ [19] and other oxides [20]. Gold-based catalysts is very high activity although gold has been thought for a long time to be chemically inert, it has

been found that its catalytic performance is significantly affected by the size of the Au particle [6-9]. When gold nanoparticle is deposited on select metal oxides [10-14] as ultra-fine particles, promising found that its chemistry dramatically changes because addition of metal oxides stabilizes the average gold particle size, close contact between gold and metal oxides is expected [6, 7, 11]. The enhancement of catalytic activity and stability of supported gold catalysts has been reported to depend on dispersion, supports and preparation method [5, 13]. White *et al.* suggested that the design of anode catalysts has referred to basic knowledge of heterogeneous gas phase catalysis and suggested perovskite oxides as the anode catalyst [21]. Perovskite structure (ABO_3) anode materials have received much attention because of their mixed electronic and ionic conduction behaviors that make the triple-phaseboundary (TPB) extend to the entirely exposed anode surface. Among the variety of these oxides, $LaSrMnO_3$-based perovskite compounds are promising Ni-free anode candidates due to their high chemical stability at high temperatures under both oxidizing and reducing atmospheres, and strong resistance to carbon deposition [22-24]. However, they suffer from the disadvantages of low electronic and ionic conductivities and poor catalytic activity. The sufficient electronic and ionic conductivities are indispensable to reduce the electrode polarization and thus promote the electrode reaction process. There are many efforts to enhance the electronic and ionic conductivities of $LaSrMnO_3$ material. For example donor doping on the Mn site of $LaSrMnO_3$ with perovskite structure could improve the electrical conductivity [25-29]. S.W. Tao and co-worker reported the increasing in electrical conductivity of doping on the Mn site of $LaSrMnO_3$ .Moreover doped-chromium on Mn site is suitable for high temperature operation (750-900°C)

because Cr doped $LaSrMnO_3$ played a vital role in increasing resistance to coking (as well as raising sulphur tolerance) [30].

In recent years, the conductivity properties of $LiFeO_2$ with similar rock-salt structure to $LiCoO_2$ have been largely revealed [31]. It indicated that $LiFeO_2$ are potentially very attractive electrode for rechargeable lithium batteries because of theirmuch lower cost and toxicity compared with $LiCoO_2$ used in the vast majority of present day cells. Morales and Santos-Peña have studied $LiFeO_2$ as potential alternative electrode to $LiCoO_2$. [32], they reported that lithium iron oxide increases the electrochemical activity of the cell. In addition, a lithium-doped magnesium oxide,

Li/MgO, has been extensively studied as catalysts for the OCM reaction [33-38], Lunsford et al. suggested that this reaction was accelerated on the $[Li^+O]$ species formed on the catalyst surface [39]. T. Miyazaki et al. also reported the study of alkali-doped transition metal [40]. This report pointed out that $LiFeO_2$ contained components had good efficiency with OCM reaction based on a redox mechanism involving lattice oxygen anions. From this result, it demonstrated that the $LiFeO_2$ can be applied directly to the design of suitable anode catalysts for C2n hydrocarbon.

Therefore in this study, Au/LSM, LSCM, Ce/LSCM and $LiFeO_2$ were investigated as a new anode catalysts for OCM to C2 hydrcarbon in SOFC reactor. The surface morphology, composition and surface area were characterised by several techniques. The preparation of anode cell has been examined by various techniques. The catalytic activity of catalysts for OCM reaction was both studied in fixed bed and SOFC reactor. A plate type YSZ was used as a solid electrolyte and $La_{0.85}Sr_{0.15}MnO_3$

(LSM), $La_{0.8}Sr_{0.2}FeO_3$ (LSF) or $La_{0.6}Sr_{0.4}CoO_{3-\delta}$ (LSC) was used as a cathode material. Special investigation was given to of the anode catalyst.

1.2 Objective

The objective of this research was to study the OCM over various catalysts for use as an anode in an SOFC reactor, aiming to gain high conversion, selectivity of C2 hydrocarbon.

1.3 Outline of Dissertation

In this dissertation, experimental investigations for OCM over various catalysts based on electro cogeneration in SOFC reactor are as follows: The first challenge was development the $La_{0.4}Sr_{0.6}MnO_3$ (LSM) and Au/ $La_{0.4}Sr_{0.6}MnO_3$ material for oxidative coupling of methane reaction. The second challenge was catalytic reaction of oxidative coupling of methane reaction by $La_{0.25}Sr_{0.75}Cr_{0.5}Mn_{0.5}O_3$ (LSCM) and 5%Ce/LSCM material. The last challenge was to introduce the $LiFeO_2$ (LFO) material for OCM reaction.

CHAPTER II
BACKGROUND

2.1 Oxidative coupling of methane (OCM) reaction

2.1.1 Definition

The oxidative coupling of methane (OCM) is a type of chemical reaction that directly converts methane into value-added chemicals. It is the ethylene formation process by the coupling of two methyl radicals after the abstraction of the hydrogen atom from each methane molecule. However, the selectivity of ethylene is always diminished due to the directly formation of carbon oxides from the combustion of methane and C2+ products with the presence of oxygen that acts as an oxidizing agent of catalyst.

2.1.2 Oxidative coupling of methane reaction

The oxidative coupling of methane (OCM) to ethane and ethylene has been pioneered by Keller and Bhasin [11] (which was based on the use of reducible metal oxide catalysts) and Lunsford and Ito [41] (which was based on the use of non-reducible metal oxide catalyst; Li-MgO). The following selective and nonselective reactions occur simultaneously in the OCM process (800 °C) [42].

$$2CH_4 + 0.5O_2 \rightarrow C_2H_6 + H_2O + 174.2\ kJ/mol(C_2H_6) \quad (2.1)$$

$$2CH_6 + 0.5O_2 \rightarrow C_2H_4 + H_2O + 103.9\ kJ/mol(C_2H_4) \quad (2.2)$$

$$C_2H_6 \rightarrow C_2H_4 + H_2 - 114.6\ kJ/mol(C_2H_4) \quad (2.3)$$

$$CH_4 + 2O_2 \rightarrow CO_2 + 2H_2O + 801.6\ kJ/mol(CO_2) \quad (2.4)$$

$$CH_4 + 1.5O_2 \rightarrow CO + 2H_2O + 519.1\ kJ/mol(CO) \quad (2.5)$$

$$C_2H_6, C_2H_4\ and\ H_2 \rightarrow CO, CO_2 and\ water + large\ amount\ of\ heat \quad (2.6)$$

The oxidative methane activation in the catalytic OCM process involves an abstraction of H-atom from methane, leading to the formation of methyl radicals on the catalyst surface. After that the two desorbed methyl radicals are coupled in the gas phase to form ethane molecule as show in Fig. 2.1 [43].

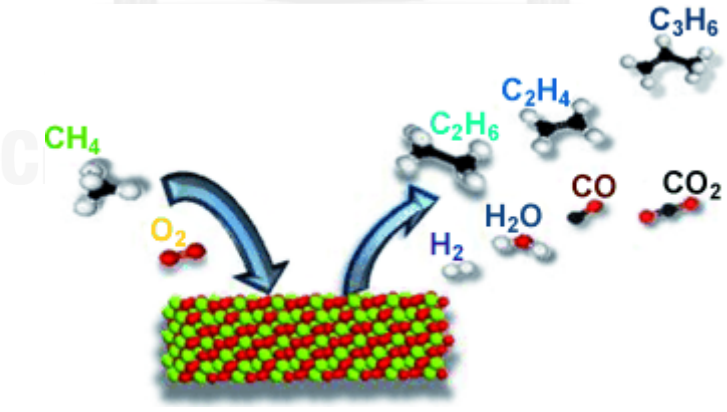

Figure 2.1 Oxidative coupling of methane reaction [44].

Although the research on OCM process has been extensively done but it has not been commercialized yet because of the following main limitations:

(1) The operating temperature is quite high (750–1000 °C) hence, it requires a high thermal and hydrothermal stability of catalyst. Therefore, the catalysts deactivation is a serious problems for developing a commercial catalyst in this process.

(2) The desired products (C2 hydrocarbons) can only be obtained at low methane conversion.

(3) At high ratio of CH_4/O_2 in feed, the selectivity of C2 hydrocarbons is high but the methane conversion and ethylene/ethane product ratio are low [3]. However, at low ratio of CH_4/O_2 in feed, not only the selectivity of C2 hydrocarbons is low but the process also becomes more severe because the nonselective highly exothermic hydrocarbon combustion occurs simultaneously to a larger and larger extent.

(4) The concentration of ethylene in the product stream of OCM is low and hence, the cost of ethylene separation is high, resulting in the separation uneconomical.

2.2 Fuel Cell Principles

2.2.1 Basic Principles

Fuel cell is the electrochemical device that directly converts the chemical energy to electrical energy. The basic physical structure of fuel cell consists of a porous anode and a cathode that are separated by the electrolyte layer. Typical fuel

cell is showed in figure 2.2, fuels are fed continuously to the anode compartment (negative electrode) and an oxidant (i.e., oxygen) is fed continuously to the cathode compartment (positive electrode); the electrolyte allows the passage of the ions, while the negative charges of electron pass around an external circuit resulting in the electric current.

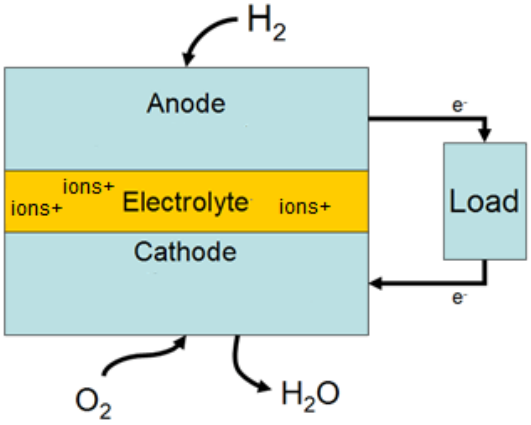

Figure 2.2 Schematic of a fuel cell

2.2.2 Types of Fuel Cells

Fuel cells are different according to the electrolyte employed and the operating temperature. It can be classified into 6 major groups, Alkaline Fuel Cell (AFC), Phosphoric Acid Fuel Cell (PAFC), Solid Oxide Fuel Cell (SOFC), Molten Carbonate Fuel Cell (MCFC), Proton Exchange Membrane Fuel Cell (PEMFC) and Direct Methanol Fuel Cell DMFC, based on the choice of fuel and electrolyte [2]. Table 2.1 shows the different types of fuel cells, classified by the electrolyte employed together with their main characteristics [45], The details of SOFC technology will be described in the next section.

Table 2.1 Types of fuel cell divided by the electrolyte and temperature functionalized.

	AFC	PEMFC	PAFC	MCFC	SOFC
Temperature (^{o}C)	60-90	80-110	160-200	600-800	800-1000
Electrode material	metal or carbon	Pt on carbon	Pt on carbon	Ni+Cr	Y_2O_3-ZrO_2
Electrolyte	NaOH/KOH	polymer membrane	H_3PO_4	$LiCO_3$-K_2CO_3	ZrO_2 with Y_2O_3
Primary fuel	H_2	H_2 reformate	H_2 reformate	H_2/CO reformate	H_2/CO/CH_4 reformate
Oxidant	O_2/Air	O_2/Air	O_2/Air	CO_2/O_2/Air	O_2/Air
Efficiency (%)	60	60	55	55-65[a]	60-65[a]

2.2.3 Solid Oxide Fuel Cell

SOFCs have recently emerged as a high temperature fuel cell technology. It provides the extremely useful in large scale, high-power applications such as the industrial stations and the electricity-generating stations. SOFC technology is the most demanding from a materials standpoint and it is developed for the potential market competitiveness that arising from [2]:

-It is the most efficient fuel cell electricity generators that currently being developed world-wide.

-It is flexible in the choice of fuel such as natural gas.

-It is the most suitable technology for the distributed generation market (i.e. stationary power) because its high conversion efficiency provides the greatest benefit when fuel costs are expensive because of the long time of delivery systems to customer.

-It has a modular and solid state construction without any moving parts. Therefore, it can be installed indoors.

-The high operating temperature of SOFC produces the high quality by product heat which can be used for many applications such as co-generation or the combined cycle applications.

-It does not contain any noble metals that could be have some problems in the resource availability and the price issue for high volume manufacture.

-It does not have any problems with the electrolyte management like the liquid electrolytes such as corrosive and the difficult to handle.

-It has extremely low emissions by eliminating the danger of carbon monoxide in exhaust gases, as any CO produced is converted to CO_2 at high operating temperature.

Nowadays, SOFC is the best suited for provision of power in the utility applications due to its high efficiency and low emission.

2.2.3.1 Principle of SOFC

The operating principle of SOFC with an oxygen ion conductor is schematically showed in figure 2.3. SOFC consists of three basic components; anode,

cathode and electrolyte. The electrolyte that is inserted between anode and cathode has been usually made of a hard ceramic such as zirconia. Fuel such as hydrogen or carbon monoxide is fed to the anode side which undergoes an oxidation reaction hence, releases the electrons to the external circuit. Oxygen from air is fed to the cathode side and accepts the electrons from the external circuit then, it undergoes a reduction reaction. The chemical and electrochemical processes often take place preferentially at the certain surface and the interfacial sites or triple-phase boundaries (TPBs).

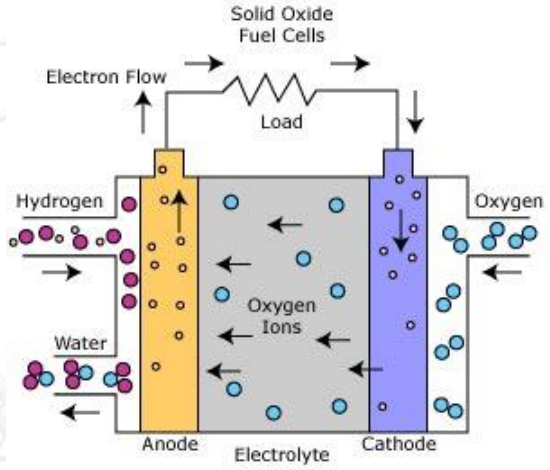

Figure 2.3 Principle of operation of SOFCThe electrochemical reactions occur as presented below:

Anode $H_2 + O^{2-} \longrightarrow H_2O + 2e^-$ (2.7)

Cathode $1/2O_2 + 2e^- \longrightarrow O^{2-}$ (2.8)

Overall $1/2O_2 + H_2 \longrightarrow H_2O$ (2.9)

Alternatively, a proton conducting solid electrolyte can be used, where H_2 is oxidized to produce protons which subsequently react with oxygen to form water. In some case, CH_4 can be oxidized directly on the anode side to from CO_2 and H_2O.

However, when a fuel cell is operated, the actual output voltage is less than that from the thermodynamically predict. This voltage drop resulted from four major irreversibilities or losses as follow [46]:

- Activation losses (losses from the electrochemical reaction)

This loss results from the slowness of the reactions taking place on the electrodes surface. The slow step could come from many possibilities such as the adsorption of reaction to the electrode catalyst surface or the desorption of products. However, the reaction rate is rapid at high operating temperature of SOFC. Therefore, the activation loss is usually small.

- Ohmic losses (losses from the resistance)

This loss is compose of the resistance of the electrons flow though the electrodes material and the various interconnections, the resistance of the ions flow though the electrolyte and the contact resistance between the cell components. It is essentially linear and proportional to the current density called “ohmic” losses.

- Mass transport or concentration losses

Mass transport or concentration losses appears when the electrode reaction is hindered by mass transport effects. This results from the change concentration of reactants at the electrodes surface and it becomes more severe as the degree of conversion increases. This loss can be minimized by increasing the feed velocity of reactants and/or removing the velocity of the reaction products.

- Fuel crossover and internal currents

This loss results from the waste of the fuel passing through the electrolyte or the electron conduction through the electrolyte. In fact, the electrolyte should be transported only by the ions though the cell. However, a certain amount of fuel diffusion or electron flow will be possible in some case. The fuel loss and current flow are usually small.

2.2.3.2 Cell component

The conventional material and the required properties of each component in SOFC system can be divided into three major parts.

2.2.3.2.1 Electrolyte

The current transfer in solid electrolyte involves the movement of oxygen ions (O^{2-}) vacancies. A criteria to select an electrolyte is its ionic conductivity, which is the temperature dependent. Ceramic ion conducing electrolytes are available for operating over a wide range of temperature between 500 to 1,000 °C. The required properties of electrolyte are high ionic conductivity, low electronic conduction and phase stability over a wide range of temperature and oxygen partial pressures. In addition, they must have the thermal expansion coefficient compatible with those of electrodes and interconnection materials, low volatilization of components, suitable mechanical properties, moderate materials and fabrication cost and negligible interaction with electrode material under operation and fabrication conditions.

Three types of electrolyte namely yttria stabilized zirconia (YSZ), strontium, magnesium-doped lanthanum gallate (LSGM), and gadolinium- or samarium-doped

ceria (CGO or CSO) have been widely investigated for SOFCs [35]. Yttria-stabilized zirconia (YSZ) is one of the most popular SOFC electrolytes for high temperature because of the low cost, its desirable chemical stability in both oxidizing and reducing atmospheres, low electronic conductivity and high mechanical strength. The oxygen ion conductivity of YSZ is high enough for SOFC operated at the temperatures above 800 ^{o}C. Therefore, YSZ is suitable for use as an electrolyte material at high temperature SOFC. However, at low operating temperature, Scandia-stabilized zirconia (ScSz) and gadoliniam-doped ceria (CGO) were found to exhibit the higher oxygen ion conductivity than the traditional YSZ material. They are attracting much attention as the electrolytes for intermediate temperature SOFCs [47, 48].

2.2.3.2.2 Electrode

Electrode is the critical components in SOFCs. It provides the interface between the chemical energy associated with fuel oxidation and electrical power. Typically, It is the complex structures that consists of a three-phase percolating composite of a metal or mixed conducting oxide, an oxide electrolyte and the pore space [49]. The cathode acts in the oxidation atmosphere where the oxygen molecules are reduced to the oxygen ions. Since it is the particularly strong oxidizing environment at high temperature then, it is not possible to use the low cost metals. The noble metals, semi-conducting oxides, or conducting metal oxides are more favorable. The anode acts in the reducing environment of the fuel gas and many types of metal can be used. Porous nickel is the most widely employed. However, its thermal expansion is considerably larger than that of YSZ hence, it can be sintered at the cell operating temperature resulting in the fuel electrode porosity

reduction. This problem can be solved by mixing porous nickel with YSZ. Since YSZ can prevent the sintering of the nickel particles, decrease the fuel electrode thermal expansion coefficient to nearly close to that of the electrolyte, and provide the better adhesion of the fuel electrode with the electrolyte. SOFC electrodes must meet the following requirement :

-Good electronic conductivity

-High electrochemical activity

-Good adherence to other cell components

-Chemical inertness

-Thermodynamic stability

-Low volatility

-Compatible thermal expansion with other call components

-Superficial resistivity $\leq$ 0.2 ohm/cm^2

-Ease of fabrication into thin porous layers that resist excessive sintering

-Good mechanical strength

-Moderate materials and fabrication costs

2.2.3.2.3 Interconnect

The interconnect material is used for electrically connect between the anodes and cathode of stacked cells in series. The primary function of interconnect

is to carry electrical current from the electrochemical cell to the external circuit. Therefore, the interconnect material must have the high electrical conductivity. The interconnect layer can use either the metallic or ceramic material which sits between each individual cell. Its purpose is to connect each cell in series in order to combine the electricity generated from each cell. Since the interconnect is exposed to both the oxidizing and reducing side of the cell at high temperatures then, it must be extremely stable. For this reason, ceramics have been accepted as a better material than metals in the long term operation. However, the cost of ceramic interconnect materials are very expensive. Nickel- and steel-based alloys become more promising materials when SOFC is operated at low temperature (600-800°C). Metallic 95Cr-5Fe alloy is a choice of material used for an interconnect contacting with YSZ. The most common inter-metallic material applied today is the doped lanthanum chromites. Ceramic-metal composites called 'cermet' are also under consideration, as they demonstrated the thermal stability at high temperatures and excellent electrical conductivity.

2.3 Co-generation of Fuel Cell: Chemical Production

As mentioned above, fuel cell is usually used as a power generator but it can be also applied as a chemical reactor. Previously, fuel cell reactors have been developed for the conversion of fuel to the desired chemicals as the main product with energy generation that is called chemicals and energy co-generation [2]. In this process, the main function of fuel cell likes chemical reactor. However, electricity generated as by-product from the fuel cell reactor distinguishes it from the conventional reactor. In addition, chemicals and energy co-generation provides a

benefit over a conventional fuel cell which just produces electrical and pure water as a by-product.

The typical concept of fuel cell reactor for chemicals and electrical power co-generation is illustrated in Figure 2.4. This system consists of fuel cell reactor, external load and chemical product recovery unit [2]. Fuel and oxidant are supplied separately to electrochemical cell (anode and cathode electrode) at fuel cell reactor, after that the useful chemical and electricity are occurred. Electricity is supplied to an external load and the useful chemical produced is collected. Cogeneration systems can operate at low, moderate or high temperatures; hence the electro-cogeneration process has become one of the new applications for fuel cell system.

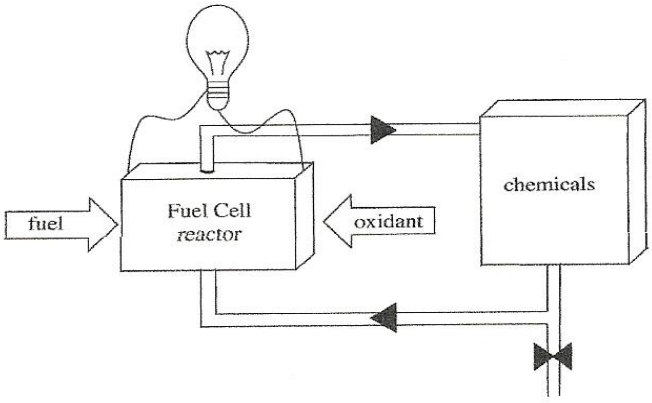

Figure 2. 4 Principles function of fuel cell to generate chemicals and energy

The main advantages of the chemical energy co-generation methods over the conventional catalytic reactors are as follows:

• The production in the electrochemical reactor is essentially controlled by cell potential;

• Cogeneration processes can operate at low, moderate or high temperatures;

• No competition for the same catalytic sites, since the reactants are fed separately;

• The suitable selection of anode material and the fuel allow controlling a successful

chemical generation;

• The selectivity of the process can be controlled by potential variation or the type of catalyst used in the electrode.

Therefore, the electrical energy cogeneration and the useful chemicals have become a more attractive application not only in term of energy conversion, but also in term of the environmental standpoint. The choice of the fuel cell type for the determined cogeneration processes depends mainly on the temperature. Therefore, the exploratory evaluation of fuel cells as reactors for producing chemicals has been studied in these temperature ranges. For example, hydroxylamine, acids [6], and hydrogen peroxide [8] have been produced from inorganic reagents using different media in aqueous electrolyte fuel cells at low temperature. Fuels has been converted to the useful chemicals, such as 1-propanol, and cyclohexlamine in PEMFC reactors [50], which also operate at low temperature. On the other hand, electrochemical oxidation of methane to gas synthesis or C2

hydrocarbons with electricity in SOFC reactors is a very attractive alternatives to conventional catalytic reactors.

2.3.1 Solid Electrolyte Membrane Reactor

A solid electrolyte membrane reactor, consists in a fuel cell applied as chemical reactor, has a membrane selectively permeated by at least one of the mixture components that it is exposed to. In this reactor, at least one of the reactants or products are supplied or removed partly or wholly through a membrane. This means that the membrane serves as the wall or as a part of the reactor wall. The membranes can be classified into two types according to permselectivity and permeability; porous and dense membranes. Porous membranes offer a high permeability to molecules with low permselectivity. The typical gas transport mechanisms in the porous membranes are in the following steps: molecular diffusion and viscous flow, capillary condensation and Knudsen diffusion as well as surface diffusion. Porous membranes have been widely successfully employed in many oxidation reactions such as oxidative coupling of methane [10], oxidative dehydrogenation of ethane, propane [11], etc.

On the other hand, dense membranes have a rather high permselectivity to some special species but it usually has a lower permeability compared to porous membranes. The transport process in the dense membrane involves the oxygen diffusion or ionic jumping in the lattice. The solid oxide dense membranes can be classified into two types: solid electrolytes and mixed ion electron conductors (MIEC). Unlike MIEC, the dominant characteristic of the solid electrolytes is the ionic conductivity. In fact, it is usually two or more orders of magnitude higher than the electronic conductivity [14]. Therefore, their classification is based on the conducting

ion. Many conductors have been discovered (H^+, K^+, Na^+, Cu^+, Ag^+, Li^+, O^{2-}, and F^-). However, H^+ and O^{2-} ion conductors have been mainly used in the solid electrolyte membrane reactors (SEMRs) [51, 52].

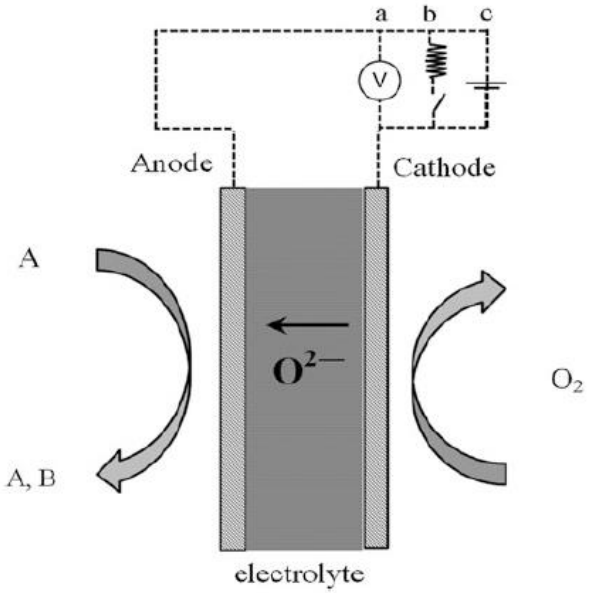

Figure 2.5 Schematic diagram of a SEMR: a open-circuit operation; b closed-circuit operation in fuel cell mode; c closed-circuit operation in ‘‘pumping’’ mode [53].

The typical configuration of a SEMR is illustrated in Figure 2.5; the membrane is an oxygen-ion conductive solid electrolyte. The cathode is exposed to the oxygen-containing gas, e.g., air, and the anode is exposed to the reactants, e.g., hydrocarbons. Two electrodes are connected to a circuit in three operation modes. For open circuit operation, two electrodes are connected to a voltmeter (case1a). In closed-circuit operation, two electrodes are connected to an external resistive load (case 1b). Another type of the closed-circuit operation was showed in case 1c, two electrodes are connected to an external power source which is called

electrochemical oxygen ‘‘pumping’’. In the open-circuit operation, there is no net current through the electrolyte. The difference in chemical potential is converted into the open-circuit electromotive force of the cell. If the primary goal is the production of electricity, the fuel cell will operate in the closed-circuit operation in order to directly convert chemical energy into electrical energy. This latter is also called fuel cell mode of operation. On the other hand, if the primary goal is the production of B chemicals, an external power source can be used to impose a current through the cell in the desired direction (case 1c). These operation modes generate three basic applications of the SEMRs as follow figure 2.5.

1. Solid Electrolyte Potentiometry (SEP),

2. SOFCs, and

3. Electrochemical oxygen ‘‘pumping’’.

The solid electrolyte potentiometry can be applied to study the heterogeneous catalysis by the measurement of the activity of oxygen on metal and metal oxide catalysts. The basic principle of SEP is the in situ measurement of the chemical potential difference between two electrodes on either side of a solid electrolyte at open-circuit conditions. SOFCs combine the concepts of a fuel cell and a chemical reactor to produce valuable chemicals from the anodic reaction with cogeneration of electrical energy instead of pure thermal energy several fuels such as H_2, CO, CH4, and CH3OH can be used in SOFCs because it can be operated at high temperatures. In electrochemical oxygen ‘‘pumping’’, the SEMR operates under closed circuit conditions to carry out a reaction and produce the useful chemicals rather than electrical energy. When the current is generated spontaneously in the

undesired direction, an external power source is used to direct and control the current. Solid electrolyte membrane reactors present several advantages such as: increase the catalytic activity and selectivity, simultaneous reaction and separation in the same device, better process integration, reduce feedstock, and easy reaction rate control [15].

2.4 A brief overview of tape casting process

Tape casting is a well known process for fabricating thin and flat sheets/films of ceramic and metallic materials. Large-area films with controlled thickness can be easily produced. Presently, tape casting is a well-established forming technique for fabricating large, thin, and flat ceramic or metallic sheets [54]. It is also known as "doctor blading"[55-57]. The doctor blade is the scraping blade that removes the excess slurry on the moving polymer carrier to produce a thin layer of tape. Tape casting is an easy and low cost process that is widely used in the plastic, paper, paint and electronic industries. The flexibility of unfired tapes allows them to be punched with holes, cut into various shapes. Using this process, a multi-layer ceramic can be prepared by lamination and co-sintered at the same firing temperature. Therefore, it is possible to prepare a multi-layer ceramic composed of layers having different porosities. Porous ceramics can be generated by the addition of pore formers that may or may not be pyrolysed. The former type combusts during high-temperature treatment, while the latter type remains in the fired tape ,and needs a separate step for removing it e.g. acid leaching for NiO pore former [58].

Slurry formation is a very crucial step for tape casting. The slurry must satisfy some quality criteria such as no agglomerations and sediments, and have a good viscosity to allow for an easy casting while maintaining the geometry of the tape. The

wet casted slurry must not have any defects during drying. The dried green (unfired) tape should be flexible to avoid cracking of the tape while handling it. It should also have good cohesion and thermo-compression for laminating layers together. This requires a carefully selected mixture of powder, solvent, surfactant, plasticizer, binder and sometimes pore formers.

2.4.1 Tape slurry ingredients

In order to understand how ceramic particles and pore formers can be stabilised in a cast tape, brief details of tape slurry components are given below.

2.4.1.1 Solvent

Tape casting is a forming process that requires the powder to flow like a fluid. In order to achieve this, the powder is suspended in the solvent. The solvent is also referred to as the vehicle or the carrier. The solvent is used to distribute all ingredients homogeneously throughout the slurry [59]. Therefore, the solvent is a very important parameter in formulating the slurry. In tape casting, non-aqueous solvents are commonly employed due to their low latent heat of evaporation and low surface tension compared with water. The solvent must dissolve all additives such as wetting agent, surfactant, dispersant, binder, and plasticizer. There is a wide range of solvent selection but the possible selection of a solvent depends on the chosen additives [60, 61]. It is common for the vehicle to have more than one solvent to dissolve all ingredients because it increases the ability to dissolve [62, 63]. It has been reported that a vehicle mixture containing up to four different type of solvent has been used [64]. Following the previous work of Irvine and co-workers

[65], a binary solvent system of methyl ethyl ketone (MEK)/ethanol was used here. Some physical and dielectric properties of ethanol and MEK are shown in Table 3.1.

Table 2.2 Physical and dielectric properties of ethanol and methyl ethyl ketone [66].

Solvent	Boiling point (^{o}C)	Dielectric constant at 20 ^{o}C	Heat of evaporation (kJ/mol)
Ethanol	78	25.3	38.6
MEK	80	18.5	31.3

2.4.1.2 Surfactant

A surfactant is also called the wetting agent, dispersant, or deflocculant. It is used to break down the agglomerates in the power by separating the particles and coating them individually to prevent re-agglomeration [66]. The surfactant coats the particles and keeps them in a stable suspension in the slurry due to the steric and/or electrostatic repulsion [67]. The deflocculant is used to the increase the solid loading of the slurry while maintain a desired viscosities after the addition of binder [68]. Some of the deflocculants used for tape casting are fish oil, corn oil, safflower oil, and linseed oil [69].

2.4.1.3 Binder

Binder is an important additive for the tape casting process. The binder function is to hold the entire chemical system together. The green tape is supported by the continuous chain of polymer that is infiltrated with a large amount of powder [70]. Some important factors to be considered in selecting the binder are solubility in

solvent, viscosity, strength, burn out characteristics, firing atmosphere of the powder, ash residue and cost. Most binders are either polyvinyl (vinyl) or polyacrylates (acrylic). Generally, a binder is introduced into the tape slurry after the dispersion step to avoid competitive adsorption with the dispersant on the particle's surface. In addition, the presence of high molecular weight binder increases the viscosity of the slurry, which would not be suitable for particle dispersion step. Some important factors to be considered in selecting the binder are solubility in solvent, viscosity, strength, burn out characteristics, firing atmosphere of the powder, ash residue and cost. Most binders are either polyvinyl (vinyl) or polyacrylates (acrylic). The most commonly used vinyl for tape casting is polyvinyl butyral (PVB) [70]. Since polyvinyl alcohol is soluble in water, it is generally considered for aqueous-based slurry.

2.4.1.4 Plasticizers

The plasticizer is an additive which softens the binder to provide flexibility to the green tape. Without the plasticizer, the slurry will form a strong, stiff and brittle sheet of green tape. These plasticizers are comprised of low molecular weight organic substances that can soften the binder effect by dissolving homogeneously with the binder and inserting their small molecules inside the macromolecular network formed by the binder. The plasticizers offer the flexibility that allow the dry tape to be rolled, cut, punched, and laminate without cracking. The plasticizers are made up of small low weight organic substances that soften the tape by breaking then relinking the framework formed by the binder [56]. While the plasticizers increase the flexibility of the network, they reduce the mechanical strength of the green tape. Two plasticizers suitable for the PVB binder used here are polyethylene glycol (PEG) and dibutyl phthalate (DBP)

2.4.2 Preparation of Slurry

The slurry preparation usually consists of two-stage milling and mixing procedures. The first stage is the powder dispersion milling procedure where the powder is milled in a mixture of solvent and dispersant to break down soft agglomerated that have formed as a results of high surface area. Following the previous work of Irvine and co-workers [65]. This milling process takes about 24 hours to obtain a well-dispersed particle suspension. In the second stage, the binder and plasticizers are added to the suspension to form flexible bonding between ceramic particles. These additives increase the viscosity and plasticity of the slurry to enable a smooth casting. Once the binder and plasticizers are added, the mixing process can take as little as 4 hours or as long as 12 hours [71].

2.4.3 De-Airing

When all ingredients are mixed homogenously, it is essential to de-air the slurry to remove any air that is trapped during the milling and mixing process. Trapped air bubbles create pinholes that can lead to cracking upon drying. Generally, the slurry is de-aired by rolling the slurry slowly to decrease the viscosity and allowing the air bubbles to escape. However, this process can take up to couple of hours depending on the volume of the slurry. Another way to de-air is to use the vacuum pump to force the air bubbles to surface. However, it is important to vacuum at a low constant pressure for a short period to prevent a large amount of solvent from being removed.

2.4.4 Casting process

A typical tape caster is shown in Figure 2.6 It contains a slurry container (also called a reservoir), a stationary doctor blade and a moving carrier. In the casting

process, the doctor blade is firstly adjusted to provide a gap between the blade and the carrier film. The slurry or slip is poured into the reservoir behind the doctor blade and the tape is being casted onto the moving carrier. The wet thickness of the tape depends on the gap between the doctor blade and the carrier. However, the viscosity of the slurry, the level of the slurry in the reservoir and the speed of the moving polymer film can affect the wet thickness of the tape. In addition, it is important to maintain a constant temperature during the tape casting process. It is even recommended to tape cast in an environment that is warmer than room temperature to lower the viscosity of the slurry for a more consistent and smoother flow.

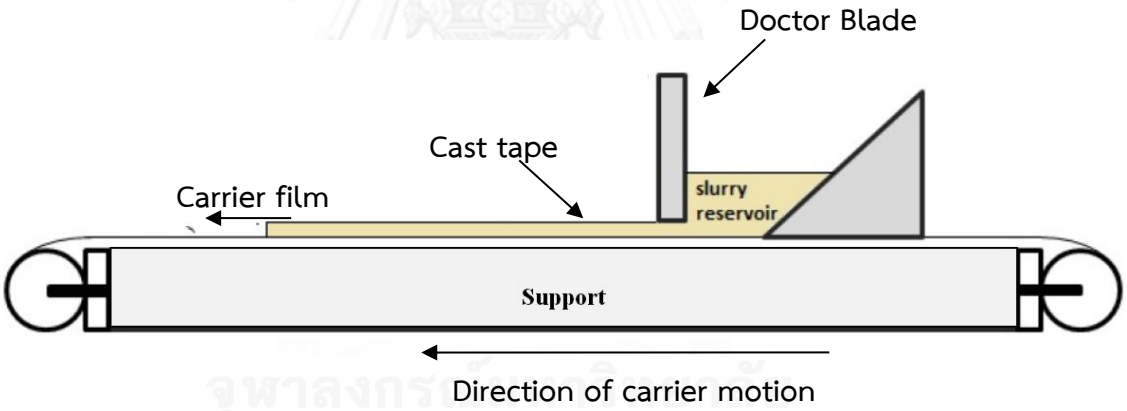

Figure 2. 6 Schematic of a tape casting machine.

2.4.5 Tape drying

Once the slurry is casted, it is important to let the wet tape dry at room temperature on the support for several hours to allow the solvent to evaporate. Blowing air into the drying chamber can speed up the drying process. However, inappropriate evaporation rate of the solvent may form cracks, drying crust, and skin on the surface of the tape [71].

2.5 Cell Fabrication

2.5.1 Shaping and Sintering

The multi-layer structured button cell can be fabricated by laminating, pressing, cutting and punching the dried green tapes. Multiple layers of dense electrolyte material were cold laminated together using the laminator. A layer of the tape consisting of the same electrolyte material with graphite as pore former is pressed to each side of the laminated n-layer electrolyte. After sintering, the prepared tape-casted cell will have a dense electrolyte with two strong, stable and porous scaffolds(as shown in figure 2.7). For the green tape, ceramic particles are held together by a large amount of additive. These organic additives must be removed completely from the green tape before ceramic sintering. Co-sintering of a multilayered tape consisting layer that has pore former must also completely remove the pore former before sintering the ceramic. Appropriate heating rate and dwelling time should be chosen to avoid cracking and distortion to the sintering samples.

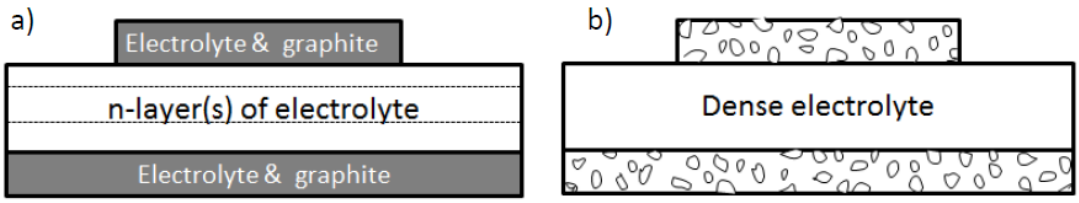

Figure 2.7 Schematic of the preparation of the tape casted cell a) before sintering and b) after sintering.

2.5.2 Infiltration

Recently, there are great interests in the development of nano-structured electrodes for SOFCs by the impregnation or infiltration method [61, 72-74]. Moreover, the nano-structured electrodes are critical for IT-SOFCs [25, 75, 76]. The infiltration of the functional material into the well-sintered and stabled scaffold allows low temperature calcination to form nano-particles and also to prevent undesired grain growth [73, 77, 78]. The continuous formation of nonrandom nano-particles on the scaffold also resolves the mismatch in thermal expansion coefficient (TEC) values between the electrode and the electrolyte. Nitrate solution of the chosen electrode material was used for infiltration. The cell was impregnated with the solution as shown in figure 2.8 then heated to 450 °C to decompose the nitrate. The infiltration and heat treatment process was repeated until the electrode reached the desired weight.

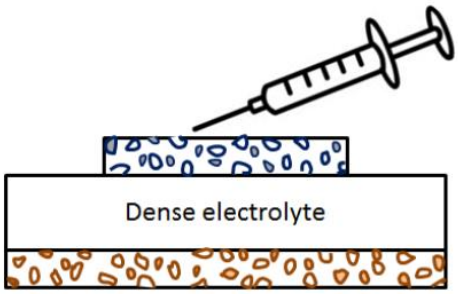

Figure 2.8 Schematic of the infiltration process

2.6 Characterization

2.6.1 X-ray diffraction (XRD)

Solid materials are crystalline substances where atoms are arranged in a unique and regular pattern. The simplest repeating building block in a crystal is called unit cell. X-Ray diffraction (XRD) technique can be used to map the unique pattern (fingerprint) of the crystalline material at the atomic and molecular level [79]. The X-Ray diffraction technique is versatile and non-destructive. It was first introduced by A. W. Hull in 1919 [80]. It is one of the most important characterization tools used in solid state chemistry and material science.

This measuring technique obeyed Bragg's Law (Eq. 2-10), where d is the distance between the atomic layers in the crystals, θ is the incident angle, n is an integer, and λ is the wavelength of the incident X-ray beam [81]. The X-ray beam (beam A and B) incidents on a pair of parallel planes that make an angle θ. The intensity of the reflected beam (beam A' and B') will be maximum when the waves are in phase (Figure 2.9).

$$2d\ sin\theta = n\lambda \qquad \text{Eq. 2-10}$$

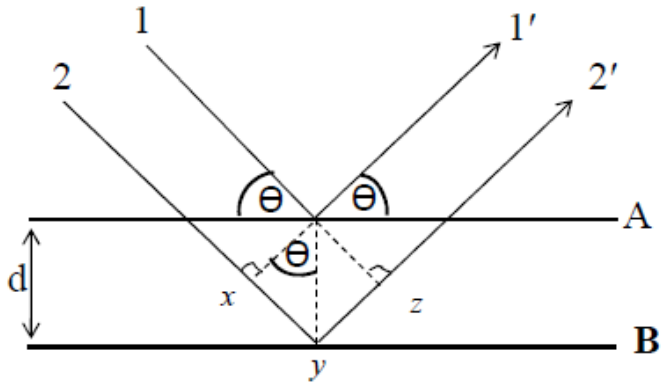

Figure 2. 9 Derivation of Bragg's law.

The X-ray diffraction pattern of each crystalline solid represents its 'fingerprint' which can be used to identify unknown crystalline materials by comparing with a reference source, Powder Diffraction File (International Center for Diffraction Data, USA).

2.6.2 Scanning Electron Microscopy (SEM)

Electron microscope is a type of microscope that uses an electron beam to capture an image of the specimen in high magnification. It is a powerful and versatile tool that allows one to observe the morphology of the specimen. The JOEL JSM-5600 scanning electron microscope (SEM) was used to observe the morphology of a sample. In the SEM, the tungsten filament of the electron gun emits an accelerated electron beam toward the specimen by applying a potential difference between 5kV and 30kV. The electron beam is then focused by passing through the magnetic lens (Figure 2.10). The scanning coil is used to control and adjust the emitted beam

before reaching the sample. An image is produced when the backscattered electron detector and the secondary electron detector detect the reflected electronic signal.

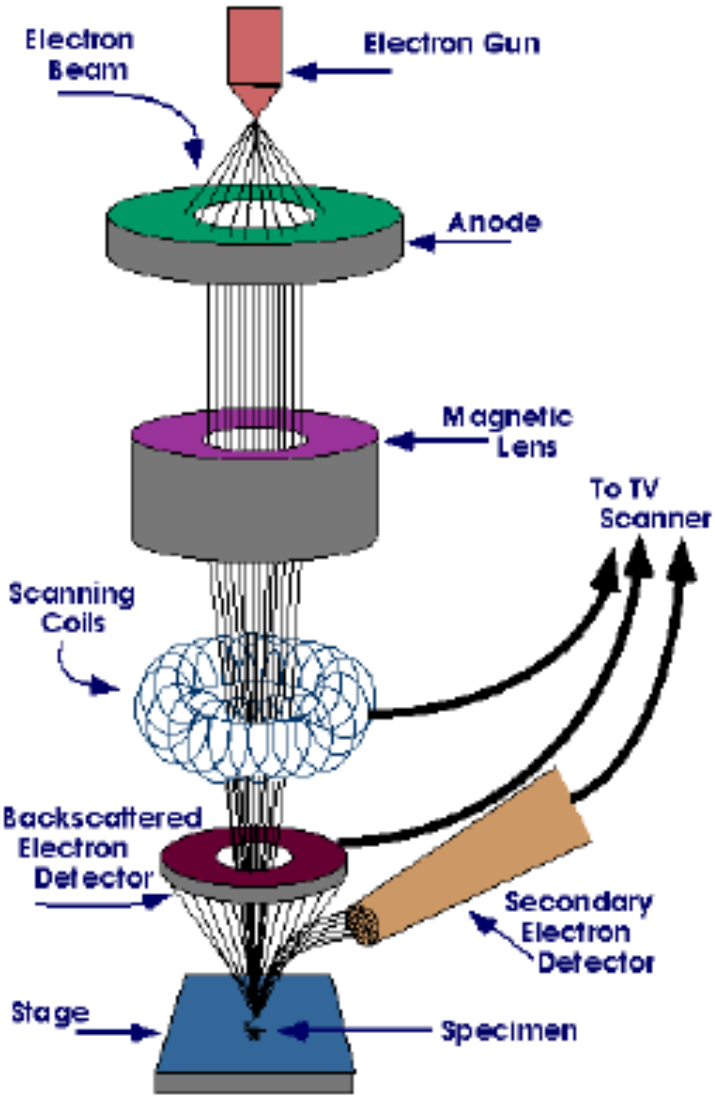

Figure 2.10 Schematic of SEM [82].

2.7 Electrochemical Measurements

2.7.1 Electrochemical Impedance Spectroscopy (EIS)

The electrochemical or impedance spectroscopy is a popular and powerful technique that is used to analyze and characterize the processes happening in the ceramic material. During the experiment, a small AC amplitude voltage signal, E(t) (Eq. 2-11), is applied to the system being studied over a range of frequencies (10^{-3} to 106 Hz). The AC current responses, I(t) (Eq. 2-12), of the system contain useful information about the interface, its structure and the electrochemical processes. In a linear system, the current response to the input potential signal will oscillate at the same frequency but shifted in phase Φ (Figure 2.11).

$$(t)=E_0\sin(\omega t)=E_0e^{j\omega t} \qquad \text{Eq. 2-11}$$

$$(t)=I_0\sin(\omega t-\Phi)=I0e^{j(\omega t-\Phi)} \qquad \text{Eq. 2-12}$$

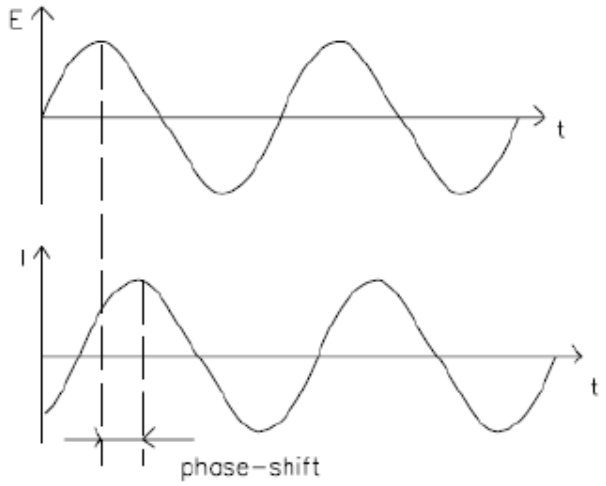

Figure 2.11 Phase angle shift of the current response signal to the voltage signal [83].

Impedance, Z(t), is defined as the ability of a circuit to resist the flow of electrical current. Using Ohm's law, Z(t) can be expressed as Eq. 2-13, which is composed of a real (Eq. 2-14) and an imaginary parts (Eq. 2-15).

$$Z(t) = \frac{E(t)}{I\,(t)} = \frac{E_{0e}jwt}{I_{0e}j(wt-\emptyset)} = \frac{E_0}{I_0}e^{j\emptyset} = Z_0\,(cos\emptyset + jsin\emptyset) \qquad \text{Eq. 2-13}$$

$$(Z)=|Z_O|\cos\Phi \qquad \text{Eq. 2-14}$$

$$-(Z)=|Z_O|\sin\Phi \qquad \text{Eq.2-15}$$

Since impedance is a complex vector, the magnitude and the direction vary as frequencies changes, which will be plotted in complex plane; the Nyquist plot (Figure 2.12). The semicircle in Figure 2.12 can be fitted with an equivalent circuit having a resistor, R, and a capacitor, C, in parallel (Figure 2.16). The relaxation time or time constant, **T**, provided by the RC parallel circuit is shown in Eq. 2-10. From this equation, RC are separable when the frequency of maximum loss, **ω**max (Eq. 2-17). The evaluated capacitance value reflects the corresponding processes of the material. Table 2.3 below lists the possible interpretation of the material. Electrochemical impedance plots often contain more than one semicircle. However, only part of the semicircle can be seen.

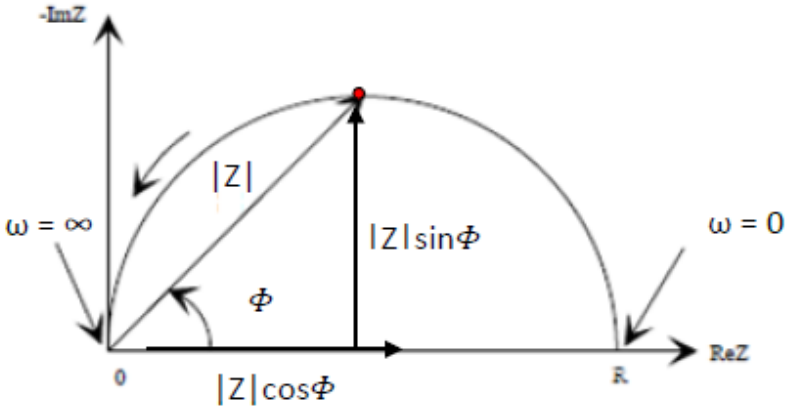

Figure 2.12 Impedance plotted in complex plane [84].

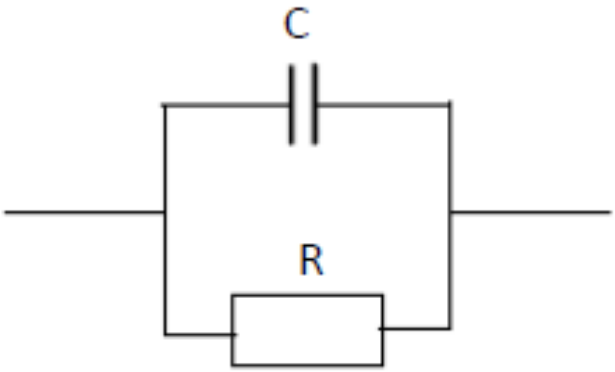

Figure 2.13 Equivalent circuit of semicircle[84].

$$\tau = \frac{1}{\omega_{max}} = RC \qquad \text{Eq.2-16}$$

$$1 = RC\omega_{max} \qquad \text{Eq.2-1}$$

Table 2.3 Relationship between capacitance values and corresponding processes [84]

Capacitance (F)	Corresponding processes
10^{-12}	Bulk
10^{-11}	Minor, second phase
10^{-11}-10^{-8}	Grain boundary
10^{-9}-10^{-7}	Surface layer
10^{-7}-10^{-5}	Sample-electrode interface
10^{-4}	Electrochemical reactions

CHAPTER III

LISTERATURE REVIEWS

3.1 Catalysts used for the Oxidative Coupling of Methane in Fixed Bed Reactor

From the pioneered work of Keller and Bhasin in 1982, more attention has been paid to the production of C2 hydrocarbons from oxidative coupling of methane. The effective catalysts are important for OCM, many studies have been focused on the design and the development of catalysts for OCM [15, 42, 43]. Table 3.1 shows a brief summary of various types of catalysts used for oxidative coupling of methane. A large number of catalysts, mostly bi-or multi-component mixed or supported metal oxides containing components with basic properties such as oxides of alkali metals, alkaline earth metals, rare earth metals, have been studied. The basicity surface of catalysts as a precondition of catalytic effectiveness was often noticed with heterolytic C–H bond splitting in methane. However, the activity and selectivity of the catalysts showe the dependence on both surface acidity and basicity but the relationship between the acidity/basicity properties and the catalytic performance was shown to be more complex. Stronger acid sites were found to be harmful for the C2 selectivity. In 1992, the Na_2WO_4–Mn/SiO_2 catalyst system was first reported by Li and his co-workers [85, 86] for the OCM. This system has received increasing attention ever since because of its excellent catalytic performance [86-88]. With this catalyst, it is possible to obtain up to 80% C2 selectivity at CH_4 conversion of 20% in a single-pass operation.

In case of Na_2WO_4–Mn/SiO_2 catalyst, two metal active site model has been proposed for OCM reaction. It was believed that the active oxygen species was the surface lattice oxygen Os^{2-} and two metal sites, $W^{6+/5+}$ and $Mn^{3+/2+}$, could be used to

explain CH_4 and O_2 activation. CH_4 was activated by Os^{2-} to generate the methyl radical on $W^{6+/5}$+ site, and the electron transferred from $W^{6+/5+}$ site to $Mn^{3+/2+}$ site, which was responsible for molecular oxygen activation to form surface lattice oxygen Os^{2-} as an active oxygen species for CH_4 activation. Moreover, 5 wt% Na_2WO_4 - 2 wt% Mn/SiO_2 (Na-W-Mn/SiO_2) is one of the catalysts that shows good performance in OCM and this material is stable up to 97 h of the operation [86]. Another attempt to study the correlation between the electrical properties and the catalyst performance over Na-W-Mn/SiO2 catalyst was reported by Malekzadeh et al. [89]. They compared the catalyst performance by varying the metal oxide loaded in Na_2WO_4/SiO_2. The results showed that MnO_x is the best oxide. It provided the highest electrical conductivity and increased the number of charge carriers between methane and the catalyst surface. Ji et al. proposed the Na-O-Mn and Na-O-W species for the active sites of the catalyst. It was found that there were a synergic effect (from sodium, tungsten, and manganese components) and the WO_4 tetrahedron on the catalyst surface appeared. These played an essential role in achieving high CH_4 conversion and high C_2 selectivity in the OCM reaction [90].

In addition, rare earth oxides (REOs) are also the promising catalysts for OCM reaction. Lanthanum, as the most basic one in REOs, showed the high basicity, acidity, catalytic activity and selectivity. It gave a methane conversion of around 11–13%, with a selectivity of 80% toward C2+ [91]. Yamashita *et al.* researched on Ba–La–O mixed oxides as the catalyst for OCM. It was found that this catalyst exhibited a C2 yield of 18% which was higher than 12% from La_2O_3. The highly dispersed O_2^{2-} species on the surface was considered to be responsible for the high catalytic performance [88]. Recently, La-promoted Na-W-Mn/SiO_2 catalyst was studied in micro

reactor by Wu et al. [92]. On 2wt%La-promoted catalyst, the CH_4 conversion was 45.8%, meanwhile the C2+ selectivity was 56% at 800 °C under atmospheric pressure.

The major problems of OCM reaction are the low C2 products yield and hot spot temperature. The C2 products yield in a conventional fixed bed reactor was limited at about 25% [92-95]. This is due to the presence of undesired complete oxidation reactions in the gas phase and partially on the catalyst surface. As found from the OCM kinetics [96-98], the deep oxidation of methane to CO and CO_2 are the main problem. A lower oxygen partial pressure is favourable to achieve the higher C2 selectivity. Therefore, the distribution of oxygen along the reactor length is an important strategy to improve the performance. A membrane reactor was proposed to control the distribution of oxygen to the catalyst bed. This method can avoid the explosion problem from methane combustion because methane does not directly contact with oxygen. Moreover, the heat of reaction released to the catalyst bed can be much more flat throughout the cross-sectional area of the reactor, thereby the hot spot temperature is less severe. In addition, the use of membrane reactor to control the oxygen concentration in a continuous reactor offers a possibility to achieve a much higher C2 selectivity and yield for OCM.

3.2 Catalysts used for the Oxidative Coupling of Methane in Membrane Reactor

The membrane applied to OCM process can closely control the oxygen supply to the methane-coupling reaction and it can avoid the direct presence of gas phase oxygen that is often deleterious to C2 selectivity. The membranes can be classified into two types according to the feature of the transportation of oxygen

though the membrane: oxygen molecule transport in porous pores, oxygen lattice diffusion.

Santamaria and co-workers [62-64] reported an application of porous ceramic membrane tube reactor for OCM. Normally, ceramic materials for porous membranes can be selected from α-alumina, γ-alumina, ZrO_2, TiO_2, CaO, and Vycor glass, from which the α-alumina ceramicis usually preferred due to its stability at high temperature. The membrane reactor gives a considerably better selectivity than a conventional fixed-bed reactor; however, the improvement in C2 yield is usually small. In addition, it is not economical to use pure oxygen. Therefore, when air is used in porous membrane reactor, a subsequent separation of product and nitrogen is needed [99].

To avoid this problem, the dense metal oxide membrane could be of interest, The dense membrane fabricated from a metal or a metal oxide was previously suggested. An example of this membrane is lead oxide supported on magnesia (PbO/MgO) membrane [100], lead oxide supported on Strontia (PbO/SrO), lead oxide supported on porous tube (PbO/SiO_2-AlO_3) (Nozaki and Fujimoto, 1994) and silver membrane [101]. Compared to porous membrane reactors, the dense metal oxide or metal membrane reactors were more successful in terms of attaining high selectivity while keeping the reaction gas free from N_2. However, it provided less reaction rates due to the oxygen transport rate across the membrane was very slow [97]. Another problem is the difficulty in fabricating a pinhole-free PbO film on the porous support material [102]. Therefore, there are few works using this type of membrane for OCM reaction.

According to the reviews mentioned above, dense solid oxide electrolyte membrane could be interest. The common solid electrolytes possessing O^{2-} conduction are stabilized ZrO_2, ThO_2 and CeO_2. The most frequently used is yttria-stabilized zirconia (YSZ, 8%Y_2O_3–ZrO_2) since it shows a much higher conductivity than calcia-stabilized zirconia (CSZ) and magnesia-stabilized zirconia (MSZ) [99]. Its stability at various temperatures and pressures, effective conductivity, good chemical resistance, mechanical strength and relatively low cost make it attractive for many high temperature applications. Lin and co-workers investigated the performance of OCM reaction in the conventional fixed bed reactor and membrane reactor using the dense mixed conducting ceramic (YSZ) membrane packed with Li/MgO catalyst [103]. The kinetic equations over Li/MgO were obtained from their previous work [104]. It was found that this dense mixed conducting ceramic membrane significantly improved C2 selectivity and yield. Moreover, many researcher studied OCM reaction using YSZ membrane with a catalytically active membrane reactor such as Ag-Pd [105], $Bi_{1.5}Y_{0.3}Sm_{0.2}O_{3-\delta}$ (BYS) [104], Au–YSZ [106] and 25 mol%yttia doped bismuth oxide (BY25) [104]. It was found that the best single-pass C2 yield was achieved in BYS doped with Y and Sm membrane reactor.

Among the various inorganic membranes, solid oxide electrolyte membranes have received much more attention due to their great potential in fuel cells, oxygen sensors, and chemical reactions of various kinds [107]. Some attempts were recently reported on electrochemical selective oxidative coupling of methane to C2 hydrocarbon using the reactors which are similar to the solid oxide fuel cells [108].

3.3 Solid Oxide Fuel Cell Reactor for OCM

Solid oxide fuel cell (SOFC) system has been attracting a lot of attentions as a future energy system, SOFC is an electrochemical conversion device that produces electricity directly from oxidizing a fuel with high efficiency. Among these studies, chemical and electrical cogeneration is one of the outstanding topics. Various reaction systems have been tested, Farr and Vayenas (1980) first demonstrated this mode of operation for case of NO production from NH_3 [107]. For cogeneration of C2 hydrocarbons and electricity in SOFC, a solid electrolyte was used as an oxygen separator and an oxygen distributor to achieve higher C2 selectivity in SOFC reactor for OCM reaction.

Table 3.2 contains works in which the solid electrolyte used was a pure oxygen ion (O^{2-}) conductor for oxidative coupling of methane reaction in solid oxide fuel cell reactor. In this electro-catalytic system, combined effects of activation of anode catalyst and permeation of oxygen though the electrolyte control the performance of reactor. The result shown that the C2 yield was low (3-10%).

White et al. suggested that the design of anode for partial oxidation of methane required the development of insight into appropriate electrocatalysis strategy favoring this oxidation path compared with complete oxidation of methane [21]. They have refered to basic knowledge of heterogeneous gas-phase catalytic in designing the anode catalysts and suggested several perovskite oxides as an anode catalyst. This is because perovskite oxide systems with a general formular of ABO_3 (where A and B are usually trivalent rare-earth cations and stability over a broad temperature range as well as high OSC (oxygen storage capacity) and oxygen ion

conductivity [109, 110]. Generally, the B-metal site in perovskite oxide forms the primary active site, while the A metal site has a strong effect on stability.

Selection of the characteristic basicity of rare earth metal oxides [111] and one of the active and selective catalysts for OCM was $Ln_{1-x}Al_xO_3$ perovskite catalyst (Ln=rare earth metal), LaAlO was the best active anode catalyst in their experiments and oxygen species were capable of moving around at the operating temperature of SOFC, W. Kiatkittipong *et al.* studied the OCM in SOFC (LSM/YSZ/LaAlO as cathode, electrolyte and anode) reactor. High selectivity and CH_4 conversion were produced, but further studies were needed to stabilize the catalytic activity [108]. Therefore, the search for new anode catalysts is a way to improve the conversion, selectivity, yield and stability.

Recently some researchers showed the interest in $La_{1-x}Sr_xMnO_3$ (LSM) perovskite-based materials lies in their excellent electrical conductivity, thermochemical properties and most active catalyst for hydrocarbon oxidation, especially MnO3 play important role in the catalytic activity reaction [112]. The promising ability of the perovskite structure is able to suppress carbon formation under hydrocarbon feed conditions and prompted reaction to carry out some catalytic tests on high surface area ultra-fine LSM powders.

Gold-based catalysts is very high activity although gold has been thought for a long time to be chemically inert, it has been found that its catalytic performance is significantly affected by the size of the Au particle [113-115]. When gold nanoparticle is deposited on select metal oxides [113] (e.g. MnOx, TiOx, **α**-Fe_2O_3, and Co_3O_4) as ultra-fine particles, promising found that its chemistry dramatically changes because

addition of metal oxides stabilizes the average gold particle size, close contact between gold and metal oxides is expected [116]. The enhancement of catalytic activity of supported gold catalysts has been reported to depend on dispersion, supports and preparation method. Several studies demonstrate that activity and stability of the gold catalysts increased if it is supported on, or promoted by, transition-metal oxides [117].

Moreover highly dispersed gold nanoparticles on appropriate metal oxides such as Au/MnO_x , Au/Fe_2O_3, Au/CeO_2, Au/Al_2O_3, Au/CuO/ZnO, Au/LSM, Au/ $LaSrCrO_3$ are really active in many important chemical reactions, i.e. in methane oxidation, propane partial oxidation, autothermal reforming and steam reforming, CO oxidation, and exhibit high selectively with small amount of catalysts. Moreover, Au/ $LaSrMnO_3$, Au/$LaSrCrO_3$ perovskite composites catalysts have been previously investigated as remarkable anodic catalysts in SOFCs for propane reforming processes [24]. Au/LSM show high activity for propane reforming than Au/$LaSrCrO_3$.

Ceria, an excellent electronic and ionic conductor, it can realize the direct utilization of hydrocarbon, CeO_2 has been showed to increase conversion of methane without coking [118-120]. It is known to be a proper oxygen activator with high oxygen storage capacity. G. Cai *et al.* studied Mn-doped CeO_2 -Scandia-stabilized zirconia composites (MDC–ScSZ) are evaluated for using anode materials in SOFC in terms of chemical compatibility, thermal expansion coefficient, electrical conductivity, and fuel cell performance in H_2 and CH_4. They found that the Mn doping into CeO2 can reduce the ohmic and polarization resistance, thus leading to a higher performance. The results demonstrate the potential ability of MDC–ScSZ composite to be used as SOFCs anode [121].

In partial oxidation of CH_4 many catalysts have been advanced in literature. Besides the oxide supported (MgO, SiO_2, Al_2O_3, CeO_2, ...) Fe, Co, Ni, Cu metals and noble metals (Ru, Rh, Pt) or metal oxides with or without additives like CeO_2, oxide-based formulations were also studied [87, 118]. Other perovskites, pyrochlores, brownmillerites oxides were advanced as catalysts for CH_4 activation, many of them being quite stable in the reaction conditions. Such examples are $LnMO_3$ with M = Al, Ti, V, Cr, Mn, Fe, Co, Ni, Cu, Y and Nb, substituted or not on the A or B sites, TiO_2, ZnO, Nb_2O_5, Bi_2O_3, CeO_2, lanthanide-based oxides. Among the lanthanide perovskites, $LnMO_3$, of the first row transition metal elements, Mn, Fe, Co and Ni, based compounds were found to exhibit interesting oxidative behaviour under co-feed (CH_4+O_2) reaction conditions comparable to highly active Pt/Al_2O_3 . $LnCrO_3$ were the least active [91]. By substituting Sr on the La site, an increase in activity was observed and related to a higher lattice oxygen availability [53, 97]. The lanthanide part did also influence the catalytic activity towards CH_4 but less than the accompanying transition metals. For the same transition metal element, the reducibility and thus the lattice oxygen availability tended to decrease in the trend Gd>Sm>Nd>Pr>La, corresponding to a decrease in catalytic activity. The perovskite $(La_{0.75}Sr_{0.25})(Cr_{0.5}Mn_{0.5})O_3$–$\delta$ (called LSCM) was largely explored as potential anode for SOCs, Solid Oxide Fuel Cells (SOFCs) or Solid Oxide Electrolysis Cells (SOECs). However, as in the case of the majority of ceramic anodes, which are essentially MIEC compounds, the electro-catalytic properties of LSCM towards direct oxidation of fuel have to be improved for device application.

3.4 Oxygen permeation though solid oxide electrolyte

Many research groups have published their experimental results on the overall oxygen permeation though many permeable electrolyte membranes such as YSZ [122, 123], mixed ion-electronic conducting materials such as $La_{0.2}Sr_{0.8}CoO_{3-\delta}$ (LSC) [122], $La_{1-x}Sr_xCo_{1-y}Fe_yO_{3-\delta}$ (LSCF) [122, 123] and other perovskite type ceramics such as $Ba_{0.5}Sr_{0.5}Co_{0.8}Fe_{0.2}O_{3-\delta}$ [124], $GdBaCo_2O_{5+\delta}$ [125, 126], $BaCo_xFe_yZr_zO_{3-\delta}$ [127] and $BaBi_xCo_{0.2}Fe_{0.8-x}O_{3-\delta}$ [128].

The conventional Yttia Stabilized Zirconia (YSZ) electrolyte used to provide the electrochemical permeation of oxygen for OCM. Several studied focused on the steady state oxygen permeation in membrane reactors for oxidation reactions such as partial oxidation of methane and oxidative coupling of methane. However, very limited studies on oxygen permeation in SOFC reactors have been reported. W. Kiatkittipong *et al.* studied oxygen transport in a LSM/YSZ/LaAlO solid oxide fuel cell type reactor, the oxygen permeation flux increased by applying an external potential [108]. They suggested that the oxygen permeation at the anode side was the rate-limiting step for the oxygen permeation.

Table 3. 1 shows a brief summary of different catalysts for oxidative coupling of methane using in fixed bed reactor.

Catalysts		**T (°C)**	**Maximum C2 Yields**	**Years**	**References**
Catalysts without support	La_2O_3	750	12.6	1992	106
	BaX_2/Gd_2O_3 (X=F, Cl, Br)	750	21.1	1998	107
	CeO_2	800	1.6	2003	7
	La_2O_3	800	13.9		
	Eu_2O_3	795	14.0		
	Li doped Y_2O_3	750	15.7	2001	5
	$ZnNd_2O_4$	800	20	2009	13
	5%Ni doped Sm_2O_3	750	18.3	2000	2
	$LaAlO_3$	750	9.4	2001	4
	$LaAl_{0.9}Li_{0.1}O_3$	750	11.1		
	$SrNi_{0.7}Li_{0.75}O_{3-x}$	750	22.4	2005	9
	Na doped $BaSrTiO_3$	800	24	2008	12
	Fe doped La_2O_3	750	5	2009	14

Catalysts		T (°C)	Maximum C2 Yields	Years	References
Catalysts without support	La_2O_3	750	12.6	1992	129
	BaX_2/Gd_2O_3 (X=F, Cl, Br)	750	21.1	1998	130
	CeO_2	800	1.6	2003	7
	La_2O_3	800	13.9		
	Eu_2O_3	795	14.0		
	Li doped Y_2O_3	750	15.7	2001	5
	$ZnNd_2O_4$	800	20	2009	13
	5%Ni doped Sm_2O_3	750	18.3	2000	2
	$LaAlO_3$	750	9.4	2001	4
	$LaAl_{0.9}Li_{0.1}O_3$	750	11.1		
	$SrNi_{0.7}Li_{0.75}O_{3-x}$	750	22.4	2005	9
	Na doped $BaSrTiO_3$	800	24	2008	12
	Fe doped La_2O_3	750	5	2009	14

Table 3. 2 shows a brief summary of different catalysts for oxidative coupling of methane using in solid oxide fuel cell reactor.

Electrolyte	**Working electrode (Catalyst)**	**T (°C)**	**Maximum C2 Yields**	**Years**	**Ref.**
YSZ tube	Ag	700	0.6	1985	1
YSZ tube	Bi_2O_3-Ag	700	2.1	1985	2
YSZ plate	LiCl-NiO	700	0.6	1988	3
YSZ plate	$LiNiO_2$	700	0.3	1988	4
YSZ	Ag, Bi_2O_3-Ag , Cu, Fe	750-900	3.0	1988	18
YSZ	Pt/Sm_2O_3/$La_{0.83}Sr_{0.1}MnO_3$	760	0.2	1988	19
YSZ	Bi_2O_3-Pr_6O_{11}	700	1.6	1988	20
YSZ	Li/MgO-Ag, Bi_2O_3-Ag, Cu,Pt, Mo-Ag, Sm_2O_3-Ag	700-900	3.1	1988 1989	21 22
YSZ tube	Ag	795	1.0	1990	5
YSZ tube	Ag-Pd	840	9.0	1990	6
YSZ tube	Ag-$LaCoO_3$	735	0.4	1990	7
YSZ	KF/Au, $BaCO_3$/Au, NaCl	800	1.6	1990	26
YSZ	Ag, 80%Ag/20% Pd, Cu, Ni, Pt, $LaCrO_3$	700-840	10.0	1990	23

Electrolyte	Working electrode (Catalyst)	T (°C)	Maximum C2 Yields	Years	Ref.
YSZ tube	Au-YSZ	900	7.9	1991	8
YSZ tube	Sr/La_2O_3-Bi_2O_3	730	7.5	1997	9
YSZ tube	Sr/La_2O_3-Ag	730	6.9	1997	10
YSZ tube	Ag	730	0.9	1997	11
YSZ tube	Sr/La_2O_3-Ag	730	8.1	1997	12
YSZ	MnOx	750-830	1.0	1997	36
YSZ tube	Ag	850	3.0	1990	13
YSZ	Au-$SrCeO_3$	700-850	3.1	1994	33
$La_{0.6}Sr_{0.4}Co_{0.8}Fe_{0.2}O_3$ disk	-	950	3.1	1995	19
YSZ tube	Ag	730	1.4	1997	14
YSZ tube	Sr/La_2O_3-Ag	730	2.0	1997	15
YSZ plate	$La_{1.8}Al_{0.2}O_3$	700	3.8	1998	22
YSZ tube	Sr/La_2O_3-Bi_2O_3	730	2.0	1999	16
YSZ tube	LaSrMnO/LaAlO	1000	4.0	1999	17
YSZ plate	Ni/ZrO2	950	9.5	2003	23
YSZ tube	$Mn/Na_2WO_4/SiO_2$-Ag $Mn/K_2WO_4/SiO_2$ -Ag	500-1000	4.0 4.0	2003	24
YSZ tube	$La_{1.8}Al_{0.2}O_3$	700-1000	4.3	2005	25

CHAPTER III
EXPERIMENTAL

4.1 $Au/La_{0.6}Sr_{0.4}MnO_3$ powder preparation

The perovskite oxide, $La_{0.6}Sr_{0.4}MnO_3$ (LSM), was prepared by sol-gel method. In this process, stoichiometric quantities of $La(NO_3)_3.6H_2O$ (Aldrich, 99.99%), $Mn(NO_3)_2.6H_2O$ (Aldrich, 98%) and $Sr(NO_3)_2$ (Aldrich, 99.99%) precursors were dissolved into water. Hence, an aqueous solution of citric acid (Riedel de Haën, reagent grade) and ethylene glycol (Aldrich, 98%) was added to the metal solution (citric acid: metal nitrates[acetate]: ethylene glycol molar ratios=5:1:4.3). The mixture was stirred at 70 °C for 12 h. Water was slowly evaporated on a hot plate and the resulting brown gel was dried and then heated up in air at 400 °C for 2 h in an oven. LSM perovskite samples were obtained by ball-milling the decomposed resin for a few hours before calcination at 1000 °C for 2 h in air with heating rate 6 °C/min). Au/LSM nanocomposites were prepared by dissolving 1, 3 and 5 wt.% of hydrate $HAuCl_4$ in deionised water, followed by the addition of an ammonia solution until a final pH of 7 was reached. Then, Au precursor was added to stirred LSM, which was then sonicated in an ultrasonic bath for 6 h; next, it was centrifuged, washed with deionised water, dried and heated at 300 $^{\circ}C$ for 4 h in air. Phase identification of this powder was performed by X-ray diffractometry (XRD).

4.2 Catalytic activity test of catalysts in conventional fixed bed reactor

The catalytic of methane oxidation reaction over all catalysts were performed at atmospheric pressure and at temperatures of 700–1000 $^{\circ}C$ in a quartz micro-

reactor (i.d. 6 mm) placed in a ceramic tube furnace as shown in figure 4.1. A total of 0.3 g of fresh catalyst was loaded into a reactor that was located in a programmable furnace with a thermocouple placed in the centre of the catalyst bed, and 2:1, 4:1 and 6:1 CH_4:O_2 molar ratios of the feed were used. The gas products were sampled every 30 min for measuring their compositions using an on-line gas chromatography equipped with a TCD detector. Herein, $La_{0.25}Sr_{0.75}Cr_{0.5}Mn_{0.5}O_3$ (LSCM) and $LiFeO_2$ (LFO) particles were supported from JTSI group School of Chemistry, University of St Andrews, St Andrews, UK.

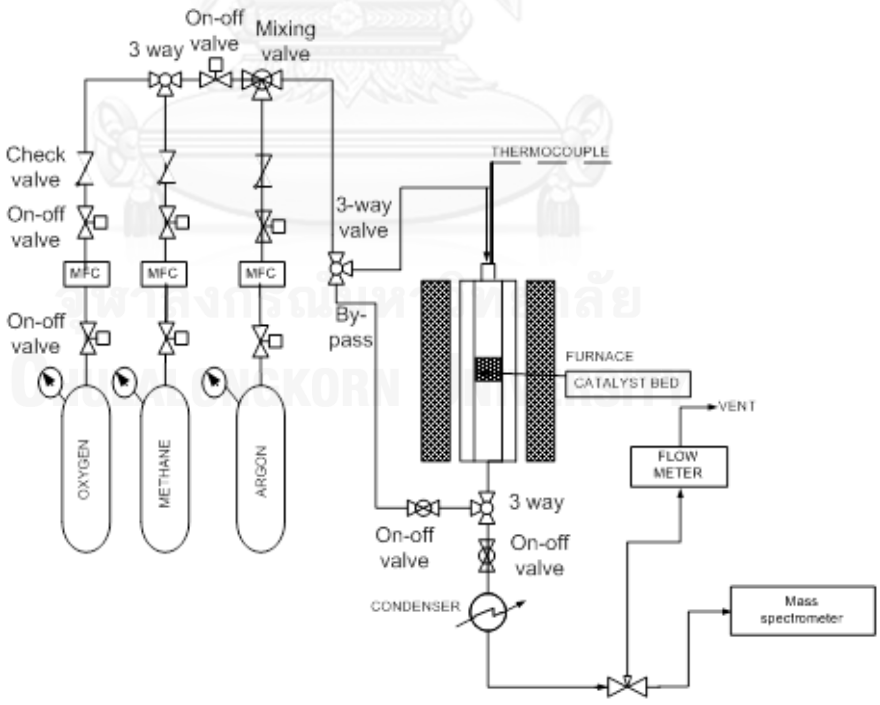

Figure 4. 1 Schematic diagram of the conventional fixed bed reactor.

4.3 Single cell preparation

4.3.1 Tape casting process

The procedure for preparing tape casting slurries was based on a process that had been developed by the group of Prof Irvine and coworkers [3]. A formulation of green tapes was shown in table 4.1. The slurry was prepared by dissolving a dispersant (Triton QS-44, Sigma-Aldrich Ltd) with the solvent mixture of methyl ethyl ketone (MEK) and ethanol (60/40 % by weight) in a 125 cm^3 Nalgene bottle (Sigma Ltd) before adding the YSZ powder and grinding media (18x zirconia balls each of 8.8 mm diameter). The mixture was then milled for 18 h on a home-made ball mill with a speed of 160 rpm. This step allowed some soft agglomerates to be broken down and the powder particles to be mixed and dispersed homogeneously throughout the solvent. In the next step, PEG (Mn = 285-315, Sigma-Aldrich) and DBP (Fisher scientific) plasticizers and PVB (Butvar® B-98, Mw = 40,000-70,000, Sigma-Aldrich) binder were added to the dispersed mixture. Then, the bottle was then vigorously shaken on a vibratory mixer for 20 min to deagglomerate binder lumps and to help dissolve the binder into the mixture. Most of the binder was dissolved at this stage but the mixing process was still continued on the ball mill for another 4 h using 100 rpm speed. In the last step, the slurry was then rotated slowly on the ball mill for at least 18 h at a speed of 26 rpm for de-aeration.

The slurry for porous YSZ cast tape was prepared by the same procedure as mentioned above except that a certain amount of YSZ powder was replaced by pore formers. The pore formers used in this experiment were graphite (325 mesh, Alfa Aesar) and glassycarbon (10-20 μm, Alfa Aesar). A TTC-1000 (Richard E Mistler Inc) tape caster was used for casting. The design of this tape caster is shown in Figure 2.6.

The slurry was poured into a single 4 inch doctor blade reservoir which was set on a carrier film (silicon-coated Mylar). The gap height between the blade and the carrier film was kept at 0.012 cm for electrolyte tapes and at 0.035 cm for porous tapes. The slurry was cast by moving the carrier film at approximately 42 $cm.s^{-1}$. This process, the electrolyte slurry was cast and the cast tapes were left to dry in air at room temperature for 60 min. Then, the second layer of porous tapes was co-cast on YSZ green tapes.

Table 4.1 Formulations of green tapes

Compositions		Formulations (g)	
		Electrolyte	Porous layer
YSZ powder		20.000	20.000
Pore formers	Graphite	-	3.225
	Glassy carbon	-	1.075
Triton QS-44		0.130	0.300
PEG		1.720	3.300
DBP		1.560	2.880
Butar (PVB)		2.240	4.420
Solvent		10.000	20.000

4.3.2 Lamination of ceramic green tape

In the first step, the co-casing electrolyte-porous tapes were punched into circular discs using steel punches (diameter= 25 mm) and the porous tapes were punched into smaller circular discs using steel punches (diameter =15 mm). The smaller circular discs of porous YSZ tape was then attached on one sides of the electrolyte disc. A schematic of a finished disc is shown in figure 4.2. The tapes were then laminated using additional heat of 40 $^{\circ}$C generated using a household iron. The laminated tape was held at temperature for around 10 sec without additional pressure except the weight of the iron. Finally, the laminated tapes were sintered at 1350 $^{\circ}$C for 5 hr with sintering treatments as shown in figure 4.3. The porous layer with the same diameter of the electrolyte acts as a support for the electrolyte while the smaller one prevents cross-contaminations between the two electrode materials during the impregnation process.

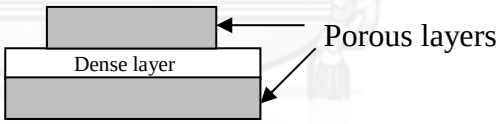

Figure 4.2 Geometric pattern of a three-layer green tape stack.

4.3.3 Preparation of electrode

4.3.3.1 Preparation of LSM//YSZ//Au/LSM single cell

A plate-type YSZ (8 mol.% Y_2O_3, thickness = 0.3 m, diameter = 25 mm, fuel cell material, FCM) was used as an electrolyte. Normally, a perovskite type $La_{0.25}Sr_{0.75}MnO_3$ ($LaSrMnO_3$) was used as a cathode material. The characteristic of $LaSrMnO_3$ powder was described elsewhere [19]. $LaSrMnO_3$ perovskite samples were ground to fine powder. The $LaSrMnO_3$ powder was mixed with glycerol and pasted

on one side of YSZ plate by hand-painting. The electrode was painted in full-circle pattern at the centre on both sides of the pellet creating a cell with two-electrode configuration as displayed in figure 4.4. The superficial surface area of each electrode was 0.785 cm^2. After painting, the electrode was fired at 1000 $^{\circ}C$, for $LaSrMnO_3$ electrodes, and at 800 $^{\circ}C$, for Au/LSM electrodes, in air for 1 h in order to attain good adhesion with the electrolyte.

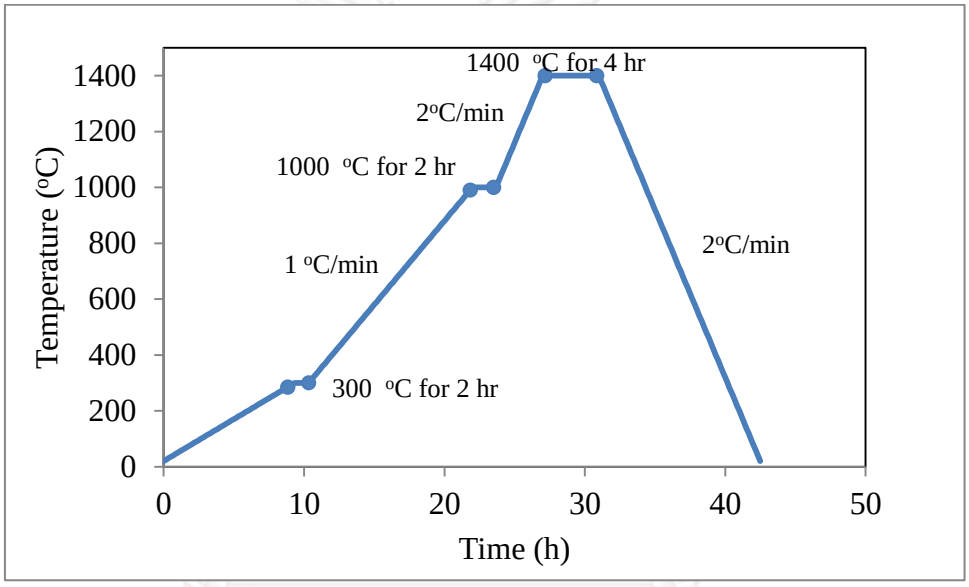

Figure 4.3 Sintering treatments for laminated tapes.

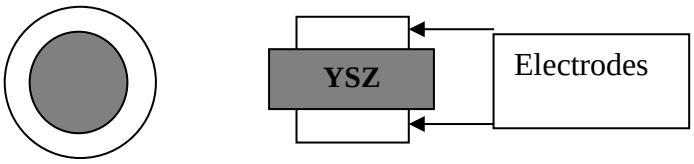

Figure 4.4 Geometry of electrode on YSZ pellet for electrochemical testing.

4.3.3.2 Preparation of LSF//YSZ//LSCM and LSF//YSZ//Ce-LSCM single cell

After synthesizing the three-layer YSZ, LSCM was added to anode porous layers using aqueous nitrate solutions until the loading of LSCM was 40 wt.% as described figure 4.5. The metal nitrate solution was introduced drop-wise onto the porous YSZ layer using a 1 ml syringe fitted with a needle. The impregnated sample was dried in an oven at 300 $^{\circ}$C for 30 minutes and the process was repeated until the porous substrate reached a saturated point. Then, the sample was transferred to the furnace where the nitrate decomposition was performed in a stagnant air. The heating treatment consisted of a fast heating rate of 8 $^{\circ}$C/min to 800 $^{\circ}$C and dwelling at this temperature for 60 min before cooling down to room temperature at a rate 3 $^{\circ}$C/min. The technique of fast drying provides uniform distribution of the metal particles. Slow drying tends to cause the migration of the metal salt upward and accumulate near porous layer surface [3]. After the heating treatment, the perovskite of the electrode material should deposit on the YSZ porous scaffold surface. The desired loading of the electrode oxide was achieved after repeating the process about 10-15 times in porous support. Finally, it was heated in air to 1200 $^{\circ}$C for 4 hr. For cathode side, $La_{0.8}Sr_{0.2}FeO_3$ (LSF) cathode was added after the final 1200 $^{\circ}$C calcinations used to produce the LSCM, and was calcined at 850 $^{\circ}$C. Additions of CeO_2 at the anode were impregnated in separate stages. In this case, the drying temperature was 400 $^{\circ}$C, and they were calcined at 700 $^{\circ}$C. Phase composition and metal oxide distribution inside the porous substrate were investigated by SEM-EDS.

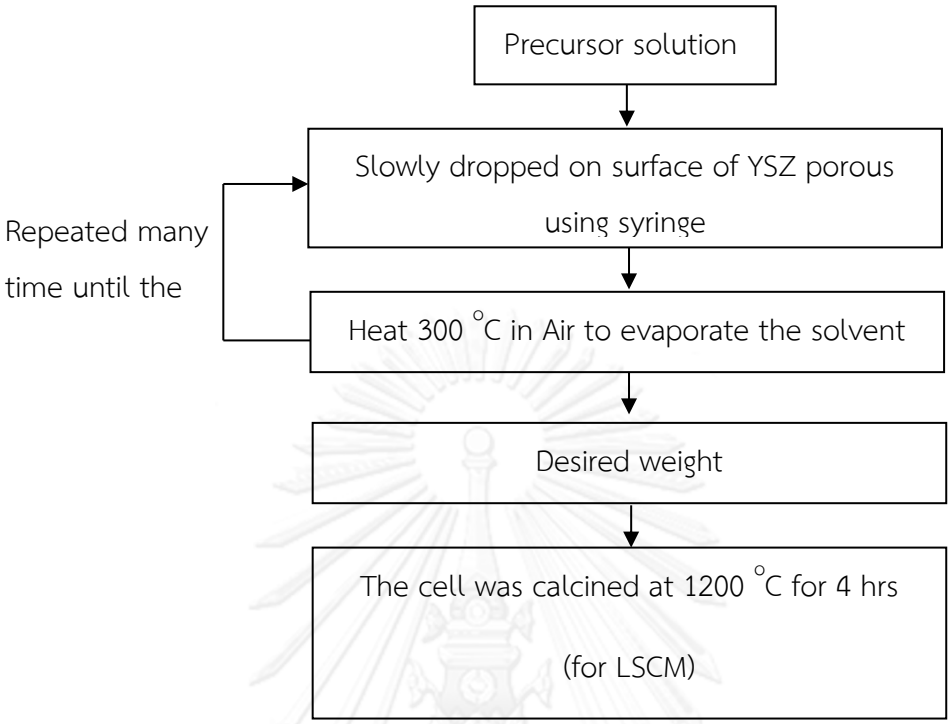

Figure 4.5 Schematic of the infiltration process.

4.3.3.3 Preparation of LSF//YSZ//LFO and LSC//LSGM//LFO single cell

The single cell was prepare in YSZ electrolyte and porous similar in section 4.3.3.2. However, $LiFeO_2$ (LFO) anode was added after the final 850 °C calcinations used to produce the LSF, and was calcined at 700 °C. In addition the difference electrolyte material was studied. The LSGM 3-layer cells were supported from JTSI group School of Chemistry, University of St Andrews, St Andrews, UK. $La_{0.6}Sr_{0.4}CoO_{3-\delta}$ (LSC) was added to cathode porous layers using aqueous nitrate solutions until the loading of LSC was 40wt.%. The metal nitrate solution was introduced drop-wise onto the porous LSGM layer using a 1 ml syringe fitted with a needle. The impregnated sample was dried in an oven at 400 °C for 20 minutes and the process was repeated until the porous substrate reached a saturated point. Then, the sample

was transferred to the furnace where the nitrate decomposition was performed in a stagnant air. The heating treatment consisted of heating rate of 3 °C/min to 800°C and dwelling at this temperature for 60 min before cooling down to room temperature at a rate 3 °C/min. After the heating treatment, the perovskite of the electrode material should deposit on the LSGM porous scaffold surface. The desired loading of the electrode oxide was achieved after repeating the process about 10-15 times in porous support. Finally, it was heated in air to 950 °C for 2 h. For anode side, LFO anode was added after the final 950 °C calcinations used to produce the LSC, and was calcined at 700 °C. Phase composition and metal oxide distribution inside the porous substrate were investigated by SEM-EDS.

4.4 Electrochemical Measurements

4.4.1 Test jig

Electrochemical measurements of SOFC cells were carried out in a two-chamber apparatus. The measurements were performed in the temperature range 750-850 °C. The sample was fixed between two alumina tubes by pyrex ring or alumina sealant (Aremco, Ceramabond 552) creating two gas-tight compartments as shown in figure 4.6 and 4.7, respectively. For LSM//YSZ//Au/LSM button cell system, a SOFC schematic diagram was shown in figure 4.6. It was separated by using two ceramic tubes (O.D. = 25 mm, I.D. = 19 mm), between which the cell system LSM//YSZ//Au/LSM was placed and sealed using a pyrex ring. The effective area of the anode was 1.9 cm^2. A platinum wire of 0.05 mm diameter (Alfa Aesar) was connected to platinum meshes (100 mesh, Alfa Aesar) placed on both electrodes to serve as current collectors. Then the temperature was raised with a heating rate of 1 °C/min to 750-850 °C.

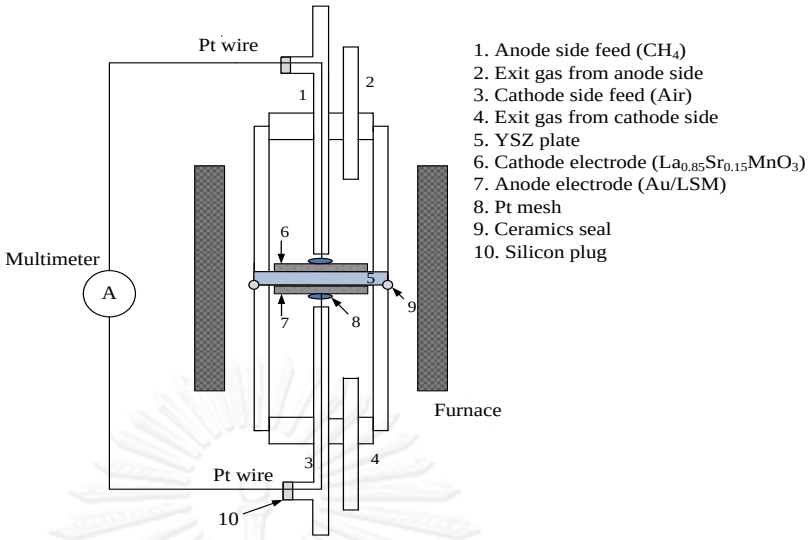

Figure 4.6 Schematic diagram of the solid oxide fuel cell using pyrex ring sealant.

The impregnated cell (LSF//YSZ//LSCM, LSF//YSZ//Ce-LSCM, LSF//YSZ//LFO and LSC//LSGM//LFO) was fixed between two alumina tubes by pyrex ring or alumina sealant (Aremco, Ceramabond 552) creating two gas-tight compartments. The outlet tube with 0.25 mm diameter was placed centrally inside the 20 mm diameter tube. Both 20 mm and 0.25 mm diameter tubes were fitted with a Swagelok stainless steel T-shape fitting. Electrical connections were achieved by connecting the electrodes of the cell to the stainless steel fitting from inside the alumina tube using Ag paste and Ag wires. The schematic of the two chamber setup is shown in Figure 4.7. Inside the furnace, the cell was dwelled at 150 ℃ for 1-2 h in order to cure the ceramic sealant. Then the temperature was raised with a heating rate of 1 ℃/min to 750-850 ℃.

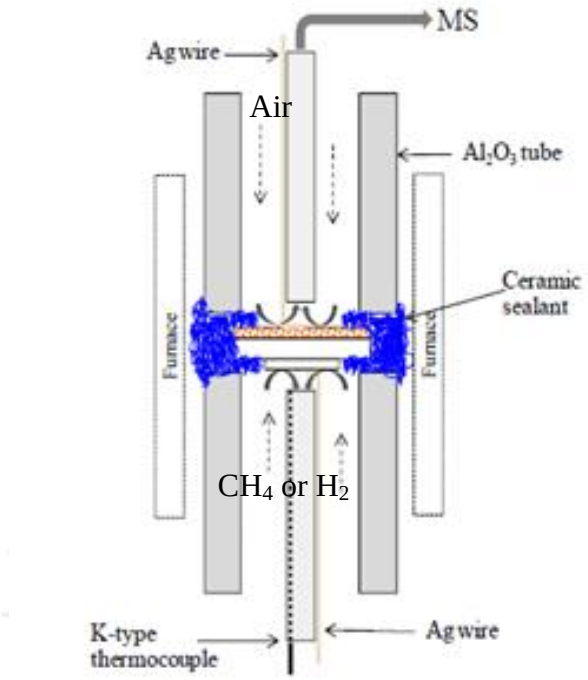

Figure 4.7 Two-chamber testing apparatus using alumina sealant.

4.4.2 Performance of SOFC cell

In this study, only humidified H_2 and CH_4 was used as the anode gas. Humidified H2 and CH4 was achieved by bubbling gas through room-temperature water resulting in a gas mixture of 3 % H2O and fuel. The flow rate of gas was controlled by a needle flow meter.

The open circuit voltage (OCV) of the cell under testing condition was recorded as a function of time until the system reached the steady state before performing the electrochemical measurements. The electrochemical measurements were carried out using a frequency response analyzer (Solartron 1255, UK) coupled with an electrochemical interface (Solartron 1287, UK). The voltage-current (V-I) measurement was performed by sweeping potentials across the cell using a scan

rate of 2 mV/sec with the applied potentials from 0-0.5 V with respect to the OCV. The AC impedance measurement was obtained in a frequency range of 1 MHz to 0.1 Hz using a potential amplitude of 50 mV under open-circuit conditions. In some cases, the polarisation under applied potential was also investigated.

For C2 hydrocarbon synthesis, humidified CH4 was fed into the anode, during electrolysis, the gaseous products in the anode outlet stream were examined by a mass spectrometer (MS) (Prolab, Thermo Scientific) and GC-8A gas chromatograph (Shimadzu) equipped with a TCD, using a Poropak Q and Molecular Sieve 5A column at every 15 min. In order to determine the compositon of gases, a constant flow rate of CH4 was required. In this work, a mass flow controller (Model 5850S, Brooks instrument) was employed. However, the actual flow rate of the outlet stream was checked periodically by a glass soap bubble flow meter.

4.5 Characterization techniques

All synthesised catalysts and SOFC cell were characterized by several techniques such as:

4.5.1 X-ray Diffraction (XRD)

The bulk crystal structure and chemical phase composition were determined by diffraction of an X-ray beam as a function of the long fine focus. The XRD spectrum were measured by using a D8 Advance Bruker AXS X-ray diffractometer and CuK_{α} radiation with Ni filter in the 2θ range of 10-80 degrees with resolution 0.02. The crystallite size was calculated from Scherrer's equation.

4.5.2 N_2 Physisorption

The BET surface area, pore volume, and average pore size diameter of catalysts was measured through nitrogen gas adsorption at liquid nitrogen temperature (-196°C) using Micromeritics ASAP 2020 instrument.

4.5.3 Scanning Electron Microscope (SEM)

Scanning electron microscope (SEM, model JEM-6400 Jeol Ltd., Japan) and transmission electron microscopy (TEM, model JEM- 2100 Jeol Ltd., Japan) were used to study the morphology. The SEM was operated in the back scattering electron (BSE) mode at 15 kV.

4.5.4 Transmission Electron Microscopy (TEM)

The morphologies of LSM supports and 1%Au/LSM catalysts were investigated using JEOL-JEM 2010 transmission electron microscope using energy-dispersive X-ray detector operated at 80-200 kV. The average Au particle sizes and distribution of Au on the LSM supports were also observed.

CHAPTER V
RESULTS AND DISCUSSIONS

The results and discussions in this chapter are divided into three parts. In the first part the characteristics and properties of LSM and Au/LSM were investigated by several techniques such as BET, XRD, SEM and TEM analysis. The performance of Au/LSM anode catalysts was investigated in fixed bed reactor (FBR) and solid oxide reactor (SOFC). The second part, the three layer YSZ cell was prepared by tape-casing process. The LSCM and Ce/LSCM anode catalysts were prepared by infiltration method. After that, the catalytic activity and electrochemical performance were tested in FBR and SOFC, respectively. The third part, the catalytic activity of $LiFeO_2$ anode catalyst was investigated in FBR reactor. In SOFC system, LSGM electrolyte was used to compare with YSZ electrolyte.

Part I
Synthesis, characterization and electrical properties of LaSrMnO3-based powder

5.1 Au/LSM anode catalyst

5.1.1 Material Characterization

The results from the material characterization are shown in Table 5.1. The BET surface area for the LSM was 3.45 m^2 g^{-1}, the pore volume was 0.009 cm^3 g^{-1}, and the pore size was 7.2 nm (Table 1); these results coincide with Gaudon et al. [129]. After the LSM was loaded with Au precursor, the surface areas and pore sizes of the LSM and Au/LSM decreased because of the sintering during the drying and calcination processes.

The X-ray diffraction patterns at room temperature of LSM was identified to be perovskite type crystalline structure (Fig. 5.1 (a)) [24, 130]. The crystal size of $La_{0.6}Sr_{0.4}MnO_3$ estimated by the well-known Scherrer equation was around 60–100 nm. The XRD pattern of Au/LSM nanocomposites (Fig. 4.4(b)) revealed the additional reflection peaks at 2θ = 38.098, 44.258 and 64.378 [24, 114]. It should be noted that there are no differences in the XRD patterns between the presence of metallic Au nanoparticles and LSM.

Table 5.1 Surface areas, average pore size and pore volume.

Catalyst	surface area ($m^2 g^{-1}$)	Total pore volume ($cm^3 g^{-1}$)	Mean pore diameter (nm)
LSM	6.84	0.009	7.2
1%Au/LSM	5.34	0.007	5.9
3%Au/LSM	4.47	0.007	5.2
5%Au/LSM	3.40	0.004	4.1
3%Au/LSM*	4.20	0.005	4.8

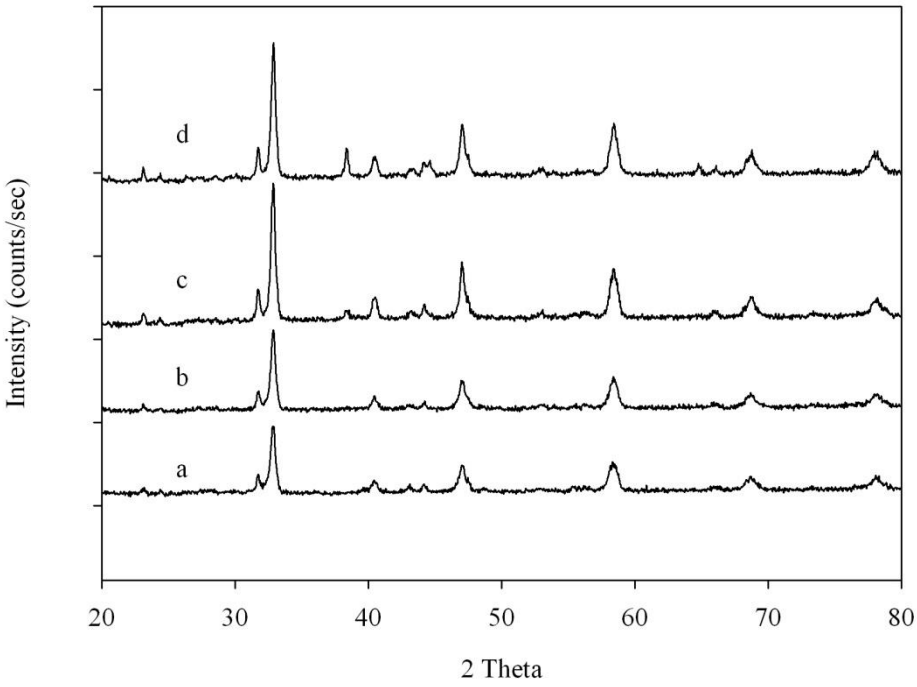

Figure 5.1 XRD patterns of (a) LSM, (b) 1 wt.% Au/LSM, (c) 3 wt.% Au/LSM, and (d) 5 wt.% Au/LSM.

The TEM images of LSM and the 1,3,5 wt% Au/LSM nanocomposites. Figure 5.2 shows TEM images of LSM and the 1, 3, 5 wt.% Au/LSM nanocomposites. The TEM micrographs of LSM show the presence of compact nanocrystalline agglomerates. The estimated particle diameters for LSM and Au were 100–400 nm and 10–30 nm, respectively. The Au morphology was mostly found in hemispherical shape [116]. A less homogenous dispersion of metallic Au nanoparticles having dimensions from <5 nm up to 20–25 nm on LSM surface was obtained when 3 and 5 wt.% of Au were added to the LSM suspension.

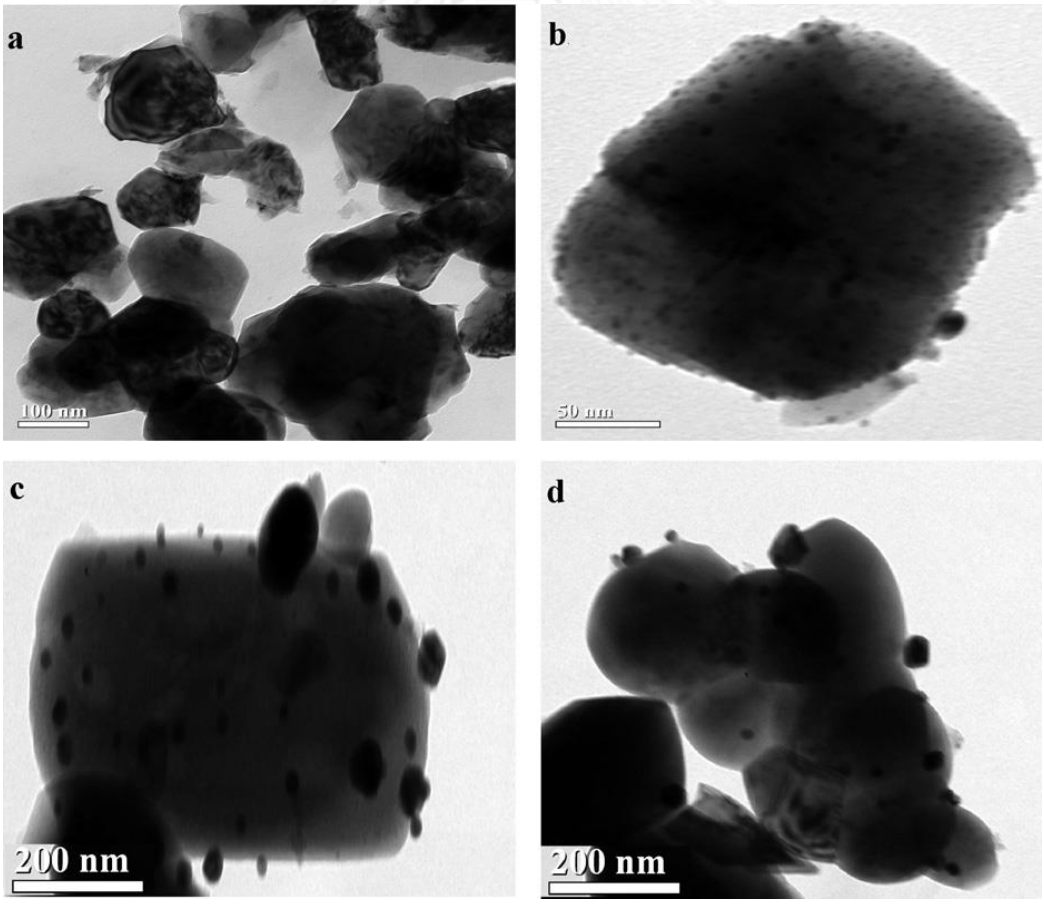

Figure 5. 2 TEM images of (a) LSM , (b) 1%Au/LSM, 3%Au/LSM and 5%Au/LSM.

5.1.2 Catalytic performance of catalysts in fixed bed reactor

As for the conversion of methane, typically, OCM has been studied mostly in conventional reactors such as fixed bed reactor. One of attractiveness for selecting methane is its utility for various applications, its wide availability. Table 5.2 summarises the catalytic performances of LSM and Au/LSM at 7860 h^{-1} of GHSV and at 800^{o}C for a molar ratio of CH_4/O_2 = 6:1. For Au/LSM, the presence of Au can improve the catalytic performance of LSM. The conversion of CH_4 was slightly increased, from 10.6 to 12.9% (1 wt.%, 3 wt.% and 5 wt.% Au). The selectivity of C2 was slightly improved with the increasing Au concentration, from 16.0% at 1 wt.%, to 17.8% at 3 wt.%. However, C_2 selectivity of the 5 wt.% Au addition to LSM powders was obviously decreased when compared with the 1 wt.%, 3 wt.% Au because Au nano-particles have agglomerated and the catalytic performance is significantly affected by the size of the Au particle. These results are in agreement with the data obtained from TEM micrographs at 5 wt.% Au/LSM.

Table 5. 2 Catalytic performance of LSM and Au/LSM at different Au loading (CH_4:O_2=6:1, 800 ^{o}C and GHSV= 7860 h^{-1})

Catalyst	Conversion (%)	Selectivity (%)			Yield (%)
	CH_4	C_2	CO	CO_2	C2
LSM	6.8	14.8	20.2	64.4	1.0
1%Au/LSM	10.6	16.0	24.3	53.0	1.7
3%Au/LSM	10.8	17.9	17.2	59.6	1.9
5%Au/LSM	12.9	11.3	23.8	53.5	1.5

In addition, the trend of C2 yield was imperceptible from 1.0% to 1.9% at GHSV of 7860 h^{-1} and 800 ^{o}C, which is similar to the CH_4 conversion. A comparison between LSM and Au/LSM catalysts obviously indicates that when Au/LSM is utilised in the OCM reaction, the % conversion, % selectivity of C2 hydrocarbons and % C2 yield are greater than those of LSM. However, CH_4 conversion, C2 selectivity and C2 yield was low so its activity was tested in a fixed bed reactor at two different ratios of CH_4/O_2 and 1%wt Au/LSM was selected for testing. The catalytic performances of LSM and Au/LSM at different values of GHSV and temperature for a molar ratio of CH_4/O_2 = 2:1 was shown in Table 5.3. The results show that both catalysts were more selective to partial oxidation than the complete combustion, as the selectivity to CO was much higher than that to CO_2. Approximately 79.6% CO selectivity and 13.3% CO_2 selectivity at 54.7% CH_4 conversion with Au/LSM was successfully obtained at 900 ^{o}C, GHSV 7860 h^{-1}. The selectivity to C2 hydrocarbons was quite low, but its value increased with increasing GHSV, indicating that C2 hydrocarbons can be further reacted to other products like CO or CO_2. For the LSM catalyst, the deep oxidation of CH_4 may be suppressed by increasing the GHSV; however, the methane conversion becomes smaller due to the shorter contact time. Increasing the temperature is another choice to decrease the CO_2 selectivity while improving the methane conversion. For Au/LSM, the presence of Au can clearly improve the catalytic performance of LSM. The conversion of CH_4 was progressively increased, from 27.9% to 40.3%, and the trend of H_2 yield was quite similar to the CH4 conversion, from 20.5% to 30.6% at GHSV 7860 h^{-1}, 1000 ^{o}C.

Table 5. 3 Effect of methane GHSV on the catalytic activity of LSM and Au/LSM (CH_4:O_2=2:1)

Catalyst	GHSV (h^{-1})	Conversion (%)	Selectivity (%)			Yield (%)
		CH_4	C_2	CO	CO_2	H_2
LSM	5240[a]	40.8	1.1	72.8	25.6	32.0
	7860[a]	37.3	1.3	78.9	19.3	29.9
	10480[a]	32.3	5.6	75.7	18.2	26.6
	7860[b]	27.9	1.9	65.6	31.9	20.5
Au/LSM	5240[a]	56.8	1.2	76.3	22.4	45.1
	7860[a]	54.7	6.5	79.6	13.3	43.9
	10480[a]	35.3	8.1	74.6	17.1	26.2
	7860[b]	40.3	1.4	72.4	25.9	30.6

[a]Reactor temperature = 1,000°C

[b]Reactor temperature = 900°C

Table 5. 4 Catalytic performance of LSM and Au/LSM at different temperatures (CH_4:O_2=6:1, GHSV = 7860 h^{-1})

Catalyst	Temperature	Conversion (%)	Selectivity (%)			Yield (%)	
	(°C)	CH_4	C_2	CO	CO_2	H_2	C_2
LSM	800	6.8	14.8	20.2	64.4	1.5	1.0
	900	9.4	4.8	46.5	47.4	4.3	0.5
	1,000	11.6	2.0	58.4	39.1	7.0	0.2
Au/LSM	800	14.1	19.8	20.3	59.9	3.1	2.8
	900	19.0	6.1	49.1	44.3	10.5	1.2
	1,000	22.0	2.7	63.3	33.5	14.7	0.6

Table 5.4 compares the catalytic performances of LSM and Au/ LSM between 800 and 1000 °C. The GHSV and molar ratio of CH_4/O_2 were kept at 7860 h^{-1} and 6:1, respectively. The results show that operation at a higher molar ratio of CH_4/O_2 offers higher selectivity to C2 hydrocarbons than operation at a lower molar ratio of CH_4/O_2 because oxygen becomes limited when operating at a higher value, and therefore the reactions that consume a higher number of oxygen moles (i.e., complete combustion and partial oxidation) become less favourable. Thus, the methane conversion increases with increasing operating temperature, and that operating temperature significantly influences the reaction selectivities. The yield of H_2 was slightly increased with the rising temperature. However, the H_2 yield was obviously decreased compared with the lower CH_4/O_2 ratio.There are optimum operating

temperatures that offer the maximum yields for LSM and Au/LSM. The optimum temperatures for both catalysts appear at 800 $^{\circ}$C, where the C2 hydrocarbon selectivities were 14.8% and 19.8% for LSM and Au/LSM, respectively. Increasing the operating temperature suppresses the selectivity to CO2 while promoting the selectivity to CO. The conversion of methane was rapidly increased, from 6.8% to 14.1% at 800 $^{\circ}$C, with the presence of Au.

A comparison between both catalysts clearly indicates that when Au/LSM is utilised in the reactions, the % conversion and % selectivity of C2 hydrocarbons are significantly higher than those of LSM. It was reported that the electronic interaction between the metal oxide support and the gold nanoparticles could help the gold to maintain its metallic state and increase catalytic activity [113]. Moreover, gold nanoparticles have been reported to enhance the catalyst stability as they can inhibit the formation of decomposition products such as lanthanum oxide, and can stabilize of manganese $3^{+}/4^{+}$ mixed oxidation state [24]. It should be noted that it is likely that the steam generated from the reactions could also react with methane and C2 hydrocarbons products via steam reforming to form hydrogen and carbon monoxide as the Au/LSM catalyst was reported earlier to be active for propane steam reforming [24]. Therefore, the Au nanoparticle can be concluded to promote the catalytic performance in which these results support the previous finding [24]. As a result from this work, Au/LSM is a potential anode catalyst for further application in SOFC-type reactor for the cogeneration of chemicals and electricity.

5.1.3 Catalytic performance of catalysts in SOFC reactor

After experiment in fixed bed reactor the 1%Au/LSM was tested in SOFC reactor for investigate the fuel cell performance and performance to produce C2 hydrocarbon and electrical current. Figure 5.3 shows voltage, current, and power density properties for SOFC cells fabricated by hand-painting of 1%Au/LSM with Au current collectors. The measurements from these cells at 800 $^{\circ}$C in wet H_2 and wet CH_4 are shown in figure 5.3a and 5.3b, respectively. For H_2 fuel, their open circuit voltage (OCV) values were ~1.07 V, which were very close to the theoretical value calculated from the Nernst equation. Such high OCV values indicate that a dense structure is well-formed in the YSZ electrolyte and leakage of the fuel gas is negligible for each sample. As seen in Figure 5.3a and b, the power density was 8.6 and 5.0 mW.cm-2 , respectively. From the experiments at 800 $^{\circ}$C under load 0.3 V, the methane conversion was around 3.8% and 11.6% for C2 hydrocarbons selectivity observed with a significant C2 hydrocarbon production.

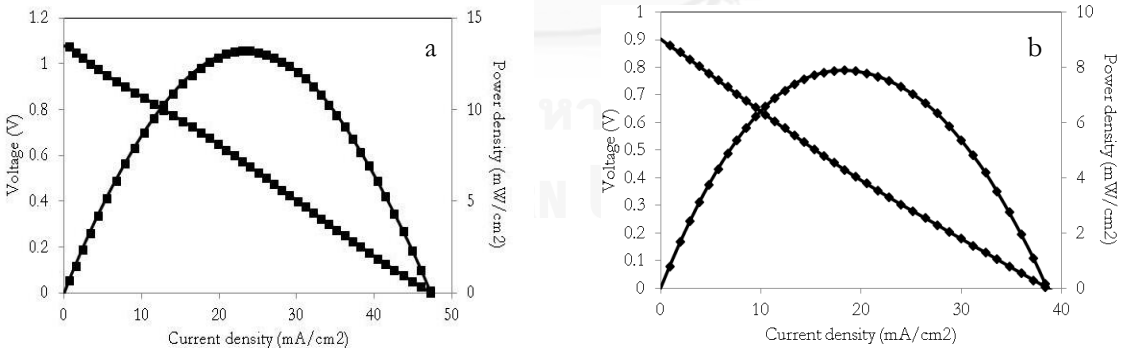

Figure 5.3 Voltage current and power density versus current density plots for the cells with each of the four anode compositions at 800 $^{\circ}$C, under wet H_2 (a) and wet CH_4 (b).

Part II

Synthesis, structure, characterization and oxidative coupling of methane over $La_{0.25}Sr_{0.75}Cr_{0.5}Mn_{0.5}O_3$ perovskite catalysts

In this part, the promising catalysts, $La_{0.25}Sr_{0.75}Cr_{0.5}Mn_{0.5}$ (LSCM) and CeO_2/ LSCM synthesized by sol-gel method were developed to be catalysts for oxidative coupling of methane reaction. This chapter started with catalysts synthesis and characterization. To investigate for their potential use in an oxidative coupling of methane (OCM) reaction in a fixed bed reactor (FBR). For SOFC cell preparation, the cell components was improved by tape- casing preparation. The ohmic resistance decreased by the reduction of the electrolyte thickness. Finally, the electrochemical performance was investigated in solid oxide fuel cell reactor (SOFC).

5.2 $La_{0.25}Sr_{0.75}Cr_{0.5}Mn_{0.5}O_3$ and Ce- $La_{0.25}Sr_{0.75}Cr_{0.5}Mn_{0.5}O_3$ anode catalysts

5.2.1 Catalytic performance of LSCM and Ce/LSCM catalysts in fixed bed reactor

The results of reactant conversions and product selectivities of LSCM and Ce-LSCM catalysts for OCM are shown in Figure 5.4 This compares the catalytic performances of catalysts between 700-900°C. The GHSV and molar ratio of CH_4:O_2:Ar were kept at 10000 ml g^{-1} h^{-1} and 4:1:5, respectively. The results show LSCM catalyst was more selective to partial oxidation than the oxidative coupling of methane reaction, as the selectivity to CO was much higher than that to CO_2. Approximately 54.5% CO selectivity and 43.2% CO_2 selectivity at 43.2% CH4 conversion with LSCM successfully obtained at 850 $^{\circ}$C. For Ce/LSCM catalyst, it was more selective to oxidative coupling of methane reaction, as the selectivity to C_2 was much higher than that to CO and CO_2. Approximately 54.5% CO selectivity and 43.2% CO_2 selectivity at

43.2% CH4 conversion with LSCM successfully obtained at 850 °C. In an analogous manner, Ce promoter addition increased methane conversion and C2 hydrocarbon selectivity. The C2+ selectivity increased when Ce was present in the catalyst. The highest C2+ (55.3%) selectivity were measured at 800 °C. The effect of temperature on products is presented in Figure 5.5 C2+ selectivity increased with temperature and passed through a maximum at 800 °C. For undesirable products, CO_2 selectivity decreased with Ce addition. The 5wt% Ce catalyst demonstrated the lowest CO2 selectivity at 750 °C. The yield of C2 hydrocarbon selective products as a function of temperature can be seen in Figure 5.5 C2 hydrocarbon yield increased and passed through a maximum value at 800 °C. Consequently, the addition of Ce promoter could promote the performance of the catalysts for the OCM reaction, and inhibited the gas phase oxidation of methane.

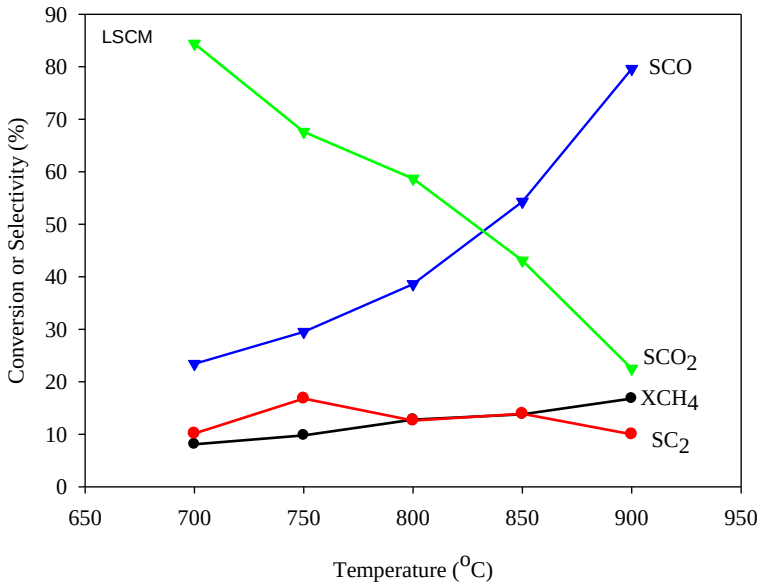

Figure 5.4 The catalytic performance of LSCM catalyst as related to operation temperatures at GHSV of 10000 ml g^{-1} h^{-1} and CH_4/O_2 of 4.

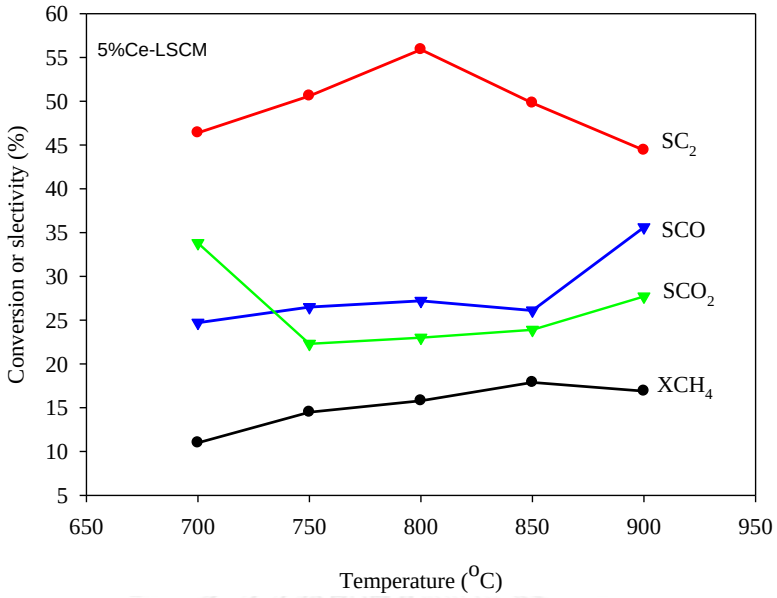

Figure 5. 5 The catalytic performance of Ce/ LSCM catalyst as related to operation temperatures at GHSV of 10000 ml g^{-1} h^{-1} and CH_4/O_2 of 4.

5.2.2 Microstructure of thin YSZ Ceramic Membrane

Tape casting procedures and slurry formulations developed by Prof Irvine and coworkers for commercial YSZ powder was used to prepare YSZ single cell. The 3-layer cast tape of YSZ powder, porous-dense-porous, was successfully co-sintered in air at 1380 °C. The results of samples are shown in Figure 5.6. The electrolyte layer with an appropriate thickness of ~50 μm maintains adequate mechanical strength to the whole sintered body. The density of the electrolyte layer was normally in the order of ~ 95 % of the theoretical density. Porous YSZ layers were achieved by the addition of graphite and glassy carbon pore formers by using 40 wt% of graphite together with 10 wt% glassy carbon in the green YSZ tape. A porosity of the final product of about 50% was normally obtained. Porous layers were adhered very well with underlying dense layers, an important requirement for transporting O^{2-} ions from the electrolyte to the electrode scaffold.

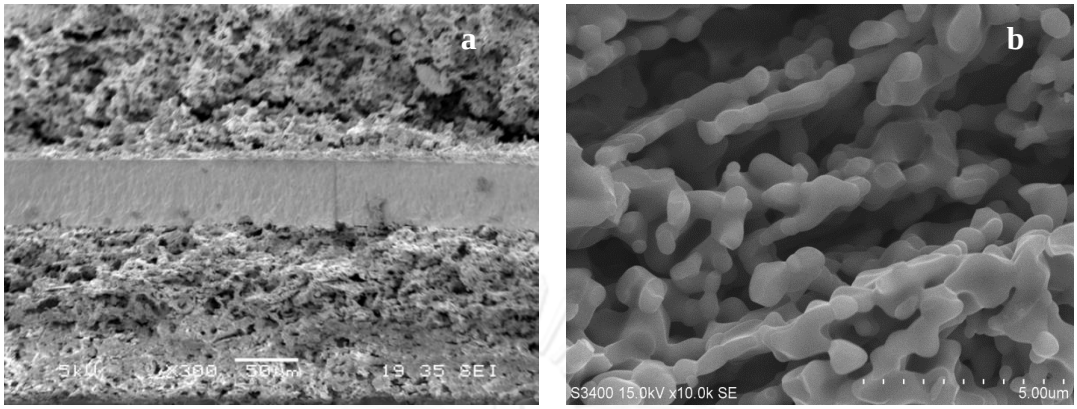

Figure 5.6 SEM images of fracture cross section of dense layer at magnifications (a) x300 and (b) porous layers. The sample was sintered in air at 1400 °C.

5.2.3 Phase compositions of impregnated electrodes

Phase identification of perovskite electrodes prepared from metal nitrates was determined by X-ray diffraction (XRD). Figure 5.7 displays the XRD patterns from the surfaces of two electrode composites comprising of LSCM and Ce-LSCM addition into electrodes. For comparison, an XRD pattern of the YSZ porous layer is also included. After the sintered at 1200 ℃, XRD peaks of LSCM were showed in figure 5.6. For CeO_2 doping, the CeO_2 peaks can be detected at 2θ as 28.6°. These data indicated that the addition of Ce promoter was not reacted with LSCM phase.

5.2.4 Microstructure of impregnated electrodes

Firstly, the firing conditions for the impregnation of the LSCM electrode were investigated. According to the literatures [18,19], the thermal decomposition of nitrate solution in air begins at 300 °C. With an intention of prevent any thermal shock that may happen in this fairly strong ceramic membrane after repeated

impregnation, the decomposition temperature of the impregnated nitrate was set at 350 °C with dwell time of 30 min. However after several impregnation cycles, the impregnated samples were completely disintegrated and delaminated. The SEM images in figure 5.8 show a significant change in the microstructure of porous layers, the SEM images of the structures LSCM indicates that the LSCM forms a uniform coating over the surfaces of the YSZ (Figure 5.8a). For CeO_2 loading, the results show the presence of nanocrystalline CeO_2 (Figure 5.8b). The estimated particle diameters for CeO_2 were 5-21 nm and uniform coating over the surfaces of the LSCM/YSZ.

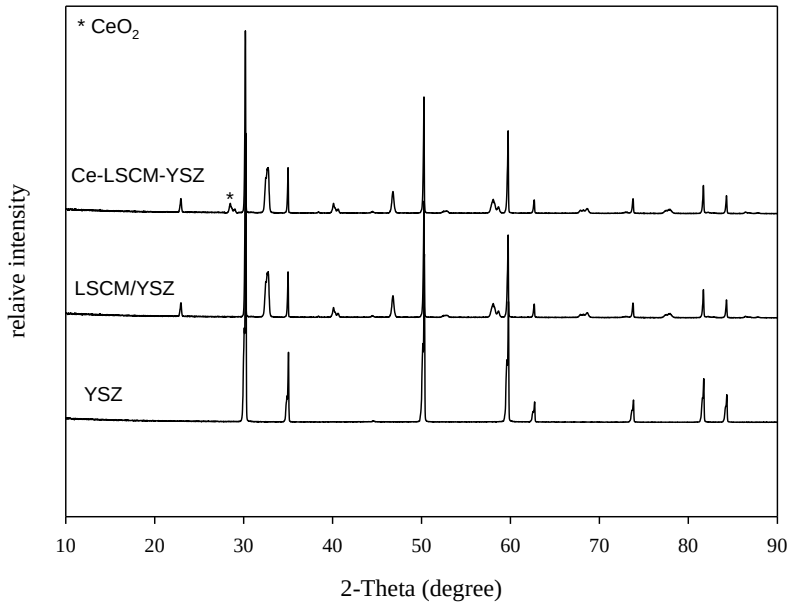

Figure 5.7 The XRD pattern of (a) YSZ, (b) LSCM/YSZ and (c) Ce-LSCM/YSZ

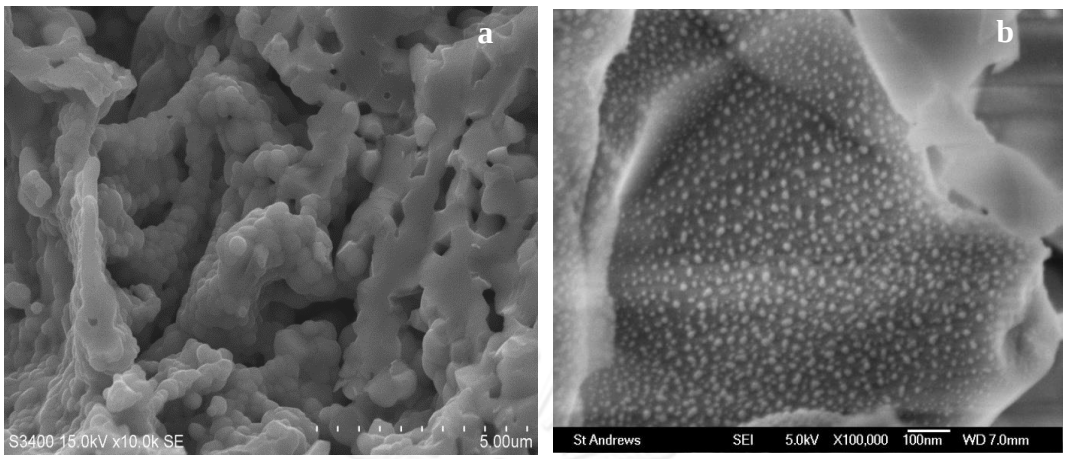

Figure 5.8 SEM images of fracture-cross section of YSZ membrane with an impregnated porous layer. (a) porous membrane with LSCM impregnated layer, (b) porous membrane with Ce/LSCM impregnated layer.

5.2.5 Electrochemical performances

Figure 5.9 shows voltage, current, and power density properties for tape-cast SOFC cells fabricated by impregnation of LSCM with CeO_2 and without CeO_2 with Ag current collectors. The measurements of these cells at 800 $^{\circ}$C are shown in Figure 5.9. Their open circuit voltage (OCV) values were ~1.02-1.08 V, which were very close to the theoretical value calculated from the Nernst equation. Such high OCV values indicate that a dense structure is well-formed in the YSZ electrolyte and leakage of the fuel gas is negligible for each sample. As seen in Figure 5.10, the power density using a LSCM anode catalyst was 123 mW cm^{-2} at 800 $^{\circ}$C. When 5 wt% of CeO2 was impregnated together with LSCM, the power density was 298 $mWcm^{-2}$. This is because the added ceria enhanced the conductivity, as well as extended effective active areas. As shown in Figure 5.10, the cell had a series resistance, RS, of 0.65 $\Omega.cm^2$ and a total resistance, RT, of 1.05 $\Omega.cm^2$ at 750 °C. As the temperature increased to 850 °C, the series resistance of the cell decreased to 0.37 $\Omega.cm^2$ and the total resistances decreased to 0.65 $\Omega.cm^2$. All the impedance

spectra captured at OCV with varying temperatures demonstrated that the resistance of the cell was greatly dominated by the polarization resistance. The power density, with respect to the temperature, for the SOFC systems studied is shown in Figure 5.11. In SOFC systems studied, there is an increase in the maximum power with increasing temperature. The addition of ceria catalysts improves performance across the entire temperature range studied. The highest power density achieved in this study were for the cell containing 5wt% CeO2 with 356 $mWcm^{-2}$ at 850 ^{o}C in humidified H_2 . These high powder densities are achieved because ceria is the most active materials for effective catalysis of the different processes in fuel oxidation. Since the cell had a low resistance and also the highest maximum power density of 336 $mW.cm^{-2}$ at 850 °C, the best performance was also obtained at 850 °C.

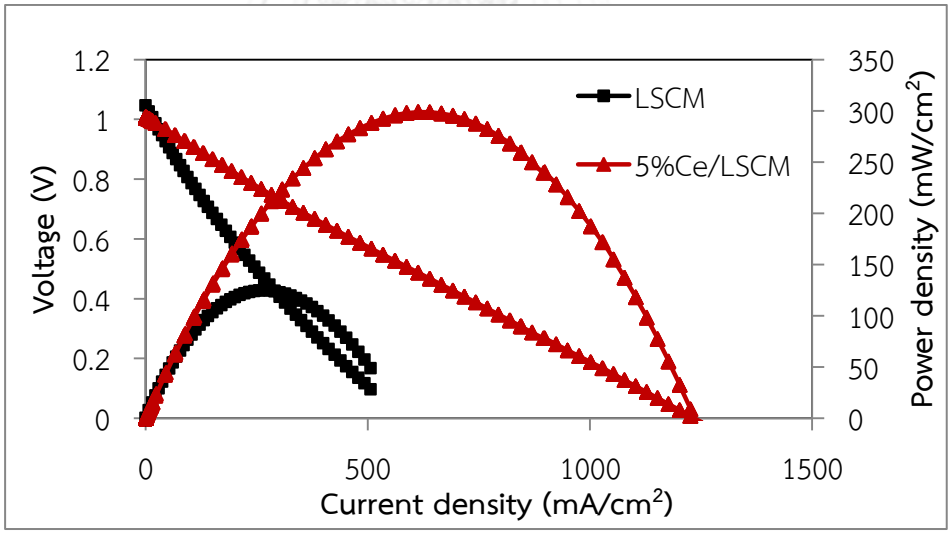

Figure 5.9 Performance curves of the 8YSZ cell with 40 wt% LSCM (a) and 5%Ce/LSCM (b) in wet humidified H_2 at 800 °C.

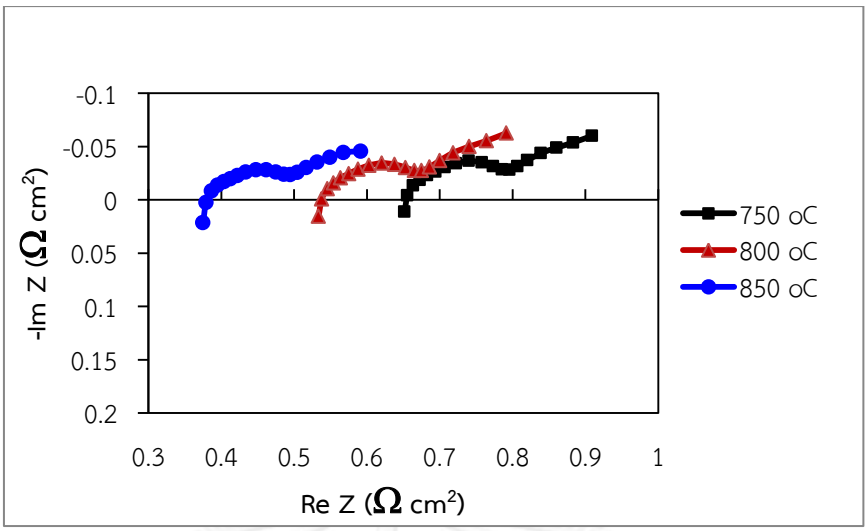

Figure 5.10 Impedance spectra of the cell with 5%ceria-40wt% LSCM as anode and 40 wt% LSF as cathode in humidified H2 at different temperatures.

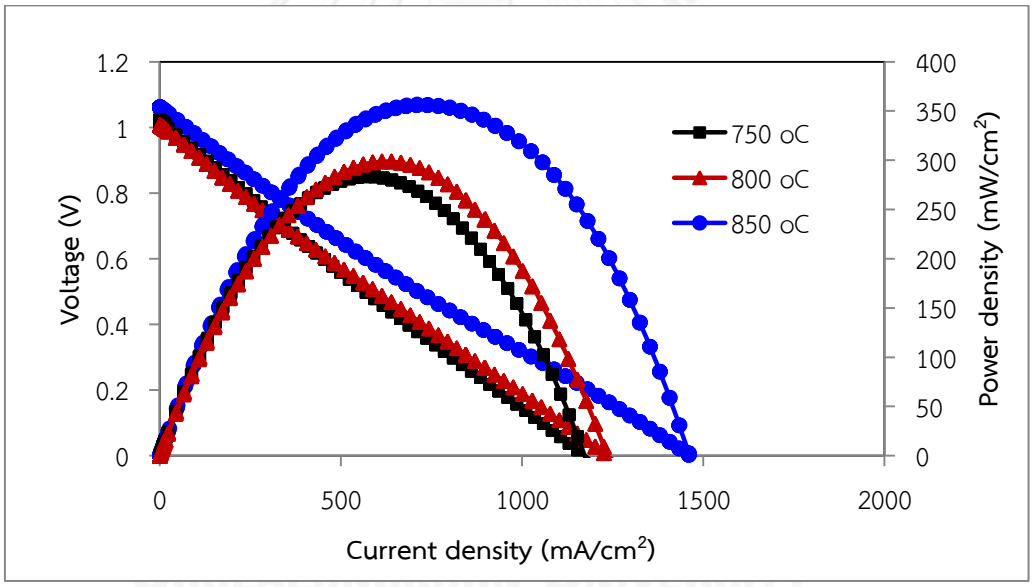

Figure 5.11 IV and performance curves of the cell with 5%ceria-40wt% LSCM as anode and 40 wt% LSF as cathode in humidified H2 at different temperatures.

5.2.6 SOFC with 5%CeO_2/LSCM anode as cogeneration of chemical and electricity

The 8YSZ cell with the 200 μm porous scaffolds were infiltrated with 40 wt% LSF and 5%CeO_2-40 wt% LSCM was used to investigate the performance of the

5%CeO_2-40 wt% LSCM anode as a cogeneration device. The cell was tested in humidified CH_4 following at the rate of 10ml/min at 750-850 °C. Impedance spectra of the cell presented in figure 5.12, shows that the maximum power with increasing temperature. The cell had a low resistance and also the highest maximum power density of 221 mW cm^2 at 850 °C, the best performance was also obtained at 850 °C in humidified CH_4 (figure 5.13). As shown in table 5.5, the methane conversion was 3.1% after applying 0.3 V to the cell for 30 minutes. At the highest methane conversion rate, the cell achieved a good C2 hydrocarbon selectivity of 78.4% and a C2 yield of 3.3% at 850 ^{o}C.

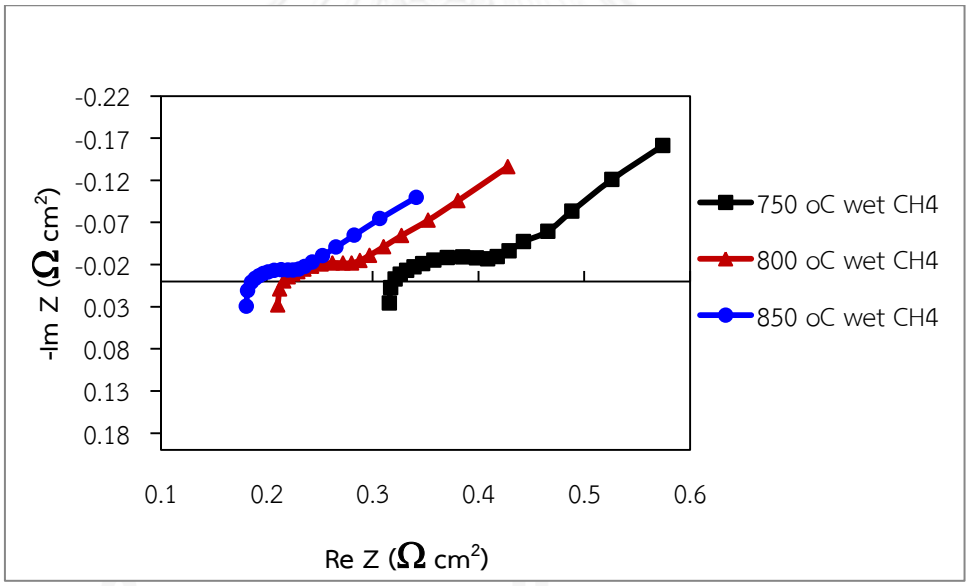

Figure 5.12 Impedance spectra of the cell with 5%ceria-40wt% LSCM as anode and 40 wt% LSF as cathode in humidified CH4 at different temperatures.

Table 5.5 The catalytic performance of the 8YSZ cell infiltrated with 5%CeO_2-40%LSCM under 0.3V at 850 °C in humidified CH_4.

Temperature (°C)	XCH_4 (%)	SC_2 (%)	SCO_2(%)	YC_2(%)
800	3.1	69.8	25.8	2.6
850	3.4	78.4	16.7	3.3

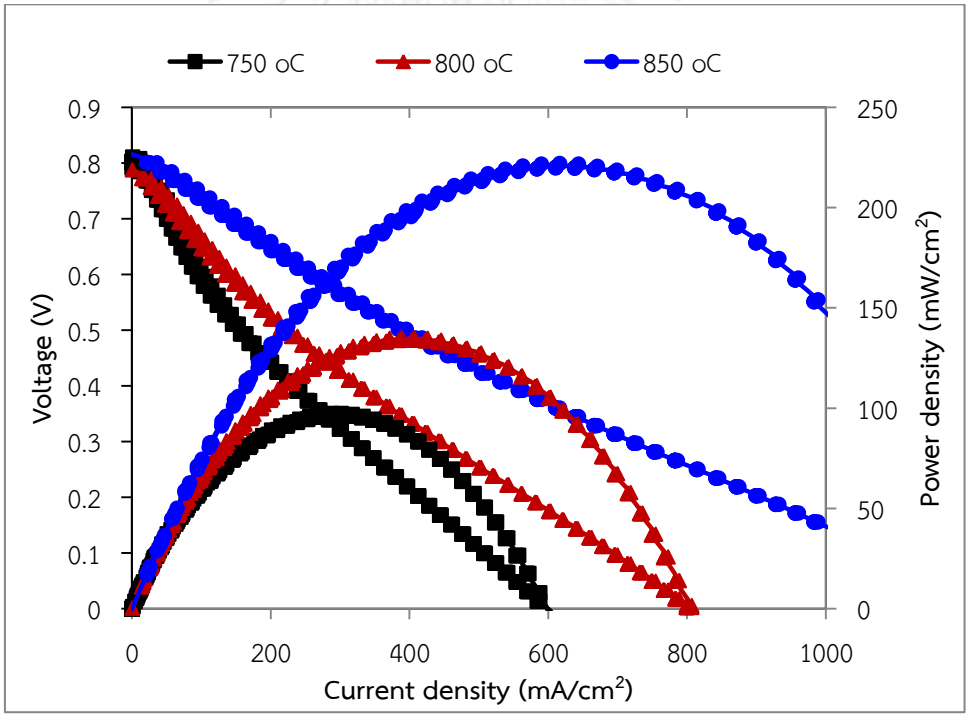

Figure 5. 13 IV and performance curves of the cell with 5%ceria-40wt% LSCM as anode and 40 wt% LSF as cathode in humidified CH4 at different temperatures.

Part III

Characterization and oxidative coupling of methane activity over $LiFeO_2$ catalyst

The system Li–MgO is well known as a selective catalyst for the oxidative coupling of methane (OCM) and has been intensely investigated because of its high reactivity and C2 selectivity. Lunsford et al reported that Li^+-O^- centers in/on Li-MgO, which are in equilibrium with surface O^- centers via hole transport, play an important role for the activation of CH_4 [33, 34, 131]. However, direct observation of the Li^+- O^- center is difficult because it is present at high temperatures and forms only in an O_2 atmosphere [132]. High C2 hydrocarbon selectivity of the system are accompanied by relatively high temperatures (780 °C) and a loss of Li during catalytic performance [36]. Due to the volatile character of the Li compounds and the following decreasing stability of the catalyst investigations became fewer during the past. Moreover, Li-MgO has low electrical conductivity so it was required to develop by doping another metal [37, 38, 131].

$LiFeO_2$ with similar rock-salt structure to $LiCoO_2$ are potentially very attractive electrode for rechargeable lithium batteries because of their much lower cost and toxicity compared with $LiCoO_2$ used in the vast majority of present day cells. Morales and Santos-Peña have studied $LiFeO_2$ as potential alternative electrode to $LiCoO_2$ [133], they reported that lithium iron oxide increases the electrochemical activity of the cell.

In this part, $LiFeO_2$ (LFO) was examined. The surface morphology, composition and surface area were characterised by several techniques. The catalytic activity of catalysts for oxidative coupling of methane and the influence of some operating variables, i.e., temperature were investigated in detail over a fixed bed reactor. After that, electrocatalytic materials for anode and cathode were introduced into LSGM porous scaffold by ion impregnation method. Finally, the catalytic behavior in the oxidative coupling of methane reaction over and LFO anode electrode was assessed to determine the potential for the production of chemicals and electrical power in an SOFC-type reactor.

5.3 $LiFeO_2$ (LFO) anode catalysts

5.3.1 Catalytic performance of catalysts in fixed bed reactor

The results of reactant conversions and product selectivities of LFO catalysts prepared by solid state reaction methods for OCM are shown in figure 5.14. This compares the catalytic performances of LFO between 700-850°C. The GHSV and molar ratio of CH_4:O_2:Ar were kept at 10000 ml g^{-1} h^{-1} and 4:1:5, respectively. The results show that the methane conversion increases with increasing operating temperature, and that operating temperature significantly influences the reaction selectivities. There are optimum operating temperatures that offer the maximum yields for LFO. The optimum temperatures appear at 750 $^{\circ}$C, where the C2 hydrocarbon selectivity was 82.3%. Increasing the operating temperature from 700 to 750 $^{\circ}$C, the conversion of methane was rapidly increased, from 12.6% to 17.7% with increasing C2 hydrocarbon selectivity. J. Wang and co-worker have been clarified that the active oxygen species was surface lattice oxygen O_s^{2-} for catalyst, and transport of gas-phase oxygen molecules to lattice oxygen ions over surface catalytic sites is

the key step toward the formation of active oxygen species, which in turn debased the conversion of methane. However, increasing of temperatures from 750 °C, C2 hydrocrabon selectivity decreasing due to the bulk lattice oxygen more likely began to release, which facilitated the deep oxidation process of hydrocarbon [12].

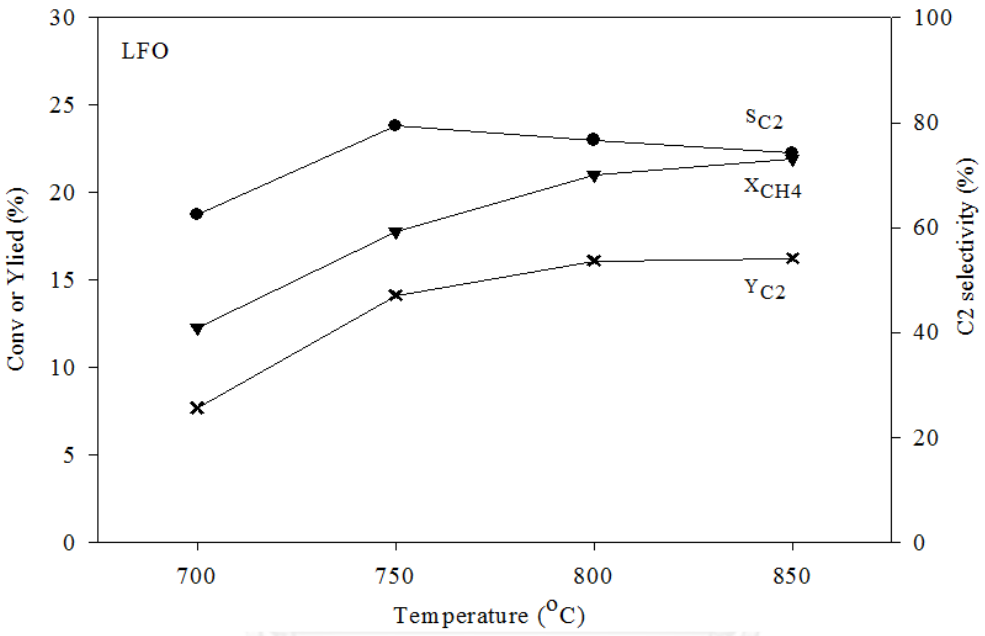

Figure 5.14 The catalytic performance of $LiFeO_2$ catalyst as related to operation temperatures at GHSV of 10000 ml g^{-1} h^{-1} and CH_4/O_2 of 4.

Based on the data of catalytic performance, there were comparable operating temperatures for OCM reaction over LFO catalysts prepared by the solid state reaction method considering the stability test at 750 ^{o}C was investigated in this study. Figure 5.15 shows that LFO catalyst was stable throughout a 30 h run at 750 °C, 10000 ml g^{-1} h^{-1} GHSV and CH_4/O_2 =4. CH_4 conversion maintained at 15-17% and C2 selectivity was 73–79%.

The XRD pattern of LFO powder after testing in the FBR showed higher intensity of peaks compared to before testing (figure 5.16). In addition, the carbon peak at $2\theta = 28^{\circ}$ was not detected after testing. After 30 hours in in 10000 ml g^{-1} h^{-1} GHSV and CH_4/O_2 = 4 at 750 ℃, the surface area of LFO decreased to 2.9 $m^2 g^{-1}$ compared to that of 3.2 $m^2 g^{-1}$ before testing (Table 5.6). The pore size of the LFO powder also decreased after testing. SEM images of LFO powder before and after testing in figure 5.17 demonstrate that LFO particles had increased in size, which reflected the decreased in surface area. In addition, the particles of the spent LFO seemed to be necking together which reduced the porosity of the powder.

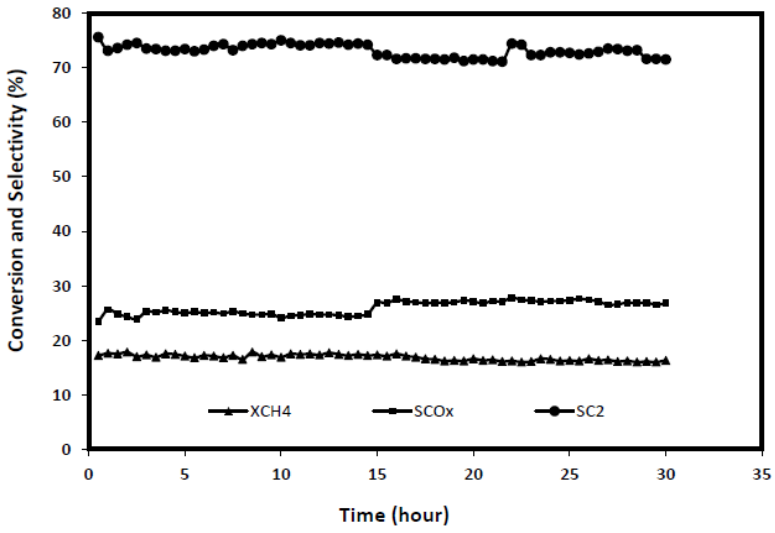

Figure 5.15 Methane oxidative reaction of LFO as a function of time at 750 ℃, 10000 ml g^{-1} h^{-1} GHSV and CH_4/O_2 =4.

Table 5.6 Surface areas, average pore size and pore volume.

Catalyst	BET-surface (m2/g)	Pore volume (cm3/g)	Pore size (nm)
[a]LiFeO2	3.2	0.008	13.4
[b]LiFeO2	2.9	0.008	13.0

[a] Catalysts as prepared. [b] Catalysts as after catalytic reactions at 750 °C.

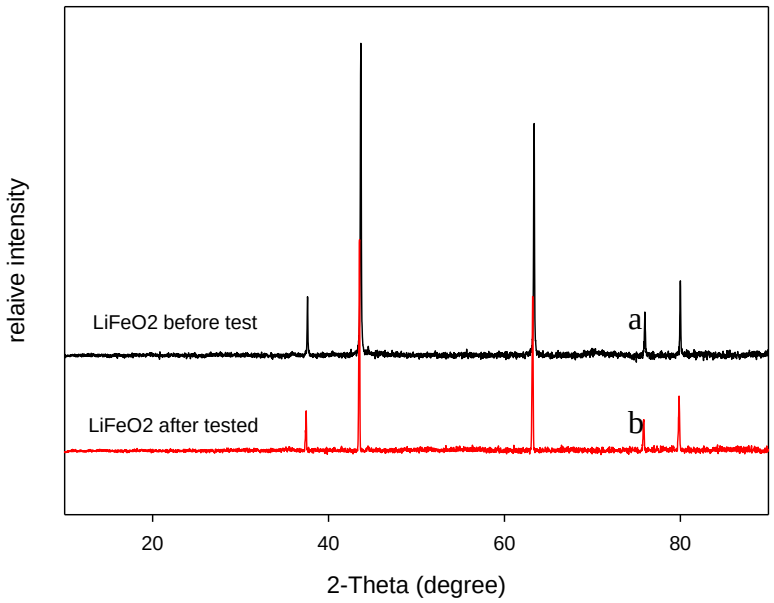

Figure 5.16 The XRD patterns of fresh and after 30 h run LiFeO2 catalyst: (a) fresh catalyst; (b) 30 h used catalyst.

5.3.2 Performance of LFO Anode

5.3.2.1 Testing of cell infiltrated with 30 wt% LFO for the anode and 40wt% LSF for the cathode on 8YSZ

The cross-sectional images YSZ single cell show in figure 5.6a, the sintered cell had an electrolyte thickness of 50 μm and a porous of 200 μm. The fabrication of the fuel cell started with infiltrating the LSF aqueous nitrate solution into the 8YSZ scaffold for the cathode. The LSF infiltrated 8YSZ electrode was heat treated at 450 °C to decompose the nitrate. Once the impregnation process for the cathode reached 40 wt%, the cell was sintered at 850 °C for 3 hours. The anode was impregnated with the LFO nitrate solution to obtain 30 wt% or 40 wt% then sintered at 700 °C for 3 hours.

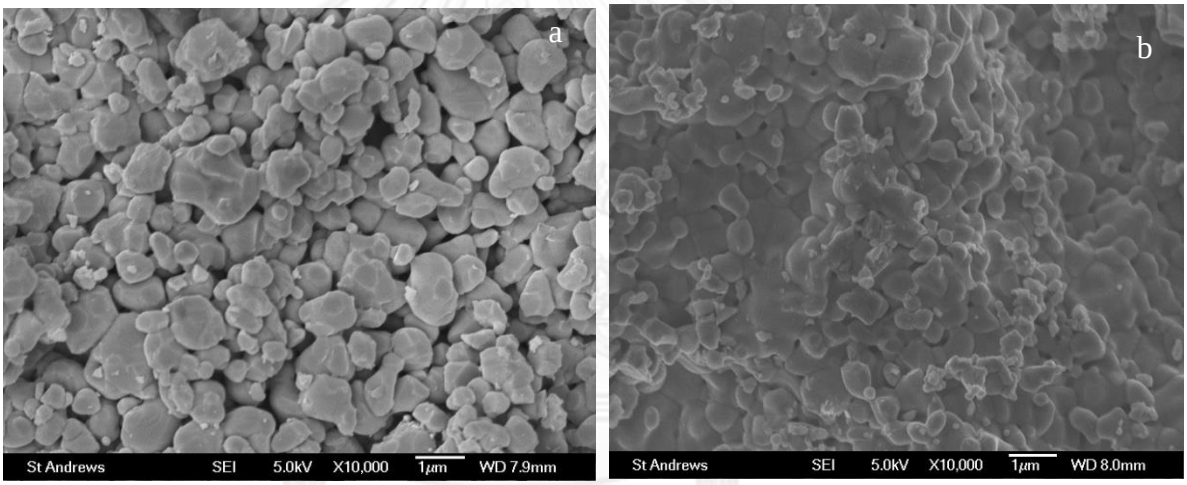

Figure 5.17 SEM micrograph of fresh and after 30 h run $LiFeO_2$ catalyst: (a) fresh catalyst; (b) 30 h used catalyst.

Figure 5.18 displays the cross-sectional images of the scaffold before and after the infiltration of the functional materials. SEM images showed that nano-LSF particles were successfully deposited onto the 8YSZ scaffold. The LFO particles also formed a continuous coating over the scaffold. However, the particle size of the deposited LFO seemed to be larger than that of the LSF. Silver wires and paste (SPI Supplies) were used as the current collector, which defined the working area of 0.35 cm^2 of the cell. Initial fuel cell performance was examined on the 8YSZ electrolyte-

supported cell infiltrated with 40 wt% LSF for the cathode and 30 wt% for the anode. Impedance spectroscopy was performed at open-circuit-voltage (OCV) with a range of temperatures in humidified (3% H_2O) H_2. VI measurements were also conducted on the same cell at different temperatures in humidified H_2. As shown in Figure 5.19, the cell had a series resistance, RS, of 0.32 $\Omega.cm^2$ and a total resistance, RT, of 0.9 $\Omega.cm^2$ at 700 °C. As the temperature increased to 750 °C, the series resistance of the cell decreased to 0.30 $\Omega.cm^2$ but the total resistances increased to 1.3 $\Omega.cm^2$. However, the ASR of the cell increased as the testing temperature rose to 800 °C. All the impedance spectra captured at OCV with varying temperatures demonstrated that the resistance of the cell was greatly dominated by the polarization resistance. Since the cell had a low ASR and also the highest maximum power density of 168 mW cm^2 at 750 °C, the best performance was also obtained at 750 °C (figure 5.20).

The performance of the 8YSZ electrolyte-supported cell infiltrated with LFO decrease at high temperature because 8YSZ and LFO were reacting with each other. This reaction caused the cell to perform poorly. Moreover, the reaction between LFO and 8YSZ seems to reduce the electronic conductivity of 8YSZ scaffold infiltrated with LFO. As the results, the cell potential decreased with increasing testing temperature. $La_{0.9}Sr_{0.1}Ga_{0.8}Mg_{0.2}O_3$ (LSGM) is a good oxide conductor for high temperature SOFC. LSGM conductivity is one magnitude higher than that of YSZ [134-136]. Due to these reasons, LSGM was used to further the investigation of LFO performance as a SOFC anode material operating at temperature greater than 650 °C.

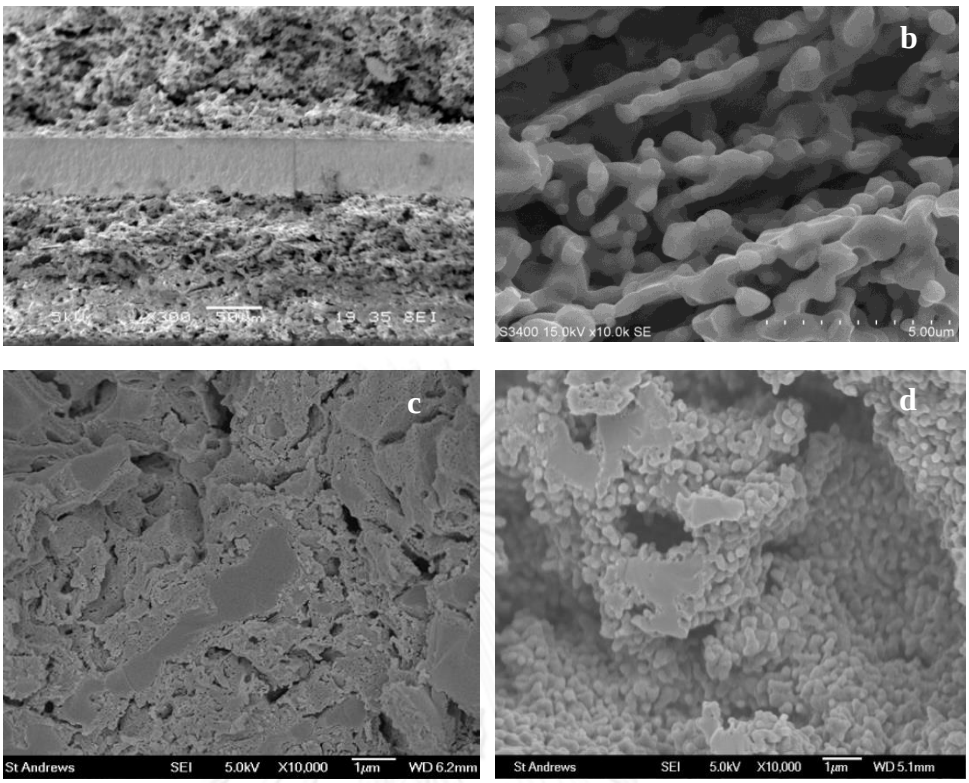

Figure 5.18 Cross-sectional images of (a) YSZ single cell (b) empty 8YSZ scaffold and scaffold infiltrated with (c) 40 wt% LSF and (d) 30 wt% LFO.

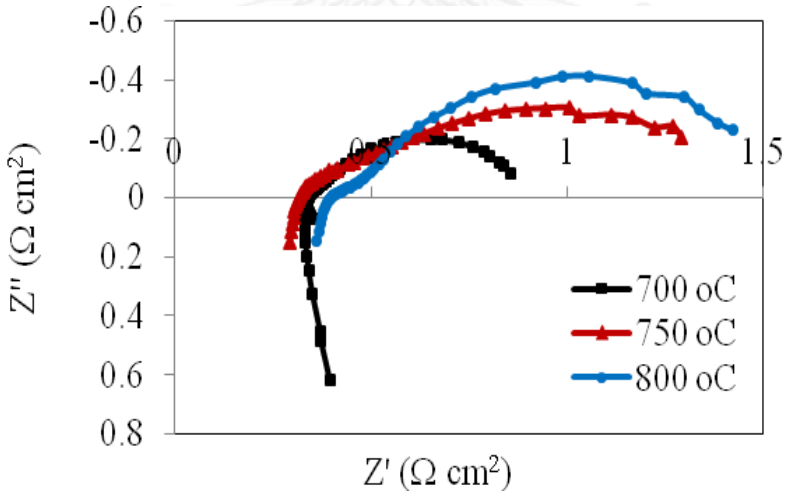

Figure 5.19 Impedance spectra of the cell with 30 wt% LFO as anode and 40 wt% LSF as cathode in humidified H_2 at different temperatures.

5.3.2.2 Testing of cell infiltrated with 30 wt% LFO for the anode and 40wt% LSC for the cathode on LSGM

The cell was prepared the same section 5.2.2.1. $La_{0.6}Sr_{0.4}CoO_3$ (LSC) nitrate solution was used to infiltrate the cathode and $LiFeO_2$ (LFO) nitrate solution for the anode. The cell was heated to 450 ˚C to decompose the nitrate. The infiltration and heat treatment processes were repeated until the electrode reached the desired weight. The final sintering temperature for the scaffold infiltrated with the LSC cathode material was 1000 ˚C with a dwell of one hour. The final sintering temperature and time of the LSGM scaffold impregnated with 30 wt% LFO remained the same at 700 ˚C with a dwell of 3 hours.

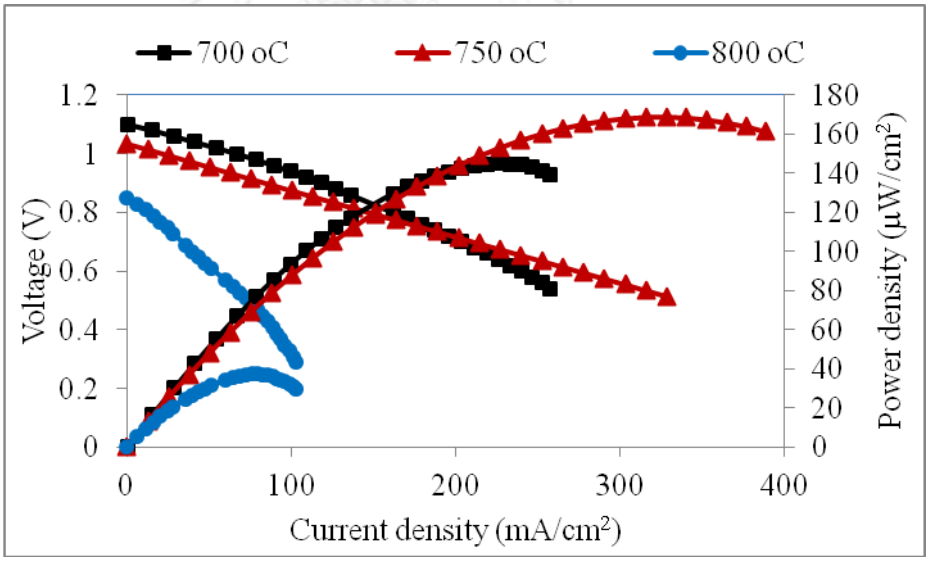

Figure 5.20 IV and performance curves of the cell with 40 wt% LFO as anode and 40 wt% LSF as cathode on 8YSZ in humidified H_2 at different temperatures.

During the infiltration process, the nitrate solution of the functional material did not leak to the other side of the sample, suggesting that a dense electrolyte layer was successfully formed. SEM images shown in figure 5.21 demonstrate that small particles of LSC and LFO were deposited and formed a continuous coating over the porous LSGM scaffold. Since the final sintering temperature of LFO was much lower than that of LSC, the LFO particles were smaller compared to that of LSC.

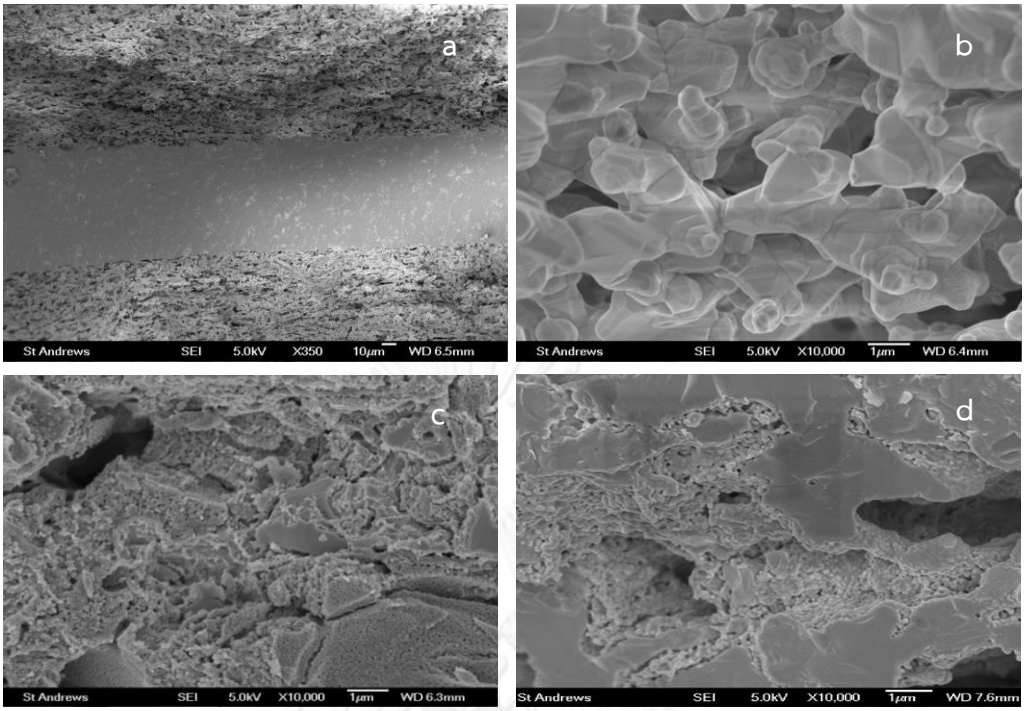

Figure 5. 21 Cross-sectional SEM images of a) the entire empty LSGM scaffold and b) zoomed in; LSGM scaffold infiltrated with c) 30 wt% LFO for the anode and d) 40 wt% LSC for the cathode.

Silver wires and paste were used also as the current collectors for the LSGM cells. The silver wire was wound into a ring that formed an active area of 0.635 cm^2. The silver paste was use to adhere the silver ring onto the electrodes. Once the silver paste was dried, the sample was sintered at 450˚C for 1 hour.

The fuel cell experimental set up for the LSGM samples were the same as the 8YSZ cell presented in Figure 4.2.

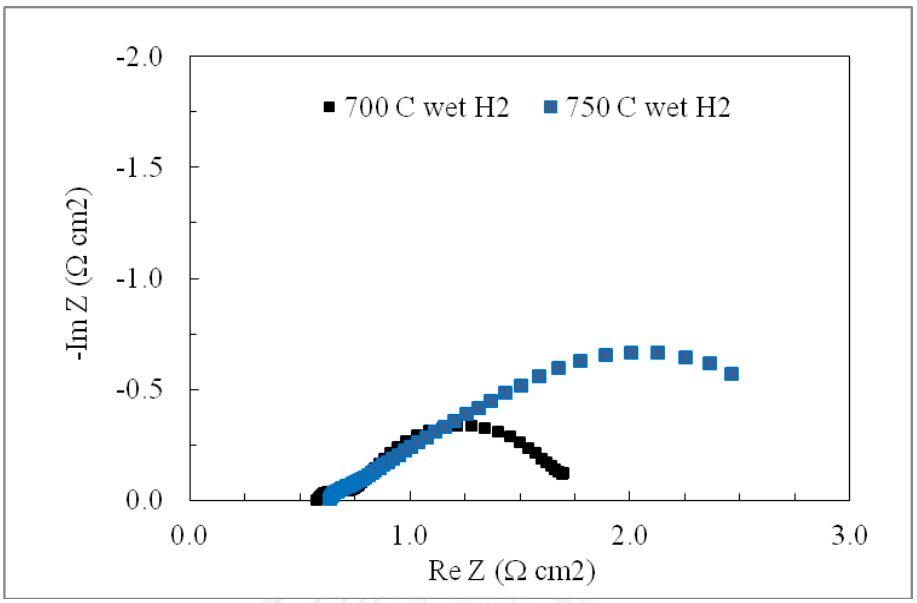

Figure 5.22 Impedance spectra at OCV of the LSGM1 cell having an electrolyte thickness of 100 μm and infiltrated with 40 wt% LSC for the cathode and 30 wt% LFO for the anode at different temperatures in humidified H_2.

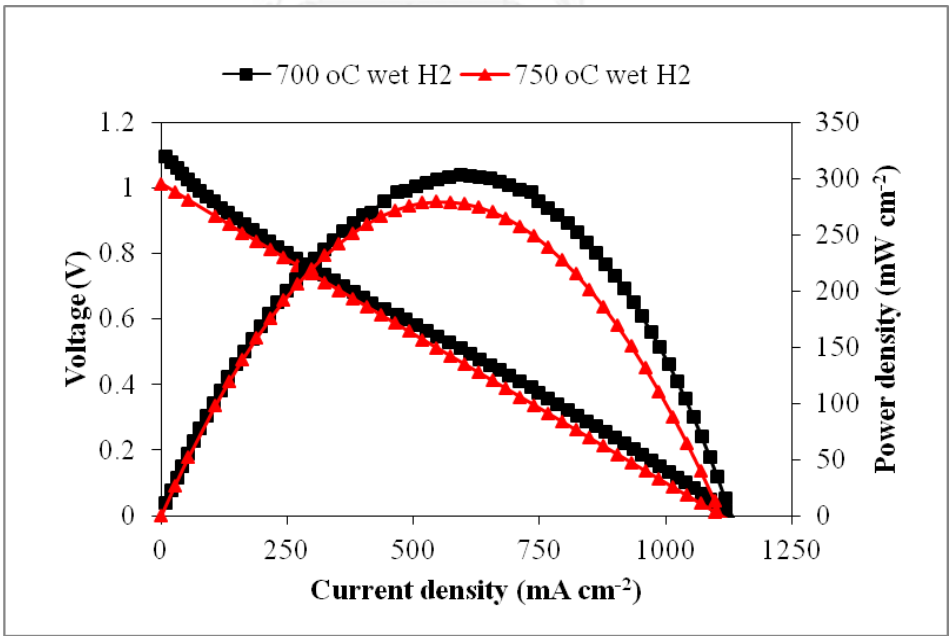

Figure 5.23 Voltage and performance curves of the cell LSGM1 at different temperatures in humidified H_2.

The LSGM electrolyte-supported cell used in this study was labeled LSGM1 and had an electrolyte thickness of 100 μm. The performances of the LSGM1 cell were investigated at different temperatures in humidified H_2 flowing at the rate of 20ml/min. The impedance spectra captured at OCV, 1.09 V, in Figure 5.22 shows that the LSGM1 cell infiltrated with 40wt% LSC for the cathode and 30 wt% LFO for the anode obtained a series resistance of 0.28 $\Omega.cm^2$ at 700 ˚C. With a total resistance of 1.8 $\Omega.cm^2$, the cell yielded a polarization resistance of 1.23 $\Omega.cm^2$. As temperature reached 750 ˚C, the total resistance of the cell at OCV, 1.02 V, increased to 2.80 $\Omega.cm^2$ where 0.64 $\Omega.cm^2$ was contributed by the series resistance. The resistance of the cell increased by 1.57 $\Omega.cm^2$ from 700˚C to 750 ˚C, the overall resistance of the cell obtained at 750 ˚ due to the microstructure of LFO changes with time and temperature by agglomerating and forming larger particles. The change in the microstructure could have an effect on bonding between the anode and the current collector which could explain the increase in series resistance as the testing temperature increased. The performances of the LSGM cell presented in figure 5.22 reflect the changes in the resistance at different temperatures in humidified H_2. As shown in figure 5.23, the cell obtained an initial maximum power density of 303 mW cm^{-2} at 700 ˚C. As the testing temperature increased to 750 ˚C, the cell had a maximum power density decrease to 279 mW cm^{-2}.

5.3.3 SOFC with LiFeO2 anode as cogeneration of chemical and electricity

The LSGM cell with the 230 μm porous scaffolds were infiltrated with 40 wt% LSC and 30 wt% LFO was used to investigate the performance of the LFO anode as a cogeneration device. The cell was tested in dry and humidified CH_4 following at the

rate of 10ml/min at 750 °C. Impedance spectra of the cell presented in figure 5.24 show that the cell obtained a series resistance of 0.245 Ω cm^2 in humidified (3% H_2O) CH_4. The series resistance of the cell increased slightly to 0.262 Ω cm^2 when the fuel was switched to dry methane. In addition, the captured impedance spectra in both wet and dry CH_4 showed sign of limited diffusion. However, the polarization of the cell in wet CH_4 seemed to be smaller compared to that in dry CH_4.

As shown in figure 5.25 below, the OCV value of the cell was slightly higher in dry CH_4 than wet CH_4. The cell obtained an OCV value of 0.82 V in dry methane compared to 0.79 V in wet CH_4. The performance of the cell was also better in dry methane than wet methane. The cell obtained a maximum power density of 29 mW cm^{-2} in dry CH_4. In order to observe the amount of chemical generated from the cell, the cell was put under a bias voltage of 0.3 V. As shown in figure 5.6, methane conversion was around 0.5% at OCV in humidified CH_4. However, the methane conversion increased to 3.1% after applying 0.3 V to the cell for 30 minutes. At the highest methane conversion rate, the cell achieved a good C2 hydrocarbon selectivity of 85.2% and a C2 yield of 2.6% (Table 5.3).

Table 5.7 The catalytic performance of the LSGM cell infiltrated with 30 wt% LFO under 0.3V at 750 °C in humidified and dry CH_4.

CH_4	XCH_4 (%)	SC_2 (%)	SCO_2(%)	YC_2(%)
Wet	3.1	85.2	9.5	2.6
Dry	3.4	83.4	9.1	2.8

When the fuel was changed to dry methane, the maximum power density of the cell increased to 32 mW cm^{-2}. There was little change in the methane conversion. In dry methane, the methane conversion was 3.4% compared to 3.1% in humidified CH_4. However, the selectivity of methane decreased slightly to 83.4% in the dry fuel condition compared to 85.2% in wet methane.

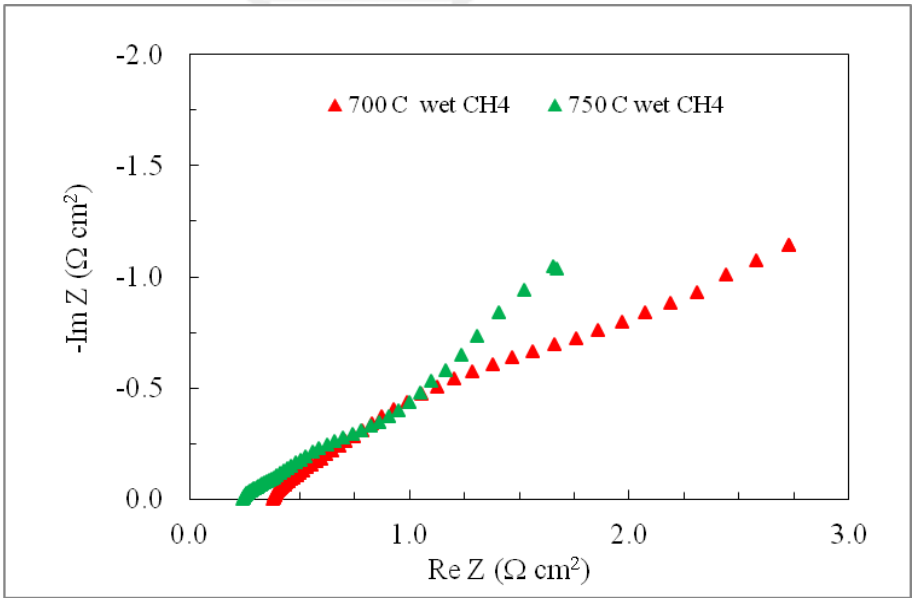

Figure 5.24 Impedance spectra of LSGM electrolyte-supported cell infiltrated with 30 wt% LFO for the anode and 40 wt% for the cathode at OCV in humidified CH_4 at different temperatures.

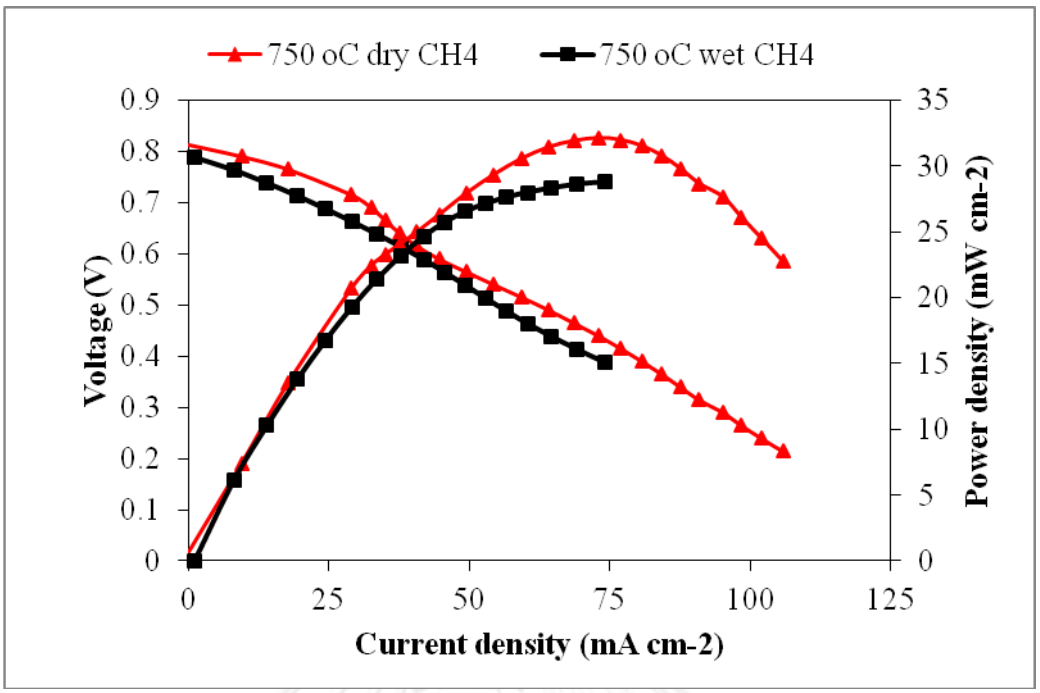

Figure 5.25 Performance curves of the LSGM cell with 30 wt% LFO in humidified or dry CH_4 at 750 °C.

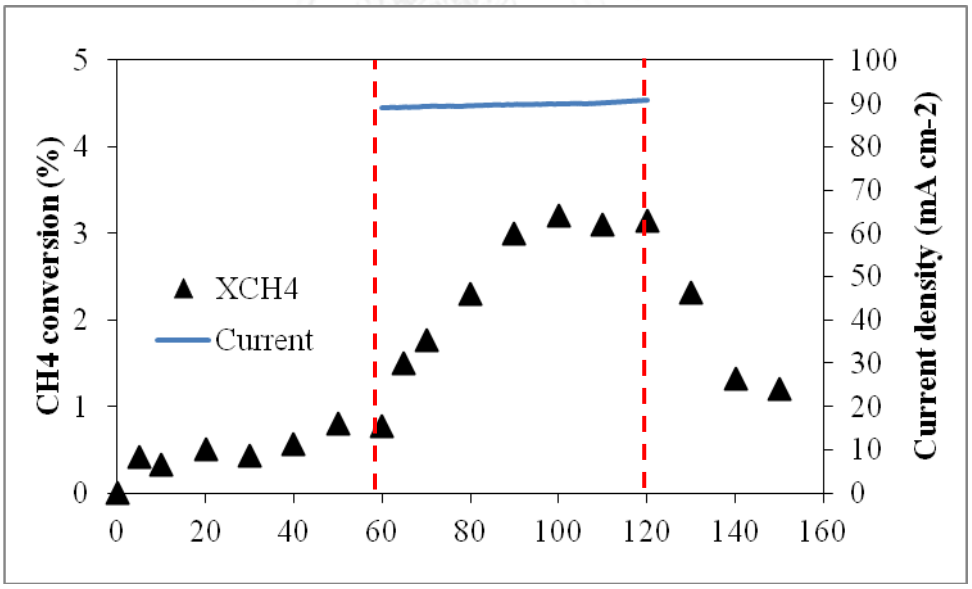

Figure 5. 26 Methane conversion and current density of the LSGM cell with 30 wt% LFO in humidified CH_4 at 750 °C.

CHAPTER VI
CONCLUSIONS AND RECOMMENDATIONS

6.1 Conclusions

In search of new anode material for co-generation C2 hydrocarbon and electricity using SOFC reactor, Au/ $La_{0.4}Sr_{0.6}MnO_3$, $La_{0.25}Sr_{0.75}Cr_{0.5}Mn_{0.5}$ (LSCM), CeO_2/ LSCM and $LiFeO_2$ were considered. The project addressed the study of the performance of catalysts for OCM reaction in fixed bed reactor and solid oxide fuel cell reactor. Moreover, study of the electrolyte ceramic preparation to improve the cell performance via tape casting and ion impregnation.

6.1.1 Performance of Au/ $La_{0.4}Sr_{0.6}MnO_3$ catalyst

The characterization results showed that Au nanoparticles could significantly improve the catalytic performance of the composite. Its activity was tested in a fixed bed reactor at two different ratios of CH_4/O_2. A 79.6% CO selectivity and a 54.7% CH_4 conversion were obtained at a low CH_4/O_2 ratio; however, at higher CH_4/O_2 ratios, the selectivity of C2 became significant. With the presence of Au, the CH_4 conversion, H_2 yield and C_2 and CO selectivity were improved. The effect of Au addition of 1 wt.% and 3 wt.% to LSM showed some influences on C2 selectivity, CH_4 conversion, except for 5 wt.% which showed no catalytic activity. Thus, it is recommended that Au/LSM is not suitable to use in a methane oxidative coupling process but it is possible to be used in a partial oxidation fixed bed reactor and an SOFC reactor.

6.1.2 Performance of $La_{0.25}Sr_{0.75}Cr_{0.5}Mn_{0.5}$ (LSCM) and CeO_2/ LSCM catalysts

The catalytic activity for oxidative coupling of methane (OCM) was measured in a fixed bed reactor (FBR) and solid oxide fuel cell reactor (SOFC). Approximately 54.5% CO selectivity and 43.2% CO_2 selectivity at 43.2% CH4 conversion with LSCM successfully obtained at 850 ^{o}C for Ce/LSCM catalyst. The addition of Ce promoter could promote the performance of the catalysts for the OCM reaction, and inhibited the gas phase oxidation of methane. The improvement of cell performance was carried out by decreasing the thickness of the electrolyte and utilising a high catalytic activity electrode. The tape casting method was employed in order to reduce the electrolyte thickness and prepare porous ceramic support for the electrode material. The electrode materials were introduced into porous YSZ support by ion impregnation technique and a composite electrode/electrolyte was achieved. The impregnated LSCM was synthesized at temperatures over 700 ^{o}C and did not react with 8YSZ at 1200 ^{o}C. Tape-cast SOFCs with impregnated LSCM exhibited excellent performance when CeO_2 was used as catalysts. A SOFC with a composite anode 5%CeO_2- 40 wt% LSCM exhibited maximum power density 221 mW cm^{-2} at 850 ^{o}C in humidified methane. Under a load of 0.3V, 3.4% CH_4 conversion and 78.4% C2 selectivity were obtained.

6.1.3 Performance of $LiFeO_2$ catalyst

In search of new anode material for SOFC application, $LiFeO_2$ was considered. The prepared LFO formed a high temperature, disordered (α) cubic phase. Particle sizes of pellets sintered at 850°C are between 2 and 5 μm. The application of LFO infiltrated in electrodes in a single cell provided interesting results for electrocatalytic C2 hydrocarbon synthesis at 750 °C. The catalytic activity for oxidative coupling of

methane (OCM) was measured in a fixed bed reactor (FBR) and solid oxide fuel cell reactor (SOFC). A 17.8% CH_4 conversion and 79.4% C2 selectivity were obtained in a FBR at 750 ^{o}C and 4:1 CH_4/O_2 ratio. For SOFC system, ceramic anodes were prepared by aqueous impregnation yielding composites with 30 wt% LFO in porous $La_{0.8}Sr_{0.2}Ga_{0.8}Mg_{0.2}O_3$ (LSGM) scaffold. A SOFC with a composite anode 30 wt% LFO exhibited maximum power density 21 mW cm^{-2} at 750 ^{o}C in dry methane. Under a load of 0.3V, 3% CH4 conversion and 85% C2 selectivity were obtained.

6.2 Recommendations for Future Works

The results from the formation of C2 hydrocarbon suggests that a vital factor that controls the rate of C2 hydrocarbon formation would be the number of active sites on the anode catalyst. Therefore, the increase of the electrode active area should provide the higher amount of C2 hydrocarbon and lower the amount of CO_2 produced. This can be done by increasing size of the button cell or changing the geometry of the cell to a tubular cell which can be easily performed via tape casting process.

$La_{0.25}Sr_{0.75}Cr_{0.5}Mn_{0.5}$ (LSCM) perovskite structure is suitable for high temperature operation (750-900°C) because Cr doped LaSrMnO3 played a vital role in increasing resistance to coking (as well as raising sulphur tolerance). However, C2 hydrocarbon selectivity was low. A mixed ionic–electronic conductor (MIEC) anode can extend the reaction zone from the triple phase boundaries (TPBs) to the whole electrode/gas interface, thus minimizing the electrode overpotential. Therefore, materials with significant ionic contribution to the overall conductivity are preferred. Among the large number of perovskite oxides investigated so far, Sr- and Mg-

substituted LaGaO3 (LSGM) is prominent due to its pure and high oxide ion conductivity at intermediate temperatures over a wide range of oxygen partial pressures ($p(O_2)$). Substitution of this material by high amounts of Mn at the B-site successfully improved the electronic conductivity, making it a good anode candidate. However, gallium is expensive and LSGM has some stability problems due to the high volatility of the gallium component in the anode atmosphere by the formation of GaOH(g). As an analog to $LaGaO_3$-based material, $LaAlO_3$-based material has been considered as an anode Material. Although $LaAlO_3$-based materials have lower ionic conductivity than LSGM, they show much higher ionic conductivity than $LaCrO_3$-based materials. Through appropriate substitution at the Al-site by transition metal elements (e.g. Mn), it is anticipated to improve the electronic conductivity in a similar way to LaGaO3-based materials. Therefore, $(La_{0.8}Sr_{0.2})_{0.94}\,Al_{0.5}Mn_{0.5}O_{3-\delta}$ (LSAM) is a one attractive catalysts for OCM reaction.

REFERENCES

1. Tagawa, T., et al., *Design of electrode for solid oxide fuel cells reactor.* Solid State Ionics, 1998. **106**(3–4): p. 227-235.
2. Steele, B.C.H., *Material science and engineering: The enabling technology for the commercialisation of fuel cell systems.* Journal of Materials Science, 2001. **36**(5): p. 1053-1068.
3. Stambouli, A.B. and E. Traversa, *Solid oxide fuel cells (SOFCs): a review of an environmentally clean and efficient source of energy.* Renewable and Sustainable Energy Reviews, 2002. **6**(5): p. 433-455.
4. Neophytides, S. and C.G. Vayenas, *Chemical cogeneration in solid electrolyte cells. The oxidation of CH3OH to H2CO.* Journal of the Electrochemical Society, 1990. **137**(3): p. 839-845.
5. Michaels, J.N. and C.G. Vayenas, *STYRENE PRODUCTION FROM ETHYLBENZENE ON PLATINUM IN A ZIRCONIA ELECTROCHEMICAL REACTOR.* Journal of the Electrochemical Society, 1984. **131**(11): p. 2544-2550.
6. Vayenas, C.G. and S. Neophytides, *Non-faradaic electrochemical modification of catalytic activity III. The case of methanol oxidation on Pt.* Journal of Catalysis, 1991. **127**(2): p. 645-664.
7. Sigal, C.T. and C.G. Vayenas, *Ammonia oxidation to nitric oxide in a solid electrolyte fuel cell.* Solid State Ionics, 1981. **5**(0): p. 567-570.
8. Yentekakis, I.V. and C.G. Vayenas, *Chemical Cogeneration in Solid Electrolyte Cells: The Oxidation of to.* Journal of The Electrochemical Society, 1989. **136**(4): p. 996-1002.
9. Kiratzis, N. and M. Stoukides, *The Synthesis of Hydrogen Cyanide in a Solid Electrolyte Fuel Cell.* Journal of The Electrochemical Society, 1987. **134**(8): p. 1925-1929.
10. Carrillo, A.S., T. Tagawa, and S. Goto, *Application of mist pyrolysis method to preparation of Ni/ZrO2 anode catalyst for SOFC type reactor.* Materials Research Bulletin, 2001. **36**(5–6): p. 1017-1027.
11. Keller, G.E. and M.M. Bhasin, *Synthesis of ethylene via oxidative coupling of methane: I. Determination of active catalysts.* Journal of Catalysis, 1982. **73**(1): p. 9-19.

12. Wang, J., et al., *Comparative study on oxidation of methane to ethane and ethylene over Na2WO4–Mn/SiO2 catalysts prepared by different methods.* Journal of Molecular Catalysis A: Chemical, 2006. **245**(1–2): p. 272-277.
13. Fakhroueian, Z., F. Farzaneh, and N. Afrookhteh, *Oxidative coupling of methane catalyzed by Li, Na and Mg doped BaSrTiO3.* Fuel, 2008. **87**(12): p. 2512-2516.
14. Pujare, N.U. and A.F. Sammells, *Methane Activation to C 2 Hydrocarbon Species in Solid Oxide Fuel Cell.* Journal of The Electrochemical Society, 1988. **135**(10): p. 2544-2545.
15. Au, C.T., et al., *The Oxidative Coupling of Methane over BaCO3/LaOBr—Catalysts of High Ethylene Yield.* Journal of Catalysis, 1996. **163**(2): p. 399-408.
16. Morikawa, K.O.a.A., *Japanese Patent*. 1986: Japan.
17. Steele, B.C.H., et al., *Oxidation of methane in solid state electrochemical reactors.* Solid State Ionics, 1988. **28–30, Part 2**(0): p. 1547-1552.
18. Otsuka, K., K. Suga, and I. Yamanaka, *Oxidative coupling of methane applying a solid oxide fuel cell system.* Catalysis Today, 1990. **6**(4): p. 587-592.
19. De, M.P.E.V., et al., *A method for the production of light hydrocarbons from gas with high methane content, a solid oxide fuel cell used for the production of light hydrocarbons from gas with high methane content, and a catalyst for the production of light hydrocarbons from gas with high methane content*. 2010, Google Patents.
20. Saracco, G. and V. Specchia, *Catalytic Inorganic-Membrane Reactors: Present Experience and Future Opportunities.* Catalysis Reviews, 1994. **36**(2): p. 305-384.
21. White, J.H., et al., *The electrochemical oxidative dimerization of methane.* Solid State Ionics, 1992. **53–56, Part 1**(0): p. 149-161.
22. Kong, J., et al., *Synthesis and electrochemical properties of LSM and LSF perovskites as anode materials for high temperature steam electrolysis.* Journal of Power Sources, 2009. **186**(2): p. 485-489.
23. Chen, K., N. Ai, and S.P. Jiang, *Performance and stability of (La,Sr)MnO3–Y2O3–ZrO2 composite oxygen electrodes under solid oxide electrolysis cell operation conditions.* International Journal of Hydrogen Energy, 2012. **37**(14): p. 10517-10525.
24. Barison, S., et al., *Novel Au/La1−xSrxMnO3 and Au/La1−xSrxCrO3 composites: Catalytic activity for propane partial oxidation and reforming.* Solid State Ionics, 2007. **177**(39–40): p. 3473-3484.

25. Corre, G., et al., *Activation and Ripening of Impregnated Manganese Containing Perovskite SOFC Electrodes under Redox Cycling.* Chemistry of Materials, 2009. **21**(6): p. 1077-1084.
26. Kim, G., et al., *Investigation of the Structural and Catalytic Requirements for High-Performance SOFC Anodes Formed by Infiltration of LSCM.* Electrochemical and Solid-State Letters, 2009. **12**(3): p. B48-B52.
27. Lee, S., et al., *Solid oxide fuel cell cathodes prepared by infiltration of LaNi0.6Fe0.4O3 and La0.91Sr0.09Ni0.6Fe0.4O3 in porous yttria-stabilized zirconia.* Journal of Power Sources, 2009. **193**(2): p. 747-753.
28. Yang, C., et al., *Characterization of infiltrated (La0.75Sr0.25)0.95MnO3 as oxygen electrode for solid oxide electrolysis cells.* International Journal of Hydrogen Energy, 2010. **35**(11): p. 5187-5193.
29. He, H., et al., *Low-Temperature Fabrication of Oxide Composites for Solid-Oxide Fuel Cells.* Journal of the American Ceramic Society, 2004. **87**(3): p. 331-336.
30. Tao, S. and J.T.S. Irvine, *Synthesis and Characterization of (La0.75Sr0.25) Cr0.5Mn0.5 O 3 – δ , a Redox-Stable, Efficient Perovskite Anode for SOFCs.* Journal of The Electrochemical Society, 2004. **151**(2): p. A252-A259.
31. Baker, R.T., et al., *Catalytic Behavior of LiFeO2 Anode for Solid Oxide Fuel Cells*, in *Studies in Surface Science and Catalysis*, F.S. L. Guczi and T. P, Editors. 1993, Elsevier. p. 2127-2130.
32. Huang, B., et al., *Study of LiFeO2 coated NiO as cathodes for MCFC by electrochemical impedance spectroscopy.* Journal of Power Sources, 2004. **137**(2): p. 163-174.
33. Amin, N.A.S. and S.E. Pheng, *Influence of process variables and optimization of ethylene yield in oxidative coupling of methane over Li/MgO catalyst.* Chemical Engineering Journal, 2006. **116**(3): p. 187-195.
34. van Kasteren, J.M.N., J.W.M.H. Geerts, and K. van der Wiele, *The role of heterogeneous reactions during the oxidative coupling of methane over Li/MgO catalysts.* Catalysis Today, 1990. **6**(4): p. 497-502.
35. Morales, E. and J.H. Lunsford, *Oxidative dehydrogenation of ethane over a lithium-promoted magnesium oxide catalyst.* Journal of Catalysis, 1989. **118**(1): p. 255-265.
36. Simon, U., et al., *Li/MgO with spin sensors as catalyst for the oxidative coupling of methane.* Catalysis Communications, 2012. **18**(0): p. 132-136.

37. Jianjun, Z., et al., *Role of Li Ion in Li-Mn-MgO catalyst for oxidative coupling of methane.* Catalysis Today, 1992. **13**(4): p. 555-558.
38. Choudhary, V.R., et al., *Oxidative conversion of methane to C2 hydrocarbons over Li, Mn, Cd and Zn promoted MgO catalysts : II: Performance of fresh and reoxidised catalysts in the absence of free oxygen.* Applied Catalysis, 1991. **69**(1): p. 187-200.
39. M. Aigler, J. and J. H. Lunsford, *Oxidative dimerization of methane over MgO and Li+/MgO monoliths.* Applied Catalysis, 1991. **70**(1): p. 29-42.
40. Miyazaki, T., et al., *Structure and catalysis of layered rock-salt type oxides for methane oxidation.* Applied Surface Science, 1997. **121–122**(0): p. 492-495.
41. Ito, T. and J.H. Lunsford, *Synthesis of ethylene and ethane by partial oxidation of methane over lithium-doped magnesium oxide.* Nature, 1985. **314**(6013): p. 721-722.
42. Choudhary, V. and B. Uphade, *Oxidative Conversion of Methane/Natural Gas into Higher Hydrocarbons.* Catalysis Surveys from Asia, 2004. **8**(1): p. 15-25.
43. Lunsford, J.H., *Catalytic conversion of methane to more useful chemicals and fuels: a challenge for the 21st century.* Catalysis Today, 2000. **63**(2–4): p. 165-174.
44. Zohour, B., D. Noon, and S. Senkan, *New Insights into the Oxidative Coupling of Methane from Spatially Resolved Concentration and Temperature Profiles.* ChemCatChem, 2013. **5**(10): p. 2809-2812.
45. Alcaide, F., P.-L. Cabot, and E. Brillas, *Fuel cells for chemicals and energy cogeneration.* Journal of Power Sources, 2006. **153**(1): p. 47-60.
46. James Larminie, A.D., *Fuel Cell Systems Explained*. 2 ed. 2003, J. Wiley.
47. Singhal, S.C., *Advances in solid oxide fuel cell technology.* Solid State Ionics, 2000. **135**(1–4): p. 305-313.
48. Steele, B.C.H., *Appraisal of Ce1−yGdyO2−y/2 electrolytes for IT-SOFC operation at 500°C.* Solid State Ionics, 2000. **129**(1–4): p. 95-110.
49. Takanashi, N.Q.M.a.T., *Science and technology of ceramic fuel*. Vol. 76. 1995, Elsevier Science
50. Michaels, J.N. and C.G. Vayenas, *Kinetics of vapor-phase electrochemical oxidative dehydrogenation of ethylbenzene.* Journal of Catalysis, 1984. **85**(2): p. 477-487.
51. Godini, H.R., et al., *Design and demonstration of an experimental membrane reactor set-up for oxidative coupling of methane.* Chemical Engineering Research and Design, 2013. **91**(12): p. 2671-2681.

52. Tan, X., et al., *Catalytic perovskite hollow fibre membrane reactors for methane oxidative coupling.* Journal of Membrane Science, 2007. **302**(1–2): p. 109-114.
53. Lu, Y., et al., *Oxidative coupling of methane in a modified γ-alumina membrane reactor.* Chemical Engineering Science, 2000. **55**(21): p. 4901-4912.
54. Reed, J.S., *Introduction to the principles of ceramic processing:*. 1989, Newyork: Wiley.
55. Williams, J.J., *The Influence of Constitutive Relationships on Stress-Redistribution Times in Creeping Structures.* Journal of Applied Mechanics, 1976. **43**: p. 173-175.
56. Hotza, D. and P. Greil, *Review: aqueous tape casting of ceramic powders.* Materials Science and Engineering: A, 1995. **202**(1–2): p. 206-217.
57. Naiqing, Z., et al., *Study on Properties of LSGM Electrolyte Made by Tape Casting Method and Applications in SOFC.* Journal of Rare Earths, 2006. **24**(1, Supplement 1): p. 90-92.
58. J.R.M., *Impedance Spectroscopy: Theory, Experiment, and Applications*. 2005: Wiley Interscience Publications
59. R. Kirk, D.O., *Encyclopedia of Chemical Technology*. 1981, New York: John Wiley & Sons
60. Boch, P. and T. Chartier, *Tape Casting and Properties of Mullite and Zirconia–Mullite Ceramics.* Journal of the American Ceramic Society, 1991. **74**(10): p. 2448-2452.
61. Plucknett, K.P., C.H. Cáceres, and D.S. Willinson, *Tape Casting of Fine Alumina/Zirconia Powders for Composite Fabrication.* Journal of the American Ceramic Society, 1994. **77**(8): p. 2137-2144.
62. Wachtman, J.B., *Ceramic innovations in the 20th century*. 1999: . The American Ceramic Society.
63. Burrel, H., *Solubillity Parameters*. 1995: Interchem. Rev.
64. Tok, A.I.Y., F.Y.C. Boey, and M.K.A. Khor, *Tape casting of high dielectric ceramic substrates for microelectronics packaging.* Journal of Materials Engineering and Performance, 1999. **8**(4): p. 469-472.
65. Jones, F.G.E. and J.T.S. Irvine, *Preparation of thin films using the tape-casting process for use in the solid oxide fuel cell.* Ionics, 2002. **8**(5-6): p. 339-343.

66. Lide, D.R., *Handbook of Chemistry and Physics*. 76th edition ed. 1995, Florida: CRC Press.
67. Lemonie, J.M. and J.L. Mathis, *Fabrication techniques for multilayer ceramic modules*. 1977, Google Patents.
68. Horn, R.G., *Particle interactions in suspensions*. 1995 Springer Netherlands.
69. Mistler, R.E.a.E.R.T., *Tape Casting:* . Theory and Practice. 2000: Wiley.
70. Vohs, J.M. and R.J. Gorte, *High-Performance SOFC Cathodes Prepared by Infiltration.* Advanced Materials, 2009. **21**(9): p. 943-956.
71. Mistler, R.E.a.E.R.T., *Tape Casting: Theory and Practice*. 2000: Wiley.
72. Cowin, P.I., et al., *Recent Progress in the Development of Anode Materials for Solid Oxide Fuel Cells.* Advanced Energy Materials, 2011. **1**(3): p. 314-332.
73. Jiang, S.P., *Nanoscale and nano-structured electrodes of solid oxide fuel cells by infiltration: Advances and challenges.* International Journal of Hydrogen Energy, 2012. **37**(1): p. 449-470.
74. Liu, Z., et al., *Fabrication and modification of solid oxide fuel cell anodes via wet impregnation/infiltration technique.* Journal of Power Sources, 2013. **237**(0): p. 243-259.
75. Shah, M. and S.A. Barnett, *Solid oxide fuel cell cathodes by infiltration of La0.6Sr0.4Co0.2Fe0.8O3 – δ into Gd-Doped Ceria.* Solid State Ionics, 2008. **179**(35–36): p. 2059-2064.
76. Liu, L., et al., *A novel doped CeO2–LaFeO3 composite oxide as both anode and cathode for solid oxide fuel cells.* International Journal of Hydrogen Energy, 2012. **37**(17): p. 12574-12579.
77. Smith, J.R., et al., *Evaluation of the relationship between cathode microstructure and electrochemical behavior for SOFCs.* Solid State Ionics, 2009. **180**(1): p. 90-98.
78. Gorte, R.J. and J.M. Vohs, *Nanostructured anodes for solid oxide fuel cells.* Current Opinion in Colloid & Interface Science, 2009. **14**(4): p. 236-244.
79. Hukins, D., *X-Ray Diffraction by Disordered and Ordered Systems*. 1st Edition ed. 1981.
80. Hull, A.W., *A NEW METHOD OF CHEMICAL ANALYSIS.* Journal of the American Chemical Society, 1919. **41**(8): p. 1168-1175.
81. Bragg, W.H., *X rays and Crystals*. 1912, Nature. p. 219.
82. Scanning Electron Microscope.
83. Rahaman, M.N., *Ceramic Processing and Sintering*. 2003, Florida: CRC Press. 875.

84. Rahaman, M.N., *Ceramic Processing and Sintering*. 2003: Florida: CRC Press.
85. Palermo, A., et al., *Critical influence of the amorphous silica-to-cristobalite phase transition on the performance of Mn/Na2WO4/SiO2 catalysts for the oxidative coupling of methane.* Journal of Catalysis, 1998. **177**(2): p. 259-266.
86. Pak, S. and J.H. Lunsford, *Thermal effects during the oxidative coupling of methane over Mn/Na2WO4/SiO2 and Mn/Na2WO4/MgO catalysts.* Applied Catalysis A: General, 1998. **168**(1): p. 131-137.
87. Chua, Y.T., A.R. Mohamed, and S. Bhatia, *Oxidative coupling of methane for the production of ethylene over sodium-tungsten-manganese-supported-silica catalyst (Na-W-Mn/SiO2).* Applied Catalysis A: General, 2008. **343**(1–2): p. 142-148.
88. Yamashita, H., Y. Machida, and A. Tomita, *Oxidative coupling of methane with peroxide ions over barium-lanthanum-oxygen mixed oxide.* Applied Catalysis A: General, 1991. **79**(2): p. 203-214.
89. Malekzadeh, A., et al., *Correlation of electrical properties and performance of OCM MOx/Na2WO4/SiO2 catalysts.* Catalysis Communications, 2001. **2**(8): p. 241-247.
90. Ji, S.-f., et al., *The relationship between the structure and the performance of Na-W-Mn/SiO2 catalysts for the oxidative coupling of methane.* Applied Catalysis A: General, 2002. **225**(1–2): p. 271-284.
91. Papa, F., et al., *Catalytic activity of neodymium substituted zinc ferrites for oxidative conversion of methane.* Journal of Molecular Catalysis A: Chemical, 2009. **299**(1–2): p. 93-97.
92. Wu, J., et al., *La-promoted Na2WO4/Mn/SiO2 catalysts for the oxidative conversion of methane simultaneously to ethylene and carbon monoxide.* Applied Catalysis A: General, 2007. **323**(0): p. 126-134.
93. Guo, X.-M., et al., *Oxidative Coupling of Methane in a Solid Oxide Membrane Reactor.* Industrial & Engineering Chemistry Research, 1997. **36**(9): p. 3576-3582.
94. Shahri, S.M.K. and A.N. Pour, *Ce-promoted Mn/Na2WO4/SiO2 catalyst for oxidative coupling of methane at atmospheric pressure.* Journal of Natural Gas Chemistry, 2010. **19**(1): p. 47-53.
95. Wang, W. and Y.S. Lin, *Analysis of oxidative coupling of methane in dense oxide membrane reactors.* Journal of Membrane Science, 1995. **103**(3): p. 219-233.

96. Liu, S., et al., *METHANE COUPLING USING CATALYTIC MEMBRANE REACTORS.* Catalysis Reviews, 2001. **43**(1-2): p. 147-198.
97. Lafarga, D., J. Santamaria, and M. Menéndez, *Methane oxidative coupling using porous ceramic membrane reactors—I. reactor development.* Chemical Engineering Science, 1994. **49**(12): p. 2005-2013.
98. Coronas, J., M. Menéndez, and J. Santamaria, *Methane oxidative coupling using porous ceramic membrane reactors—II. Reaction studies.* Chemical Engineering Science, 1994. **49**(12): p. 2015-2025.
99. Coronas, J., M. Menendez, and J. Santamaria, *Development of ceramic membrane reactors with a non-uniform permeation pattern. Application to methane oxidative coupling.* Chemical Engineering Science, 1994. **49**(24, Part A): p. 4749-4757.
100. Nozaki, T., et al., *Selective oxidative coupling of methane with membrane reactor.* Chemical Engineering Science, 1992. **47**(9–11): p. 2945-2950.
101. Nozaki, T. and K. Fujimoto, *Oxide ion transport for selective oxidative coupling of methane with new membrane reactor.* AIChE Journal, 1994. **40**(5): p. 870-877.
102. Bytyn, W. and M. Baerns, *Supported PbO catalysts for the oxidative coupling of methane — The effect of surface acidity of the support on C2+ selectivity.* Applied Catalysis, 1986. **28**(0): p. 199-207.
103. Santos, A., et al., *Reactor Engineering Studies of Methane Oxidative Coupling on a Li/Mgo Catalyst*, in *Studies in Surface Science and Catalysis*, H.E. Curry-Hyde and R.F. Howe, Editors. 1994, Elsevier. p. 171-176.
104. Zeng, Y. and Y.S. Lin, *Oxygen Permeation and Oxidative Coupling of Methane in Yttria Doped Bismuth Oxide Membrane Reactor.* Journal of Catalysis, 2000. **193**(1): p. 58-64.
105. Xui-Mei, G., K. Hidajat, and C.-B. Ching, *Simulation of a solid oxide fuel cell for oxidative coupling of methane.* Catalysis Today, 1999. **50**(1): p. 109-116.
106. Tagawa, T., et al., *Fuel cell type reactor for Chemicals-energy co-generation.* Chemical Engineering Science, 1999. **54**(10): p. 1553-1557.
107. Farr, R.D. and C.G. Vayenas, *Ammonia High Temperature Solid Electrolyte Fuel Cell.* Journal of The Electrochemical Society, 1980. **127**(7): p. 1478-1483.
108. Kiatkittipong, W., et al., *Oxygen transport through LSM/YSZ/LaAlO system for use of fuel cell type reactor.* Chemical Engineering Journal, 2005. **106**(1): p. 35-42.

109. Lapeña-Rey, N. and P.H. Middleton, *The selective oxidation of methane to ethane and ethylene in a solid oxide electrolyte reactor.* Applied Catalysis A: General, 2003. **240**(1–2): p. 207-222.

110. Wiglusz, R.J., et al., *Conductivity and electric properties of La1–xSrxMnO3–δ nanopowders.* Journal of Rare Earths, 2009. **27**(4): p. 651-654.

111. Spinicci, R., et al., *Oxidative coupling of methane on LaAlO3 perovskites partially substituted with alkali or alkali-earth ions.* Journal of Molecular Catalysis A: Chemical, 2001. **176**(1–2): p. 253-265.

112. Jiang, S., *Development of lanthanum strontium manganite perovskite cathode materials of solid oxide fuel cells: a review.* Journal of Materials Science, 2008. **43**(21): p. 6799-6833.

113. Luengnaruemitchai, A., et al., *A comparative study of and catalysts for the catalytic oxidation of CO in hydrogen rich stream.* International Journal of Hydrogen Energy, 2005. **30**(9): p. 981-987.

114. Haruta, M., *Size- and support-dependency in the catalysis of gold.* Catalysis Today, 1997. **36**(1): p. 153-166.

115. Haruta, M., et al., *Gold catalysts prepared by coprecipitation for low-temperature oxidation of hydrogen and of carbon monoxide.* Journal of Catalysis, 1989. **115**(2): p. 301-309.

116. Waters, R.D., J.J. Weimer, and J.E. Smith, *An investigation of the activity of coprecipitated gold catalysts for methane oxidation.* Catalysis Letters, 1994. **30**(1-4): p. 181-188.

117. Yang, H.-C., F.-W. Chang, and L.S. Roselin, *Hydrogen production by partial oxidation of methanol over Au/CuO/ZnO catalysts.* Journal of Molecular Catalysis A: Chemical, 2007. **276**(1–2): p. 184-190.

118. Shimazu, M., et al., *Stability of Sc2O3 and CeO2 co-doped ZrO2 electrolyte during the operation of solid oxide fuel cells: Part III. Detailed mechanism of the decomposition.* Solid State Ionics, 2012. **224**(0): p. 6-14.

119. Hornés, A., et al., *Catalytic properties of monometallic copper and bimetallic copper-nickel systems combined with ceria and Ce-X (X = Gd, Tb) mixed oxides applicable as SOFC anodes for direct oxidation of methane.* Journal of Power Sources, 2007. **169**(1): p. 9-16.

120. Lay, E., et al., *Ce-substituted LSCM as new anode material for SOFC operating in dry methane.* Solid State Ionics, 2008. **179**(27–32): p. 1562-1566.

121. Cai, G., et al., *Anode performance of Mn-doped ceria–ScSZ for solid oxide fuel cell.* Journal of Solid State Electrochemistry, 2011. **15**(1): p. 147-152.

122. Lee, S., et al., *Oxygen-permeating property of LaSrBFeO3 (B=Co, Ga) perovskite membrane surface-modified by LaSrCoO3.* Solid State Ionics, 2003. **158**(3–4): p. 287-296.

123. Letilly, M., A. Le Gal La Salle, and O. Joubert, *Electrochemical Optimization of LSCF/BIT07 as an Alternative Cathode/electrolyte Couple for SOFC.* ECS Transactions, 2009. **25**(2): p. 2837-2844.

124. Yan, A., et al., *Investigation of a Ba0.5Sr0.5Co0.8Fe0.2O3–δ based cathode IT-SOFC: I. The effect of CO2 on the cell performance.* Applied Catalysis B: Environmental, 2006. **66**(1–2): p. 64-71.

125. Tarancón, A., et al., *Effect of phase transition on high-temperature electrical properties of GdBaCo2O5 + x layered perovskite.* Solid State Ionics, 2008. **179**(17–18): p. 611-618.

126. Chang, A., S.J. Skinner, and J.A. Kilner, *Electrical properties of GdBaCo2O5+x for ITSOFC applications.* Solid State Ionics, 2006. **177**(19–25): p. 2009-2011.

127. Lü, S., et al., *Performance of double-perovskite YBa0.5Sr0.5Co1.4Cu0.6O5+δ as cathode material for intermediate-temperature solid oxide fuel cells.* Ceramics International, (0).

128. Shao, Z., et al., *Synthesis and oxygen permeation study of novel perovskite-type BaBixCo0.2Fe0.8–xO3–δ ceramic membranes.* Journal of Membrane Science, 2000. **164**(1–2): p. 167-176.

129. Gaudon, M., et al., *Evaluation of a sol–gel process for the synthesis of La1–xSrxMnO3+δ cathodic multilayers for solid oxide fuel cells.* Journal of Power Sources, 2004. **133**(2): p. 214-222.

130. Gaudon, M., et al., *Preparation and characterization of La1–xSrxMnO3+δ ($0 \leqslant x \leqslant 0.6$) powder by sol–gel processing.* Solid State Sciences, 2002. **4**(1): p. 125-133.

131. Tang, L., et al., *The promoting effect of ceria on Li/MgO catalysts for the oxidative coupling of methane.* Catalysis Today, 2011. **178**(1): p. 172-180.

132. Ito, T., et al., *Oxidative dimerization of methane over a lithium-promoted magnesium oxide catalyst.* Journal of the American Chemical Society, 1985. **107**(18): p. 5062-5068.

133. Metcalfe, I.S., et al., *Hydrocarbon activation in solid state electrochemical cells.* Solid State Ionics, 1992. **57**(3–4): p. 259-264.

134. Palanna, O.G., *Engineering Chemistry*. 2009: Tata McGraw-Hill Education Pvt. Ltd.

135. Ishihara, T., H. Matsuda, and Y. Takita, *Effects of rare earth cations doped for La site on the oxide ionic conductivity of LaGaO3-based perovskite type oxide.* Solid State Ionics, 1995. **79**(0): p. 147-151.

136. Ishihara, T., et al., *Recent progress in LaGaO3 based solid electrolyte for intermediate temperature SOFCs.* Solid State Ionics, 2006. **177**(19–25): p. 1949-1953.

APPENDIX

APPENDIX A

CALCULATION FOR METHAANE CONVERSION AND PRODUCTS SELECTIVITY

The terms of the reaction performance were defined as follows:

$$C_{H_4}\ \text{conversion} = \frac{F_{CH_4}^{in} - F_{CH_4}^{out}}{F_{CH_4}^{in}} \times 100 \quad \text{(A.1)}$$

Where $F_{CH_4}^{in}$ and $F_{CH_4}^{out}$ are the molarof CH_4 inlet and outlet, respectively.

$$\text{Selectivity of C2}\ \left(SC_{2,}\%\right) = 100x\frac{2(F_{C_2H_4}+F_{C_2H_6})}{F_{CH_4}^{in} - F_{CH_4}^{out}} \quad \text{(A.2)}$$

$$\text{Yield of C2}\ \left(YC_{2,}\%\right) = \frac{(SC_{2,}\%)(X_{CH_4}\%)}{100} \quad \text{(A.3)}$$

$$\text{Selectivity of } CO_2\ \left(S_{CO_2}\ \%\right) = 100x\frac{F_{CO_2}}{F_{CH_4}^{in} - F_{CH_4}^{out}} \quad \text{(A.4)}$$

$$\text{Selectivity of CO}\ \left(S_{CO}\ \%\right) = 100x\frac{F_{CO}}{F_{CH_4}^{in} - F_{CH_4}^{out}} \quad \text{(A.5)}$$

$$\text{Selectivity of } H_2\ \left(S_{H_2}\ \%\right) = 100x\frac{F_{H_2}}{2x(F_{CH_4}^{in} - F_{CH_4}^{out})} \quad \text{(A.6)}$$

APPENDIX B

CONDITION OF GAS CHROMATROGRAPHY

The conditions of Gas Chromatography (GC) analysis for this study are provide as following,

Gas analysis of reactants and products was performed by on-line gas chromatography (Shimadzu 14A with thermal conductivity detector, equipped with a Porapak column for separation of C_2H_4, C_3H_8 and CO_2 and a Molecular sieve for the O_2 detection). He was used as the carrier gas as presented in Table B.1

Table B.1 GC analysis condition for methane oxidation

Gas Chromatography	Shimadzu A14A
Detector	TCD (Thermal conductivity detector)
Column	Porapak (C_2H_4, C_3H_8 and CO_2) Molecular sieve (O_2)
Carrier gas	He
TCD temperature (°C)	150
Injector temperature (°C)	120
Detector temperature (°C)	138
Column temperature (°C)	80
Current (mA)	124

APPENDIX C

LIST OF PUBLICATIONS

C1. International publications

1. Wiyaratn, W., Appamana, W., Assabumrungrat, S. Development of Au/$La_{1-x}Sr_xMnO_3$ nanocomposites for further application in a solid oxide fuel cell type reactor (2011) Journal of Industrial and Engineering Chemistry, 17 (3), pp. 474-478. (Impact Factor: 2.206)
2. Wiyaratn, W., Appamana, W., Charojrochkul, S., Kaewkuekool, S., Assabumrungrat, S. Au/$La_{1-x}Sr_xMnO_3$ nanocomposite for chemical-energy cogeneration in solid oxide fuel cell reactor (2012) Journal of Industrial and Engineering Chemistry, 18 (5), pp. 1819-1823. (Impact Factor: 2.206)

C2. International conferences

1. W. Wiyaratn, W. Appamana and S. Assabumrungrat. Chemicals Production through Oxidative Coupling of Methane over Au/$La_{1-x}Sr_xMnO_3$ (x=0.4) Nanocomposites in Fixed Bed Reactor, 2009. World renewable energy congress 2009 (Asia), The 3rd International conference on xSustianable energy and environment (SEE 2009),18-23 May 2009, Bangkok Thailand (Oral Presentation).
2. W. Wiyaratn, W. Appamana and S. Assabumrungrat. Development of Novel Au/LSM Nanocomposite Material For Application in Solid Oxide Fuel Cell Typed Reactor, 2010. The 3rd technology and innovation for sustainable

devilment international conference, 4-6 March 2010, Nong khai, Thailand (Oral Presentation).

3. W. Wiyaratn, W. Appamana, S. Charojrochkul, S. Kaewkuekool, S. Assabumrungrat. Investigation the Effect of Au Nanocomposite on Au/$La_{1-x}Sr_xMnO_3$ (x=0.4) Perovskite Catalysts for Application in SOFC Reactor, 2011. TIChE International Conference 2011, 10-11 November 2011, Hatyai, Songkhla, Thailand (Poster Presentation).
4. W . Appamana , W. Wiyaratn, S. Charojrochkul and S. Assabumrungrat. Synthesis of Na_2WO_4-Mn supported YSZ as a potential anode catalyst for oxidative coupling of methane in SOFC, 2012. 62nd Canadian Chemical Engineering Conference, 14-17 October 2012, Vancouver, British Columbia, Canada (Oral Presentation).

VITA

Miss Weerinda Appamana was born on November 10, 1984 in Phayao, Thailand. She graduated high school from Dokkhamtai Witthayakhom School, Phayao in 2004. She received Bachelor's Degree in Chemical engineering from Rajamangala University of Technology Thanyaburi in 2008. She consequently continued studying Doctoral degree of Chemical Engineering, Chulalongkorn University since May 2008 and received Royal Golden Jubilee PhD program Scholarship from Thailand Research Fund (TRF) and Chulalongkorn University. She had collaborated with Professor Johh T.S. Irvine and finished parts of her research experiment at Energy materials research laboratory, School of Chemistry,University of St Andrews, St Andrews, Scotland, UK from June 1, 2012- September 25, 2013.